

Diss. ETH No. 18172

An Ultra-High-Speed Electrical Drive System

A dissertation submitted to the
ETH ZURICH

for the degree of
DOCTOR OF SCIENCES

presented by
CHRISTOF ZWYSSIG
Dipl. El. Ing. ETH Zurich
born 24. July 1978
citizen of Seelisberg, Switzerland

accepted on the recommendation of
Prof. Dr. Johann W. Kolar, examiner
Prof. Dr. Rik W. De Doncker, co-examiner

2008

Acknowledgements

The following Thesis would not have been possible without the support of various people. My first thank goes to my supervisor Prof. Dr. Johann W. Kolar for his motivating optimism and his great support for the still continuing ultra-high-speed drives project.

I am very grateful to Prof. Dr. Rik W. De Doncker for co-referring this Thesis, and to Prof. Dr. Jorma Luomi for spending a part of his sabbatical helping me optimizing ultra-high-speed machines. Furthermore I am also indebted to Prof. Dr. Konrad Reichert for helping me in the initial phase of the project, and Prof. Dr. Jörg Hugel for the fruitful discussions on balancing.

I would like to thank the entire PES staff including PhD students, secretaries and electronics workshop for providing a fantastic research and social environment. I always have and still am enjoying the inspiring diversity of know-how and personalities.

A huge thank you goes to all the Semester- and Master-Theses students who play a big part in the success of this Thesis.

I had great support from and discussions with various people in industry. A special thank goes to the team at ATE Antriebstechnik und Entwicklungs GmbH. Furthermore I would like to thank Myonic, Precision Magnetics and High-Speed Turbomaschinen GmbH. I also wish to thank the machine shops at ETH for tolerating flexible tolerances.

Furthermore, I thank Martin Bartholet for taking on the adventure of founding a company out of this research project with me.

Last but not least, I would like to thank my family and friends, everyone that cares about me and shares my interests beside work, for believing in me.

Abstract

The development of ultra-high-speed and ultra-compact electrical drive systems is needed for new emerging applications, such as generators and starters for micro gas turbines, turbocompressor systems, drills for surgery tools, and machining spindles. For the expected rotational speeds in the area of 500 000 to 1 million revolutions per minute (rpm), no known research effort has occurred, and therefore new solutions for the electrical machine, the power electronics converter and the (sensorless) control have to be found.

This Thesis deals with the different parts of, as well as the integration into, an ultra-high-speed drive system. The goal is the best combination of the individual parts in order to realize an ultra-high-speed electrical drive system with highest efficiency and power density. A permanent-magnet machine suitable for highest-speed operation is identified and an integrated mechanical and electromagnetic design and optimization method is developed. Existing and new inverter topologies and control methods are evaluated, and a pulse amplitude modulation (PAM) inverter together with a stator flux-based sensorless control is adapted for highest-speed operation. Furthermore, for integrating the electrical drive system into an application, possible high-speed bearing technologies are compared and a thermal and rotordynamic design is presented on the example of a miniature turbocompressor system.

The results are verified with two hardware prototypes of machine and power and control electronics, a world record speed test bench rotating at 1 million rpm and a 500 000 rpm drive system which is integrated into a miniature turbocompressor.

Kurzfassung

Die Entwicklung ultrahochdrehender elektrischer Antriebssysteme wird benötigt für neuartige, aufkommende Anwendungen, wie Generatoren und Starter für Mikrogasturbinen, Turbokompressoren, Bohrer für medizinische Handstücke, und Materialbearbeitungsspindeln. Für die voraussichtlichen Drehzahlen im Bereich von 500 000 und 1 Million Umdrehungen pro Minute (U/min) haben bisher keine Forschungsanstrengungen stattgefunden, und daher bedarf es neuer Lösungen für die elektrische Maschine, den Wechselrichter und die (sensorlose) Regelung.

Diese Dissertation befasst sich mit den einzelnen Komponenten, sowie der Integration in ein ultrahochdrehendes Antriebssystem. Das Ziel ist die beste Kombination der individuellen Komponenten um ein ultrahochdrehendes Antriebssystem mit höchstem Wirkungsgrad und Leistungsdichte zu realisieren. Eine permanentmagnetisch erregte Maschine, geeignet für den Betrieb mit höchsten Drehzahlen, wird eruiert und eine ganzheitliche, mechanische und elektromagnetische Auslegung und Optimierung wird entwickelt. Bestehende und neue Wechselrichtertopologien werden evaluiert und ein 'pulse amplitude modulation' (PAM) Wechselrichter zusammen mit einer sensorlosen Regelung basierend auf dem Statorfluss wird adaptiert für den Betrieb mit höchsten Drehzahlen. Für die Integration in eine Anwendung werden zudem mögliche Lagerarten verglichen und es wird, anhand des Beispiels eines Mikroturbokompressors, eine thermische und rotordynamische Auslegung präsentiert.

Die Resultate werden anhand zweier Prototypen von Maschine und Leistungs- und Steuerelektronik verifiziert, einem Prüfstand mit der Weltrekorddrehzahl von 1 Million U/min und einem Antriebssystem mit einer Drehzahl von 500 000 U/min welches in einen Miniaturturbokompressor integriert wird.

Notation

Symbols

A	area
B, \mathbf{B}	magnetic flux density, vector
$B_{rem}, \mathbf{B}_{rem}$	remanence flux density, vector
C	Esson's utilization factor or capacitance
C_m	Steinmetz coefficient
c_f	friction coefficient
C_b	bearing stiffness matrix
c_b	bearing stiffness
D_r	rotor diameter
D	diameter
E	Young's modulus
F	copper loss coefficient
f	frequency
G	copper loss coefficient or gyroscopic matrix
H, \mathbf{H}	magnetic field strength, vector
I	area moment of inertia
$i, \underline{i}, \mathbf{i}$	current, space vector, fixed to rotor axis
J	current density or inertia
J_1	spatial fundamental wave of current density
K_B	flux density coefficient
k_{Cu}	winding fill factor
$k_{Cu,s}$	strand packing factor

$k_{Cu,t}$	turn fill factor
k_w	fundamental wave winding factor
L	active length or inductance
M	mass matrix
M_p, \mathbf{M}_p	permanent magnetization, vector
m	mass
n	rotational speed
P	active power or power losses
P_d	total power losses
q	distrubuted load
R	resistance
R_1	radius of the permanent magnet
R_2	outer radius of the rotor sleeve
R_3	inner radius of the stator winding
R_4	inner radius of the stator core
R_5	outer radius of the stator core
Re	Reynolds number
S	apparent power or stiffness matrix
s	zero crossing signals
T	transistor switching signals or temperature
T_e	electromagnetic torque
T_b	breaking torque
T_m	mechanical torque
Ta	Taylor number
t	time
u	displacement
$u, \underline{u}, \mathbf{u}$	voltage, space vector, fixed to rotor axis
\mathbf{u}_r	radial unit vector
\mathbf{u}_θ	azimuthal unit vector
V	Voltage or Volume
α	Steinmetz coefficient
α_{th}	coefficient of thermal expansion
β	Steinmetz coefficient
γ	machine scaling factor

ΔT	temperature difference
Δu	difference in displacement
Δu_0	interference fit
δ	air-gap or current displacement angle
ϵ	rotor magnet angle
λ	length to diameter ratio
μ_0	magnetic constant
μ_r	relative recoil permeability
ν	Poisson's ratio or kinematic viscosity
ρ	density
σ	stress or conductivity
σ_v	von Mises stress
σ_{UTS}	tensile strength
ϕ	magnetic scalar potential
$\psi, \underline{\psi}$	flux linkage or deflection, space vector
ω	angular frequency

Subscripts

1	magnetic region 1 (permanent magnet)
2	magnetic region 2 (air)
3	magnetic region 3 (stator core)
a, b, c	phase a, b, c component
Cu	copper
d	direct-axis component
Fe	iron
f	friction
p	proximity effect component
ph	phase component
pm	permanent-magnet
q	quadrature-axis component
r	radial component
res	resonance
s	skin effect component or stator component

sl	rotor sleeve
t	terminal
θ	tangential/azimuthal component

Abbreviations

BLDC	brushless dc machine
CSI	current source inverter
CTE	coefficient of thermal Expansion
DSP	digital signal processor
EMF	electromotive force
FE	finite element
HVAC	heating ventilation and air conditioning
IM	induction machine
MEMS	micro-electrical-mechanical systems
MOSFET	metal-oxide-semiconductor field-effect transistor
Ni-Fe	nickel-iron
PAM	pulse amplitude modulation
PCB	printed circuit board
PMSM	permanent-magnet synchronous machine
PWM	pulse width modulation
Si-Fe	silicon-iron
SMC	soft magnetic composite
SRM	switched reluctance machine
VSI	voltage source inverter

Contents

Acknowledgements	i
Abstract	iii
Notation	vii
1 Introduction	1
1.1 Motivation	1
1.2 Applications	2
1.2.1 Machining Spindles	2
1.2.2 Medical Spindles	4
1.2.3 Turbocompressors	4
1.2.4 Gas Turbine Generators	5
1.2.5 Flywheels	6
1.2.6 Optical Systems	6
1.2.7 Other Applications	7
1.3 State of the Art	7
1.4 Challenges	9
1.5 Outline of the Thesis	9
1.6 Scientific Contributions	10
1.7 List of Publications	11

2	Machine Selection and Design	13
2.1	Selection	13
2.1.1	Machine Topology	13
2.1.2	Winding	14
2.1.3	Stator Core Material	15
2.1.4	Rotor Construction	16
2.1.5	Cross Section	16
2.2	Scaling	16
2.3	Modeling and Design	19
2.3.1	Mechanical Rotor Design	19
2.3.2	Magnetic Field Model	26
2.3.3	Loss Models	31
2.4	Optimization	35
2.4.1	Loss Minimization	35
2.4.2	Litz Wire Optimization	36
2.4.3	Results	37
2.5	Machine Model	46
2.5.1	Machine Data and Specifications	48
3	Power and Control Electronics	49
3.1	Topology Selection	49
3.1.1	Requirements	49
3.1.2	Topology Candidates	50
3.1.3	PAM Inverter	55
3.2	Sensorless Rotor Position Detection	61
3.3	Control	65
3.3.1	Torque Generation	67
4	System Integration	69
4.1	Bearing Technology	69
4.1.1	Requirements	69
4.1.2	Bearing Types	70

4.1.3	Application Examples	72
4.2	Thermal Design	72
4.3	Rotordynamics	74
4.3.1	Motivation	74
4.3.2	Modeling	76
4.3.3	Results	81
5	Experimental Results	85
5.1	Hardware	85
5.1.1	1 Million rpm System	85
5.1.2	500 krpm System	86
5.2	Power and Control Electronics Measurements	88
5.3	Machine Measurement Methods and Results	88
5.3.1	Machine Resistance and Inductance Measurements	89
5.3.2	Back EMF Measurement	90
5.3.3	Reaction Torque Measurement	91
5.3.4	Deceleration Test	91
5.3.5	Machine Efficiency	94
6	Conclusion	97
6.1	Summary	97
6.2	Outlook	99
	Bibliography	100
	Curriculum Vitæ	109

Chapter 1

Introduction

1.1 Motivation

The Solar Impulse project aims to build an airplane which takes off and flies autonomously, day and night, propelled uniquely by solar energy, right round the world without fuel or pollution. During the day, it stores energy not only in batteries but also in altitude and climbs up to 12000 m, where the pilot is in need for a cabin air pressurization system. Using standard compressors would penalize the airplane with an approximately additional weight of 20 kg. Using an ultra-high-speed, 500 000 revolutions per minute (rpm) turbocompressor directly driven by an electrical motor, the weight of the cabin pressurization system can be reduced to 0.2 kg.

Conventional high-speed dental handpieces are driven by air turbines or low speed electrical motors with gearboxes. Replacing this technology with a high-speed, direct electrical drive leads to a reduction of different handpieces, lower cost due to a simpler system without gearboxes and a better controllability.

Emerging mobile and remote systems, e.g. portable electronic devices, spacecrafts and satellites, or unmanned robots and airplanes, need more and more electrical power. For the power supply, the commonly used battery has the drawbacks of a limited energy density and a long recharging time. Compared to batteries, fuels offer a much higher energy density, and with an ultra-high-speed miniature gas turbine generator this chem-

ical energy can be converted to electrical energy in a small, lightweight, mesoscale system.

These are only three examples of what is possible with an ultra-high-speed electrical drive system. In the following, further applications with present and future speed requirements and output power ranges are indicated (section 1.2), an overview on existing research and development is given (section 1.3) and the challenges of designing an ultra-high-speed electrical drive system are outlined (section 1.4).

1.2 Applications

All the described applications have the common future requirements for higher rotational speeds and/or increased compactness (which again is a result of higher rotational speed). However, not only high rotational speeds, but the combination of high rotational speeds and high power is the main challenge in both applications and electrical machines. Therefore, some applications and their trends, existing systems, and the research focus of this Thesis in the area of emerging applications can be depicted in the power-speed plane as shown in Figure 1.1.

1.2.1 Machining Spindles

The recent trend in mechanical systems has been towards smaller sizes, which in turns requires high precision manufacturing. To accomplish this high precision requires the use of smaller and higher speed drilling, milling and grinding tools [3]. For example, notch grinding of silicon wafers requires motor speeds of up to 150 000 rpm [4].

In the electronics industry, the trend has been for reduced sized electronic packages with an ever increasing pin count. For example, there are now fine-pitch ball grid arrays that have over 1700 pins. The PCB has to connect all these pins to the rest of the electrical circuit and this is achieved by using multiple layers (up to 12 layers). The interconnections between the layers is provided by through-hole vias or more recently microvias. Reducing the diameter of the vias allows for more interconnections and facilitates the high pin count components. Presently, both through- and microvias with diameters of 75 μm can be produced economically with mechanical PCB drilling spindles that operate with

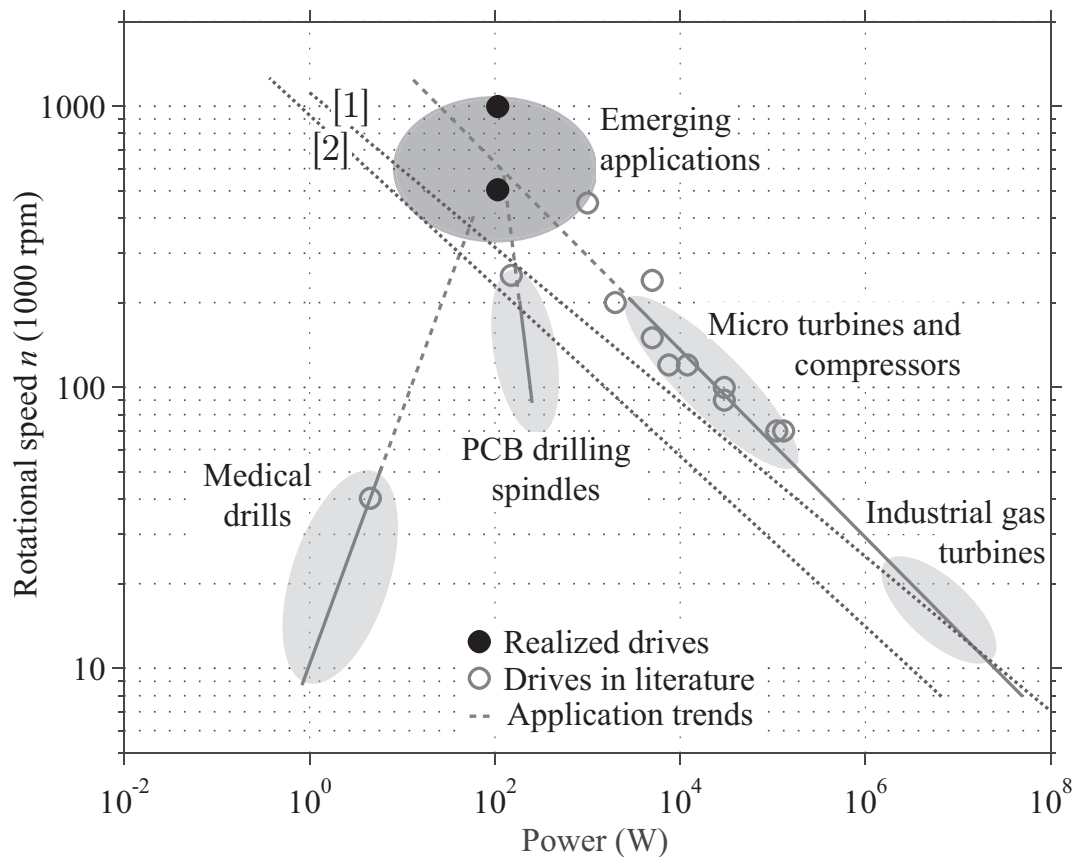


Figure 1.1: Emerging application areas, trends and existing electrical drive systems. Two scaling laws (see section 2.2) for electrical machines are plotted ([1] and [2]), and the two hardware demonstrator systems realized and analyzed in this Thesis are shown (see section 5.1).

speeds of up to 250 000 rpm and with a motor power of 200 W [5]. To provide interconnections for larger pin count components requires the use of smaller diameter microvias. Presently, the smallest microvias have hole diameters of $25 \mu\text{m}$, although $10 \mu\text{m}$ hole sizes are being investigated. For these hole diameters currently only laser drilling is possible, however the main disadvantage with laser drilling is the capital cost. Therefore, it is desirable to use cheaper mechanical drilling, but in order to maintain the same cutting speeds and productivity the rotational drill speed must be increased. For $10 \mu\text{m}$ hole diameters the drilling speed must be increased to over 1 million rpm [6].

1.2.2 Medical Spindles

The majority of today's dental drill handpieces are powered by an air turbine from a compressed air supply. Therefore, each hand piece is designed to operate at a single speed and accurate speed control is not possible. A typical dentist would require up to five different handpieces to cover the various tool speed ranges. By replacing the air spindle with an adjustable speed electrical drive can reduce the number of handpieces, with the added benefit of accurate speed and torque control. The major challenge is to reduce the size of the electrical machine to fit into a normal sized handpiece and still guarantee high torque for the low speed treatments.

In the high-speed range, air turbine handpieces with power levels between 10 W and 20 W operate up to 400 000 rpm. The currently available electrical powered hand pieces operate their electric motors up to a maximum of 40 000 rpm, and then a triple-gear system steps the speed up to a maximum of 200 000 rpm. In order to simplify these electric handpieces, the gearbox can be avoided with a direct drive. However, this requires a speed increase of a factor of 5 to 10 compared to today's electric motors. The increased speed would also allow a smaller machine design, and therefore providing greater flexibility in the design of an ergonomic handpiece.

1.2.3 Turbocompressors

Recent environmental concerns have resulted in increased research activity into the improvement of automotive fuel efficiency. A major thrust has been in the development of hydrogen based fuel cells for propulsion systems. These fuel cells require a constant supply of pressurized air that is provided by an air compressor system, which consumes around 5-10% of the fuel cell output power. To achieve a compact size, it has been reported that the compressor speed is increased to 120 000 rpm at a power level of up to 12 kW [7]. Future fuel cells with lower power ratings, and therefore lower compressors power ratings, will employ even higher-speed air compressors.

In a conventional automotive heating, ventilation and air conditioning (HVAC) system the compressor, which is the heart of an HVAC system, is directly connected to the combustion engine. This results in an increasing

load on the engine while decreasing the fuel efficiency of the vehicle. In the future, electrical compressors will be preferred over traditional compressors due to improved fuel efficiency. With turbocompressors instead of scroll compressors and an increase in speed these systems can be built much smaller and lighter. Furthermore, flexible packaging of the system is possible as the compressor works independently of the engine. This is a requirement for hybrid and all-electrical cars.

To increase the fuel economy and reduce the CO₂ production of the average car, there has been the trend of developing smaller capacity internal combustion engines, both of the gasoline and diesel types. In order to provide a higher performance and improved efficiency a turbocharger is employed. Turbochargers do not perform well at low engine speeds and a turbo lag or a delay in the air boost exists. Electrically assisted turbochargers are under investigation, which provide the pressure boost at low speeds [8]. An electrical machine is mounted on the same shaft between the turbine and the compressor. The electrical machine has to operate at the same rotational speeds of the turbocharger up to 200 000 rpm. The major drawback of the electrically assisted turbocharger is that the electrical machine must operate at extremely high temperatures since there is a direct connection to the exhaust gas turbine. Therefore, there have been developments of a separate air compressor that operates together with the turbocharger to provide additional boost at low engine speeds [9]. Increasing the compressor to higher speeds would result in a reduced volume and weight, which is especially important in smaller engine compartments.

1.2.4 Gas Turbine Generators

Gas turbine power generation is commonly used in large scale power generation systems up to 100's of MW, where the rotational speed is in the order of 10 000 rpm (Figure 1.1). There are emerging applications for portable, low power, gas turbine based power generation systems. One particular application is for the modern soldier, who now carries electrical equipment with a power consumption of up to 100 W. The existing heavy battery energy storage system, which also needs recharging, could therefore be replaced with a fuel based gas turbine system. At these power levels the gas turbine system occupies a very small volume if the rotational speeds are increased to over 500 000 rpm [10]. Significant chal-

Challenges exist in manufacturing the gas turbine and the electrical machine. For power levels of less than 10 W the trend is for speeds to over 1 million rpm where the construction uses micro-electrical-mechanical system (MEMS) techniques [11], [12]. Additional applications for small portable power supplies are in unmanned surveillance vehicles, autonomous robots and medical applications. Stanford University, in cooperation with M-DOT, has been developing a gas turbine with a predicted output power of 200 W and a rotational speed of up to 800 000 rpm [13]. The main application is for powering micro air vehicles.

1.2.5 Flywheels

Flywheels have long been used to store energy. In order to store and extract electrical energy a motor/generator is attached to the flywheel. The modern flywheel systems tend to operate in a vacuum and use magnetic bearings to reduce frictional losses. Two types of flywheel energy storage system exist, those with a large mass and low rotational speeds (<10 000 rpm) and those with low mass and high rotational speeds (>10 000 rpm) [14]. Special applications exist in the aerospace industry for low mass, high speed flywheel systems. In particular, NASA is investigating their use for both attitude control and energy storage in satellites and the international space station. As part of a research project a 3 kW, 40 000 rpm flywheel energy storage system has been tested that also provides attitude control. For the next generation of small, near earth orbit satellites the power requirements are reduced as well as the maximum weight. Research into a 100 W, up to 300 000 rpm flywheel motor/generator has been undertaken [15].

1.2.6 Optical Systems

In several optical systems, mirrors have to be rotated with very high speed in order to divert a light source such as a laser beam or a full picture. Applications are scanners, high-speed cameras, and laser systems. Usually, these mirrors are driven by air or helium turbines, however, due to the same reasons as for medical drills, there are advantages in replacing them with electric drive systems. In [16], in order to facilitate the depth scanning of human retinas through reflectometry measurements from coherent light sources, a transparent cube needs to be rotated at very high

speeds. Rotating mirror cameras use mirrors with speeds of up to 1.2 million rpm in order to generate up to 25 Million frames per second [17].

1.2.7 Other Applications

A number of other applications for ultra-high-speed electrical drives exist including those in the field of mega-gravity science. This is the study of solids and liquids under high acceleration (and temperatures). An ultra-centrifuge has been reported that produces an acceleration of 1 million times gravity through the use of a 220 000 rpm air turbine [18]. It describes that electrical drive centrifuges exist with maximum speeds up to 120 000 rpm, although there is no reason why this can not be increased with the correct design.

1.3 State of the Art

A number of research groups are investigating the different application areas for high speed electrical machines and drive systems. The most challenging aspects for the research occur when the operating speed is above 100 000 rpm.

In [19], various gas turbine and compressors systems are reported. The design target is for 240 000 rpm at a power level of 5 kW. Currently, the system is operating at 180 000 rpm at no load. A fuel cell air compressor operating at 120 000 rpm and 12 kW has been reported [7]. In [20], a 1 kW generator operating at 452 000 rpm has been reported as the world's fastest PM brushless dc motor/generator in production. At the lower power level, MIT has had research efforts in developing portable power gas turbines on a micro scale [11]. The target speed for their electric generator speed is 1.2 million rpm, while they have presently achieved 15 000 rpm. A micro fabricated axial-flux permanent magnetic generator has been reported in [21] and [22]. The generator has been fabricated using a combination of micro fabrication and precision machining. At a rotational speed of 120 000 rpm, the generator produced 2.5 W of electrical power.

For dental hand pieces, [23] reported on a design target of 150 000 rpm at a power level of 10 W. This was constructed and the target achieved. In the application area of machining tools, a design target of 150 000 rpm,

5 kW is reported [3]. The achieved speed is 100 000 rpm at no load and 60 000 rpm under load. Commercially available products, i.e. from [5] or [24], obtain speeds of around 200 000 rpm at power levels between 200 W and 900 W. Application areas for these machines include grinding and PCB drilling. For the electrically assisted turbocharger reported in [8], the target speed for the electric drive is 120 000 rpm at a power level of 7.5 kW. However, no experimental results have been reported. In the area of energy storage and attitude control flywheels for aerospace applications, the only reported system above 100 000 rpm is that in [15]. The design target is 300 000 rpm at a power level of 100 W, however only 32 000 rpm in a test run have been currently achieved.

Rotating machinery without electrical drive system is out of the scope of this Thesis. However, there are a few interesting research projects and industrial applications on air or gas turbine driven shafts with speeds above 500 000 rpm. In the MIT project mentioned earlier, a speed of 1.4 million rpm has been achieved with a compressed air driven wafer turbine [25]. In a similar project, but with conventional manufacturing, a dummy gas turbine rotor on hydroinertia gas bearings has been tested up to 770 000 rpm [26]. In order to prove the feasibility of their compliant surface foil bearings, MiTi has spun a rotor up to 700 000 rpm with an air turbine [27]. Beside these three test bench setups, there is also an industrial application running on very high speed. The highest speed mirror in a Cordin high-speed camera rotates with up to 1.2 million rpm driven by a helium turbine [17].

In 1946, Beams presented an experiment in which he spun steel balls up to 23 million rpm in order to test the material properties under a high centrifugal field [28]. To the authors knowledge, this is the highest rotational speed achieved with any kind of rotating setup, although it is not entirely clear from literature if the highest speed achieved was lower or even higher than the mentioned 386 kHz. Recently, in [29] the experiment has been revived, and a rotational speed of 2 880 000 rpm has been achieved. In both experimental setups, the balls were supported magnetically in vacuum and spun with a rotating magnetic field. Although the balls were spun similar to an induction drive with magnetic fields excited by an electrical circuit, this physical experiment is not considered an electrical drive system as it has no possibility of driving an application.

In summary, commercial electrical drive systems are readily available at speeds below 100 000 rpm. Above 100 000 rpm and less than

250 000 rpm special industrial drives are available. The highest reported speed is 452 000 rpm at 1 kW [20] although very little information is available on its application. Above 500 000 rpm there are only a handful of pure research projects being undertaken, although there have not been conclusive results.

1.4 Challenges

The design, construction and testing of ultra-high-speed electrical drive systems is not trivial. The main challenges are

- The reduction of the high-frequency losses in the machine design, mainly the eddy current losses in copper and iron, and the air friction losses.
- The selection and design of a high-speed rotor construction that withstands the mechanical stresses.
- The selection of a suitable power electronics topology for driving ultra-high-speed machines is needed. Depending on the application the power electronics have to be compact.
- A sensorless rotor position detection method that can operate at speeds beyond 1 million rpm
- An application dependent system integration that includes the selection of the correct bearing technology, a sophisticated thermal design and the analysis of rotor dynamics.

1.5 Outline of the Thesis

The goal of this Thesis is the evaluation, design and experimental testing of an ultra-high-speed electrical drive system. The focus is on the evaluation and new concepts of machine types, inverter topologies and control methods. The final result is the best combination of the parts in order to realize an ultra-high-speed electrical drive system with highest efficiency and power density.

After this introduction (chapter 1), chapter 2 presents the machine selection, scaling laws, the mechanical and the electromagnetic modeling and design, and finally - integrating all these models - the optimization for lowest losses.

In chapter 3 different power electronics topologies are compared and a suitable topology is selected. Furthermore, a sensorless rotor position detection for highest speeds is presented.

Chapter 4 compiles the information on bearing technologies suitable for high-speed rotors. The thermal design and the rotor dynamic analysis are shown based on an application example.

In chapter 5 two hardware prototypes, a 1 million rpm drive system demonstrator and a 500 000 rpm turbocompressor drive system, are analyzed experimentally. It is shown that applications (in this case a turbocompressor system) with 500 000 rpm are feasible and rotational speeds beyond 1 million rpm can be achieved with electrical drive systems.

Finally, in chapter 6 the results of this Thesis are concluded and an outlook is given.

1.6 Scientific Contributions

The following list summarizes the main contributions presented in this Thesis.

- Scaling laws for machines, an overview of international ultra-high-speed electrical drive system research, and future emerging applications are compiled in [I].
- Evaluation, comparison and selection methods for electrical drive systems for ultra-high speed operation are proposed. The methods not only consider the individual parts, machine or power electronics, but the entire drive system. The machine selection method is presented in [II] and [III], the power electronics topology selection is presented in [IV] and the chosen drive system is presented in [V].
- In traditional machine design methods, only dc copper and iron losses are considered. However, for ultra-high-speed machines additional high-frequency losses become dominant. Therefore, in [VI],

analytical loss models for skin and proximity effect copper losses and air friction losses are compiled. Furthermore, a novel, analytical optimization method for the selected machine has been developed. Furthermore, the loss models have been experimentally validated in [VII].

- A sensorless control method for highest speeds, partly presented in earlier literature, was developed and is presented in [VIII].

1.7 List of Publications

A selection of publications originating from this Ph.D. project are:

- [I] C. Zwyssig, J. W. Kolar, and S. D. Round, “Megasppeed drive systems: pushing beyond 1 million r/min,” *IEEE/ASME Transactions on Mechatronics*, accepted for future publication.
- [II] C. Zwyssig, J. W. Kolar, W. Thaler, and M. Vohrer, “Design of a 100 W, 500000 rpm permanent-magnet generator for mesoscale gas turbines,” in *Proceedings of Fourtieth IEEE Industry Applications Society Annual Meeting (IAS '05)*, vol. 1, 2005, pp. 253–260.
- [III] C. Zwyssig and J. W. Kolar, “Design considerations and experimental results of a 100 W, 500 000 rpm electrical generator,” in *Journal of Micromechanics and Microengineering*, vol. 16, no. 9, Sep. 2006, pp. 297–302.
- [IV] C. Zwyssig, S. D. Round, and J. W. Kolar, “Power electronics interface for a 100 W, 500000 rpm gas turbine portable power unit,” in *Proceedings of 21st Annual IEEE Applied Power Electronics Conference and Exposition (APEC '06)*, 2006, pp. 283–289.
- [V] C. Zwyssig, S. D. Round, and J. W. Kolar, “An ultrahigh-speed, low power electrical drive system,” *IEEE Transactions on Industrial Electronics*, vol. 55, no. 2, pp. 577–585, Feb. 2008.
- [VI] J. Luomi, C. Zwyssig, A. Looser, and J. W. Kolar, “Efficiency optimization of a 100-W 500 000-r/min permanent-magnet machine including air-friction losses,” *IEEE Transactions on Industry Applications*, vol. 45, no. 4, pp. 1368–1377, Jul.–Aug. 2009.

- [VII] C. Zwyssig, S. D. Round, and J. W. Kolar, “Analytical and experimental investigation of a low torque, ultra-high speed drive system,” in *Proceedings of 41st IEEE Industry Applications Society Annual Meeting (IAS '06)*, vol. 3, 2006, pp. 1507–1513.
- [VIII] C. Zwyssig, M. Duerr, D. Hassler, and J. W. Kolar, “An ultra-high-speed, 500000 rpm, 1 kW electrical drive system,” in *Proceedings of Power Conversion Conference (PCC '07)*, 2007, pp. 1577–1583.

Chapter 2

Machine Selection and Design

2.1 Selection

2.1.1 Machine Topology

There are two basic concepts of electromechanical energy conversions, machines based either on electric or magnetic fields. At the required power level and for the expected machine dimensions in the millimeter range, a magnetic machine is the better choice [30]. The rated current of a magnetic machine scales proportional with the machine dimensions [31]. Therefore, the flux density in an electrically excited motor, e.g. induction machines (IM) or switched reluctance machines (SRM), decreases with decreasing size. In contrary, permanent magnet flux density remains constant for decreasing machine volume. Therefore, only permanent magnet machines are considered with the aim for a low system volume. High-speed operation requires a simple and robust rotor geometry and construction. A commutation system employed for the current commutation in dc machines produces additional friction and limits the speed (to typically 35 000 rpm). Therefore, the only machine types left that meet both small size and high-speed requirements are the brushless dc (BLDC) machine, fed by square-wave currents, and the identically con-

structured permanent-magnet synchronous machine (PMSM), fed by sinusoidal currents. The lowest possible fundamental electrical frequency is the mechanical frequency. Therefore, a two pole rotor is chosen.

2.1.2 Winding

For these permanent-magnet machines both slotless and slotted stators could be employed. In [32] the slotless configuration is found to be the better choice for high-speed operation because of the simpler manufacturing of the stator core and the reduction of eddy current losses in the rotor (no slotting harmonics and lower armature current reaction).

There are several possibilities for an air-gap winding in a slotless configuration:

- Trapezoidal, cup-shaped, self-supporting, surface winding, presented for example in [33]. This winding has the advantage of very small or no end windings, the disadvantage is a winding factor of approximately 0.5, and a manufacturing that needs special equipment.
- Skewed, cup-shaped, self-supporting winding, as for example presented in [34]. These windings are based on the expired Faulhaber patent, and has the same advantages and disadvantages as the first winding configuration.
- Straight winding, usually on a winding carrier, presented for example in [32]. This configuration has the advantage of an easy manufacturing and a winding factor close to 1, but the disadvantage of usually big end windings which need an axial and radial extension of the machine.
- Toroidal, ring-wound configuration, as presented in [35] and [36]. This winding type has the same advantage of the straight winding, with smaller end windings in axial direction, but end windings on the outer side of the stator core that extend the machine in radial direction.

For ultra-high-speed machinery, the geometrical constraints of the electrical machine are usually given by the application specifications, system integration aspects such as rotordynamics and thermal analysis, and

	Density (g/cm ³)	Curie temp. (°C)	Rel. perm. (μ_r)	Sat. (T)	Losses (W/cm ³)
Si-Fe	7.6	740	2000	1.7	3.5
Amorphous	7.29	358	20000	1.41	0.15
Nanocrystalline	7.3	570	70000	1.3	0.03
Ferrite	4.85	120	15000	0.5	0.18
Ni-Fe	8.2	310	80000	1.48	0.75
SMC	3.18	450	500	2	2.8

Table 2.1: Core material properties. The losses are calculated for a flux density of 0.5 T and a frequency of 10 kHz.

mechanical stress limitation. An important constraint is the usually limited axial length of the machine to avoid low critical speeds of the entire rotor configuration. Therefore, a winding type with short end windings is important and the skewed, cup-shaped, self supporting winding is chosen.

2.1.3 Stator Core Material

In high-speed electrical machines the iron losses usually outweigh the copper losses, therefore the choice of a stator core material with low high-frequency losses is essential. Due to the large magnetic air gap in slotless machines, the flux density in the stator core is usually low, therefore a lower saturation flux density than in standard machines is acceptable. The state-of-the-art materials used in high-speed machines today are thin silicon-iron (Si-Fe) laminations, nickel-iron (Ni-Fe) laminations, or also Soft Magnetic Composites (SMC) have been reported. However, there also exist magnetic materials used in high-frequency inductors and transformers, such as high-flux ferrites, and amorphous and nanocrystalline iron-based ribbons. For a first comparison, all materials are listed in Table 2.1 for an operating point of a peak flux density of 0.5 T and a frequency of 10 kHz.

It can be seen that the standard silicon-iron laminations have the highest losses. However, SMC has almost no advantage concerning losses and a big disadvantage due to the low relative permeability. Its use is especially in machines with a 3D flux path, where laminations cannot

be used. The saturation flux density of even high-flux ferrites is too low for building compact machines. The nickel-iron laminations are better for high-frequency than the standard silicon-iron. However, for almost the same saturation flux density, the amorphous and especially the nanocrystalline iron-based alloy offers much lower losses. Both reduce the iron losses compared to the silicon-iron losses by a factor of more than 20. Amorphous iron based alloys are cheaper and more easily available (e.g. as Metglas from Hitachi or Vitrovac from Vacuumschmelze) than nanocrystalline materials, therefore it is the preferred material.

2.1.4 Rotor Construction

In high-speed permanent-magnet machine rotors the magnets are usually retained by a carbon fiber or metal sleeve, in order to reduce the stresses on the brittle permanent magnet. For this two-pole rotor, a single permanent magnet can be used, which simplifies the rotor construction. Instead of the usual shaft in the center of the rotor, a cylindrical permanent magnet without hole is chosen. The retaining sleeve therefore has two functions: The torque transfer (as the usual shaft) and the stress limitation for the permanent magnet.

2.1.5 Cross Section

In Figure 2.1 a cross section view of the chosen machine is shown. The rotor consists of a one-piece permanent magnet that is diametrically magnetized. The stresses on this brittle magnet is limited by a retaining titanium sleeve that also acts as torque-transferring shaft. The slotless stator consist of a three-phase winding placed in the air-gap, and a cylindrical stator core.

2.2 Scaling

The power S available from an electrical machine can be written as

$$S = CD_r^2 Ln \tag{2.1}$$

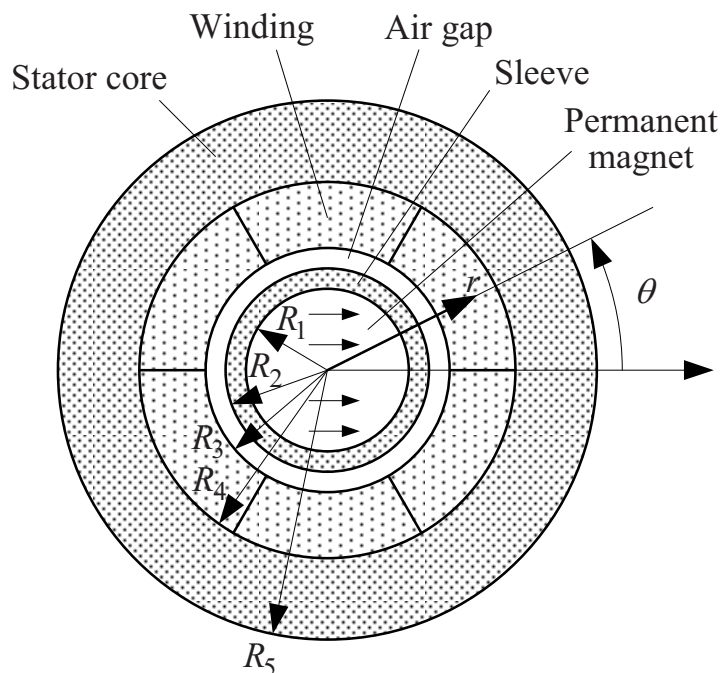


Figure 2.1: Machine cross-section and symbol definitions: diametrically magnetized cylindrical permanent magnet rotor inside a slotless stator.

where D_r is the rotor diameter, L the active length and n the rotational speed (in Hz or rpm, depending on the definition of C). Esson's utilization factor C is dependent on the machine type, and other various variables such as the cooling system and size of the machine [1], [31]. Using given data for small permanent-magnet machines, e.g. given in [31], and the relationship in (2.1), the active volume of the machine can be estimated for a given power and speed. For constant power, the volume of a machine decreases with increasing speed, which leads to very small machines for ultra-high speeds, see section 2.4.3.

Furthermore, for a given speed, the diameter of a rotor is limited by the rotor geometry, and the strength and densities of the rotor materials. For a solid disk the maximal diameter is

$$D_{max} = \frac{2}{\omega} \sqrt{\frac{8\sigma_{UTS}}{(\nu + 3)\rho}} \propto \frac{1}{n} \sqrt{\frac{\sigma_{UTS}}{\rho}} \quad (2.2)$$

where σ_{UTS} is the tensile strength and ρ the density of the material. With a maximal length to diameter ratio λ_{max} ($L_{max} = \lambda_{max} D_{max}$) and (2.1)

this leads to a relationship of speed and maximal available power of

$$P \propto C \frac{1}{n^2}. \quad (2.3)$$

For smaller machines the utilization factor C is smaller due to higher tolerances and limits in manufacturing. Furthermore, for higher speeds eddy-current losses in copper and iron as well as friction losses in air and bearing increase, which has to be compensated for with a lower flux densities and lower currents. This leads to a lower utilization factor with increasing speed, i.e.

$$C \propto \frac{1}{n^\gamma}. \quad (2.4)$$

Different values for γ have been identified, leading to different scaling factors, for example in [1] ($P \propto 1/n^{3.6}$) and [2] ($P \propto 1/n^{3.3}$). The lines are shown in Figure 1.1. Therefore, the term ultra-high-speed not only implies high-speed operation, but a combination of speed and power. Both an electrical machine running at 10 000 rpm at a power level of 10 MW and a machine running at 1 000 000 rpm with a power level of 100 W can be defined as ultra-high-speed machines. According to (2.2) another way of defining ultra-high-speed operation is according to the surface speed $\omega D_{max}/2$, which is limited by the material properties and the rotor geometry.

Scaling a machine with a constant power rating and efficiency, and therefore constant losses, to higher speeds leads to increased losses per surface area, since the size of the machine decreases. This leads to lower utilization factors C and the need for more sophisticated thermal designs for ultra-high-speed machines.

As an example, the machine volume for a permanent-magnet machine with a rated speed of 500 000 rpm and a rated power of 100 W can be estimated with utilization factors determined by investigating existing small permanent-magnet motors in [31]. There, a torque-per-volume constant of $C = 0.0006 \text{ Nm/cm}^3$ is identified. It is found that the friction (mechanical friction and magnetic stator core losses) is approximately 5% of the generated torque, although there is a wide variation for the analyzed motors. With a friction of 10% of the produced torque, the machine volume V is estimated to

$$V = 1.1 \frac{60}{2\pi} \frac{100 \text{ W}}{500\,000 \text{ rpm}} \frac{1}{C} = 3.5 \text{ cm}^3 \quad (2.5)$$

2.3 Modeling and Design

2.3.1 Mechanical Rotor Design

Requirements

The rotor construction shown in Figure 2.1 has to be designed such that the following specifications are fulfilled in the entire operation speed area:

- The torque transfer and low eccentricity are guaranteed by allowing no lift-off of the sleeve. Thus the radial stress at the interface between the permanent magnet and the sleeve has to be negative (which equals pressure), which is most critical at the maximum speed.
- The tensile stresses in the entire permanent magnet have a safety margin of 30% to the tensile strength of Sm_2Co_{17} (120 MPa). The most critical stress occurs at the maximum speed in the centre of the magnet.
- The von Mises stresses in the entire sleeve have a safety margin of 50% to the tensile strength of titanium (900 MPa). The most critical stress occurs at the maximum speed on the inner side of the sleeve.
- The sleeve has a minimum thickness (0.25 mm) for manufacturability reasons.

The stresses of the rotor construction with the permanent-magnet shrink-fitted into a titanium sleeve can be described with a two-dimensional mechanical model, either solved with an analytical approach or finite-element (FE) simulations.

Analytical Stress Model

According to [37] the general equations for displacement u , radial stress σ_r and tangential stress σ_θ in a rotating disk are

$$u = \frac{1}{E} \left((1 - \nu)C_0 r - (1 + \nu)C_1 \frac{1}{r} - \frac{1 - \nu^2}{8} \rho \omega^2 r^3 \right) \quad (2.6)$$

$$\sigma_r = C_0 + C_1 \frac{1}{r^2} - \frac{3 + \nu}{8} \rho \omega^2 r^2 \quad (2.7)$$

$$\sigma_\theta = C_0 - C_1 \frac{1}{r^2} - \frac{1 + 3\nu}{8} \rho \omega^2 r^2 \quad (2.8)$$

The constants C_0 and C_1 are determined from the boundary conditions. For a rotor construction with a cylindrical magnet encased in a retaining sleeve there is two sets of (2.6)-(2.8), one for the permanent magnet ($u_{pm}, \sigma_{r,pm}, \sigma_{\theta,pm}$) and one for the sleeve ($u_{sl}, \sigma_{r,sl}, \sigma_{\theta,sl}$). The radial stress at the interference $r = R_1$ must be the same for both permanent magnet and sleeve, the radial stress on the periphery $r = R_2$ is zero, the displacement in the center too and the difference of the displacement of sleeve and permanent magnet at the interference equals the interference fit Δu_0 . This leads to the boundary conditions

$$\sigma_{r,pm} = \sigma_{r,sl} \Big|_{r=R_1} \quad (2.9)$$

$$\sigma_{r,sl} = 0 \Big|_{r=R_2} \quad (2.10)$$

$$u_{sl} - u_{pm} = \Delta u_0 \Big|_{r=R_1} \quad (2.11)$$

$$u_{pm} = 0 \Big|_{r=0} \Rightarrow C_{1,pm} = 0 \quad (2.12)$$

These ten equations can be solved for the ten variables ($u_{pm}, \sigma_{r,pm}, \sigma_{\theta,pm}, u_{sl}, \sigma_{r,sl}, \sigma_{\theta,sl}, C_{sl}, C_{pm}, C_{1,pm}, C_{1,sl}$). For ductile materials usually the von Mises yield criterion is used to estimate the yield criteria, which states that the von Mises stress σ_v has to be smaller than the ten-

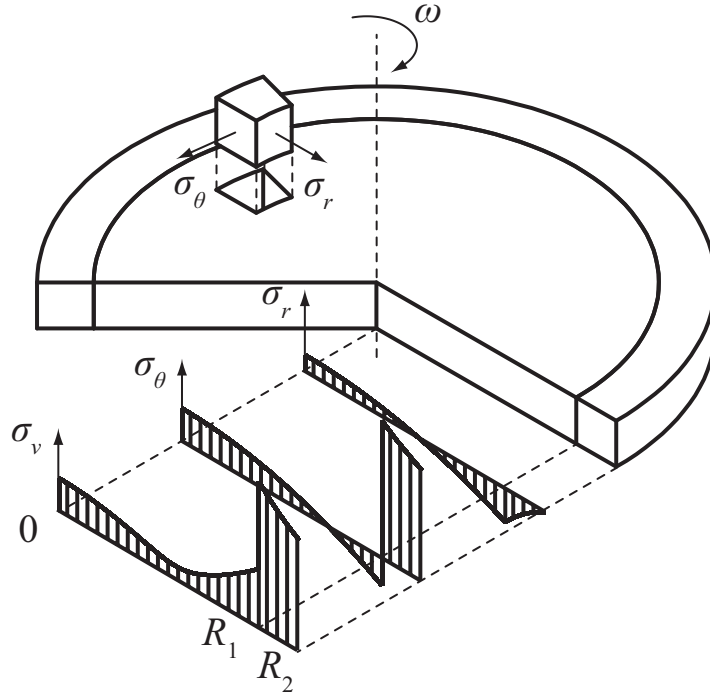


Figure 2.2: Stresses distribution for a cylindrical magnet encased in a sleeve under rotation.

stiffness of the material. In the case of planar stresses the von Mises stress can be calculated with

$$\sigma_v = \sqrt{\sigma_r^2 + \sigma_\theta^2 - \sigma_r \sigma_\theta} \quad (2.13)$$

For brittle materials (such as the permanent magnet) the von Mises yield criterion or the maximum principal stress theory, which states that the largest principal stress has to be smaller than the tensile strength, is used. The typical stress distribution for a cylindrical magnet encased in a sleeve is shown in Figure 2.2.

Shrink Fit

For the shrink fit of a sleeve onto the magnet, usually the sleeve is heated up and the magnet is cooled. The thermal expansion can be calculated with

$$\Delta u = \alpha_{th} R_1 \Delta T \quad (2.14)$$

		Permanent magnet	Titanium sleeve
Young's modulus	E	104 GPa	114 GPa
Poisson's ratio	ν	0.28	0.35
Density	ρ	8.3 g/cm ³	4.43 g/cm ³

Table 2.2: Mechanical data of the rotor.

Both titanium and Samarium-Cobalt have a coefficient of thermal expansion (CTE) α_{th} of around $10 \mu\text{mm}^{-1}\text{K}^{-1}$. The magnet can be cooled to almost -200°C with liquid nitrogen and the maximal allowable titanium temperature of 600°C a length difference of $8 \mu\text{m}$ per mm radius can be achieved. For example for a permanent-magnet radius $R_1 = 2.5 \text{ mm}$ a maximal radial interference $\Delta u_0 = 20 \mu\text{m}$ can be achieved.

Results

The results of the mechanical rotor design are presented for the 500 krpm machine (see section 5.1.2) which has a rotor with a permanent-magnet radius R_1 of 2.5 mm and a rotor radius R_2 of 3 mm. The radial interference of magnet and sleeve is $\Delta u_0 = 7.5 \mu\text{m}$. The rotor is part of a machine with a rated speed of 500 000 rpm and a rated power of 100 W. The mechanical data for both rotor magnet and sleeve are given in Table 2.2.

Figure 2.3 shows the radial displacement and the stress distribution at standstill and the rated rotational speed of 500 000 rpm. In the displacement curves it can be seen that the rotor radius is enlarged due to the shrink fit by slightly more than $6 \mu\text{m}$ and is further increased by about $0.6 \mu\text{m}$ due to the stresses at rated speed. At standstill, the magnet is compressed by about $0.7 \mu\text{m}$, whereas at rated speed it is almost back to its original state with zero displacement over the entire radius and only the sleeve is displaced. From the stress distribution it can be seen that at standstill in the magnet radial and tangential stress are equal and constant over the entire radius. In the sleeve there is compressive stress in radial direction and tensile stress in tangential direction. The tangential stress increases to 325 N/mm^2 , which, with a low radial stress of -40 N/mm^2 , leads to a von Mises stress of 347 N/mm^2 , which is well below the tensile strength of titanium. The radial stress at the interfer-

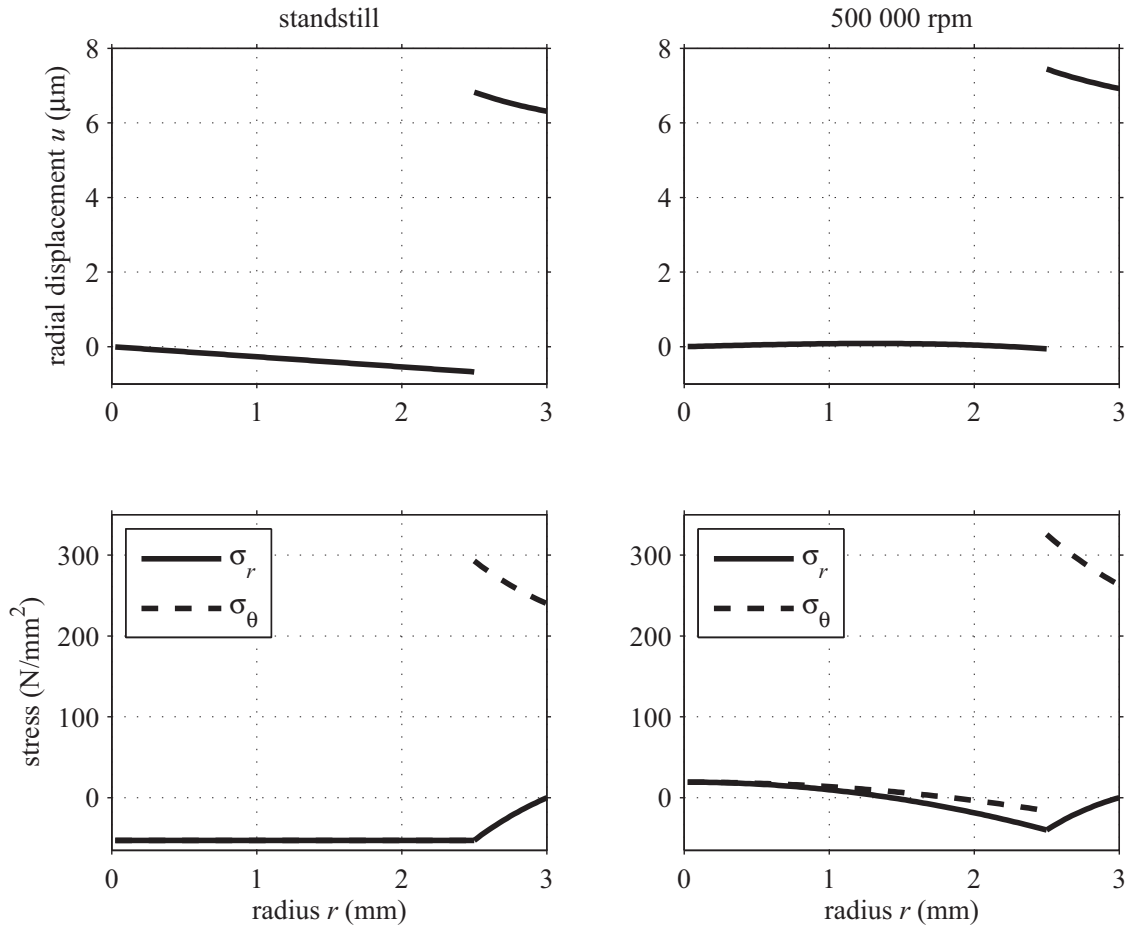


Figure 2.3: Radial displacement and stress distribution at standstill and a rotational speed of 500 000 rpm in a rotor with a magnet radius $R_1 = 2.5$ mm, a rotor radius $R_2 = 3$ mm and a radial interference fit $\Delta u_0 = 7.5$ μm.

ence of permanent magnet and titanium sleeve is negative also at rated speed, which means compression, and this leads to torque transfer and a stable rotor construction. The maximal tensile stress in the permanent magnet is very low with 19 N/mm². The higher compressive stress of -50 N/mm² is no problem for the magnet.

The comparison with FE simulations show a good agreement. In Figure 2.4 the von Mises stresses are shown for a quarter of the described rotor. The maximal von Mises stresses on the inner side of the sleeve are 330 N/mm² for standstill and 350 N/mm² for rated speed. The stresses in the magnet are sufficiently low.

If the permanent-magnet radius is a free parameters - i.e. if it is determined by an outside design routine, e.g. by the optimization routine

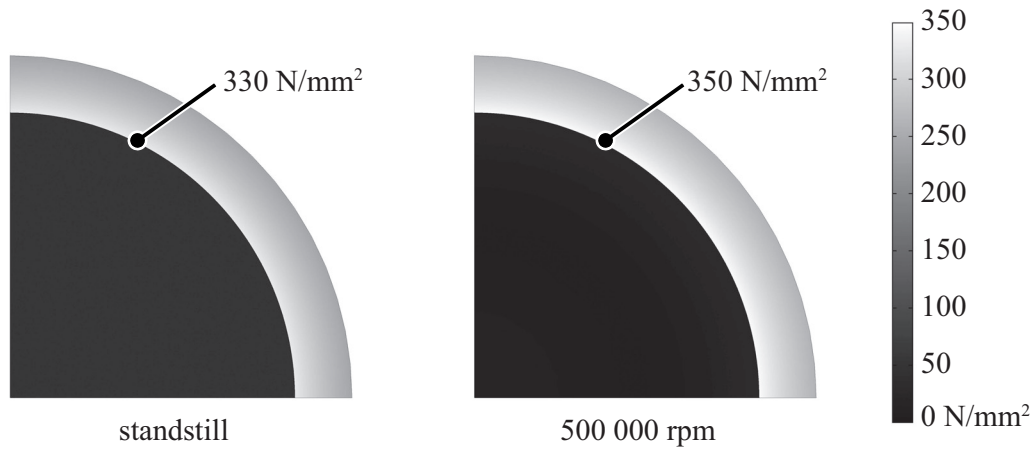


Figure 2.4: Von Mises stresses determined with FE simulations in a quarter of a rotor with a magnet radius $R_1 = 2.5$ mm, a rotor radius $R_2 = 3$ mm and a radial interference fit $\Delta u_0 = 7.5$ μm .

presented in section 2.4 - the sleeve thickness $R_2 - R_1$ and the interference fit Δu_0 can be calculated using the mechanical model and considering the requirements. The results are shown in Figure 2.5 for a rotor with a rated speed of 500 000 rpm. The stresses in the magnet are minimized. For small rotor radii, the sleeve thickness is at the minimum value defined by the manufacturability; the shrink fit ensures that the sleeve does not lift off, i.e. keeps the radial pressure at the interface negative. At 3 mm magnet radius, the stress in the magnet reaches its limit, and the interference fit has to be enforced to guarantee the safety margin to the tensile strength of Sm_2Co_{17} . At 3.3 mm, the stress in the titanium sleeve reaches its limit, and the sleeve thickness has to be increased in order to guarantee the safety margin to the tensile strength of titanium.

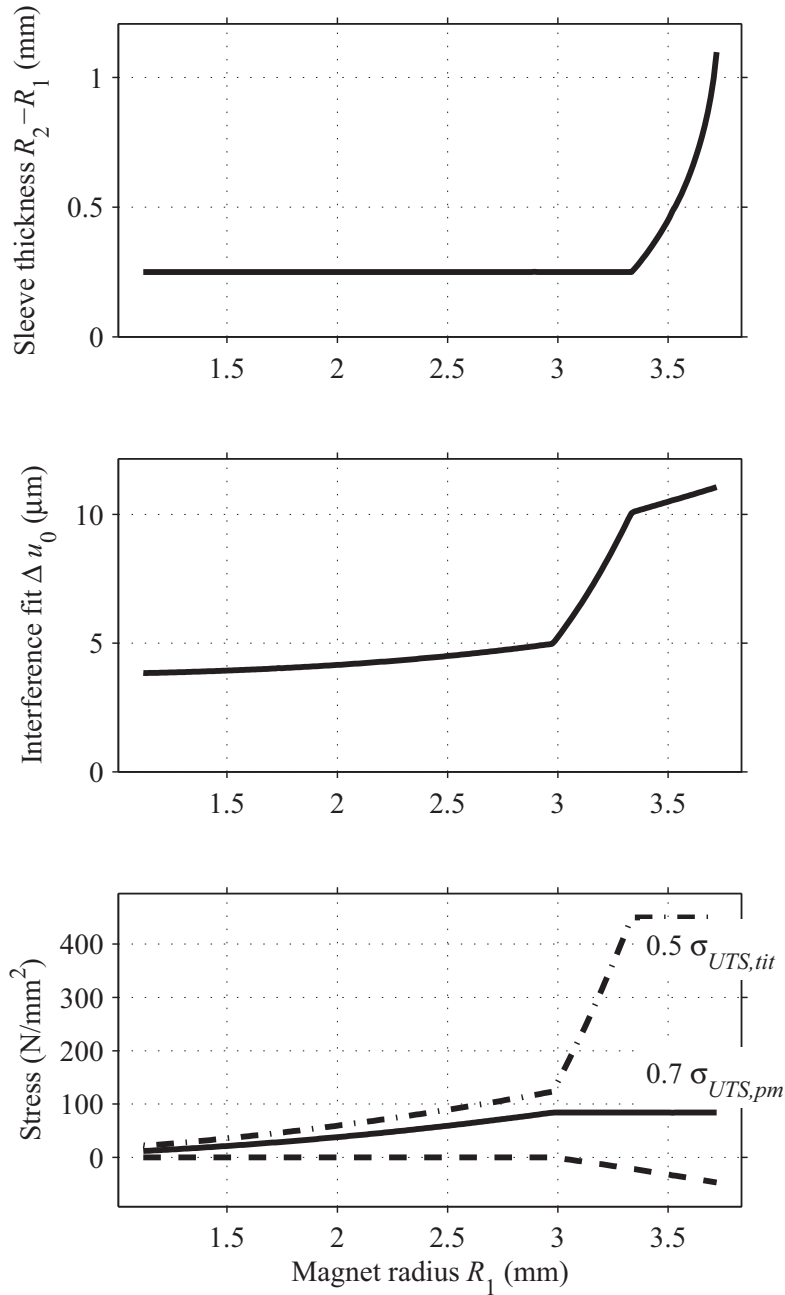


Figure 2.5: Results of mechanical analysis as function of rotor radius at 500 000 rpm. The first subfigure shows the sleeve thickness $R_2 - R_1$, the second subfigure shows the shrink fit Δu_0 , and the third subfigure shows the radial stress in the center of the permanent magnet (solid), the radial stress at the interface $r = R_1$ (dashed) and the tangential stress in the sleeve at $r = R_1$ (dash-dotted). The stress limits in the magnet and sleeve are 70% of $\sigma_{UTS,pm}$ (84 N/mm²), and 50% of $\sigma_{UTS,pm}$ (450 N/mm²) respectively.

2.3.2 Magnetic Field Model

A solution of the magnetic field is needed for analyzing the operating point, resistive losses, eddy current losses, and iron losses. Today, numerical analysis based on the FE method is the standard methodology for such calculations. However, analytical models can give more insight into the problem, they are in many cases computationally efficient, and result in smooth solutions, which is favorable in optimization. Analytical solutions of the magnetic field have been derived for permanent-magnet machines with radially magnetized magnets in the rotor, e.g., [38], [39]. Solutions for machines with diametrically magnetized rotors have been presented in [40], [41]. Usually, the permeability of the stator iron core has been assumed infinite when the magnetic field of a permanent-magnet machine is solved analytically, and the solution is restricted to the air gap and the rotor. However, an analytical model of the magnetic field in the stator core can be used for the evaluation of the iron loss distribution [42]. In the following, a solution of the magnetic field is derived for the entire cross-section of the machine, including the cylindrical stator core.

Problem Formulation

The cross section of the two-pole machine is illustrated in Figure 2.1. The symbols for the radial dimensions are: radius of the permanent magnet R_1 ; outer radius of the rotor sleeve R_2 ; inner radius of the stator winding R_3 ; and inner and outer radii of the stator core R_4 and R_5 , respectively. The length of the stator core is denoted by L , and the air gap is $\delta = R_3 - R_2$. A two-dimensional boundary value problem is formulated for the magnetic field, and the effects of the third dimension are ignored. The polar coordinate system fixed to the rotor cross-section is illustrated in Figure 2.1. The diametrically magnetized permanent magnet has a uniformly distributed remanence flux density \mathbf{B}_{rem} in the direction of $\theta = 0$. The magnetic flux density is given by

$$\mathbf{B} = \mu_0 \mathbf{M}_p + \mu_r \mu_0 \mathbf{H} \quad (2.15)$$

where \mathbf{M}_p is the permanent magnetization, \mathbf{H} is the magnetic field strength, and μ_r is the relative recoil permeability. The problem region is divided into three subregions. In the permanent magnet region

($0 \leq r \leq R_1$), $\mathbf{M}_p = \mathbf{B}_{rem}/\mu_0$ and $\mu_r = \mu_{r1}$. The uniform permanent magnetization is given by

$$\mathbf{M}_p = \mathbf{u}_r M_p \cos\theta - \mathbf{u}_\theta M_p \sin\theta \quad (2.16)$$

where \mathbf{u}_r and \mathbf{u}_θ are the radial and azimuthal unit vectors, respectively. In the non-ferromagnetic region between the permanent magnet and the stator core ($R_1 < r < R_4$), $\mathbf{M}_p = 0$ and $\mu_r = 1$. In the stator core ($R_4 < r < R_5$), $\mathbf{M}_p = 0$ and $\mu_r = \mu_{r5}$.

The magnetic field is modeled by means of the magnetic scalar potential ϕ defined by $\mathbf{H} = -\nabla\phi$. Inserting this definition with (2.15) into the governing equation $\nabla \cdot \mathbf{B} = 0$ yields the Laplace equation $\nabla^2\phi = 0$ for the scalar potential. It is to be noted that $\nabla \cdot \mathbf{M}_p = 0$ for uniform permanent magnetization. In the polar coordinate system, the partial differential equation of the scalar potential is

$$\frac{\partial^2\phi}{\partial r^2} + \frac{1}{r} \frac{\partial\phi}{\partial r} + \frac{1}{r^2} \frac{\partial^2\phi}{\partial\theta^2} = 0. \quad (2.17)$$

In addition to the partial differential equation, interface and boundary conditions are needed. The continuity of the tangential component of the magnetic field strength requires that ϕ is continuous over the interfaces at R_1 and R_4 . The continuity of the normal component of the magnetic flux density requires that $M_p \cos\phi - \mu_r d\phi/dr$ is continuous over the interfaces at R_1 and R_4 . The normal component of the magnetic flux density vanishes at the outer boundary of the machine, which gives the boundary condition $-\mu_r d\phi/dr = 0$ at R_5 .

Magnetic Field Solution

Expressions for the magnetic field are obtained in the whole machine by solving the problem consisting of the partial differential equation (2.17) and the interface and boundary conditions. The solution can be obtained by separation of variables. In the permanent magnet ($0 \leq r \leq R_1$), the radial and azimuthal components of the magnetic flux density are

$$B_r = K_{B1} \cos\theta; B_\theta = -K_{B1} \sin\theta \quad (2.18)$$

respectively, where the flux density coefficient is

$$K_{B1} = \frac{B_{\text{rem}}}{N} \left[\left(1 - \frac{R_4^2}{R_5^2}\right) \left(1 + \frac{R_1^2}{R_4^2}\right) + \frac{1}{\mu_{r3}} \left(1 + \frac{R_4^2}{R_5^2}\right) \left(1 - \frac{R_1^2}{R_4^2}\right) \right] \quad (2.19)$$

with the definition

$$N = \left[1 - \left(\frac{R_4}{R_5}\right)^2\right] \left[(\mu_{r1} + 1) - (\mu_{r1} - 1) \left(\frac{R_1}{R_4}\right)^2 \right] + \frac{1}{\mu_{r5}} \left[1 + \left(\frac{R_4}{R_5}\right)^2\right] \left[(\mu_{r1} + 1) - (\mu_{r1} - 1) \left(\frac{R_1}{R_4}\right)^2 \right]. \quad (2.20)$$

In the non-ferromagnetic region ($R_1 < r < R_4$), the radial and azimuthal components of the magnetic flux density are

$$B_r = K_{B2} \left[1 + \left(\frac{R_4}{r}\right)^2\right] \cos\theta; \\ B_\theta = -K_{B2} \left[1 - \left(\frac{R_4}{r}\right)^2\right] \sin\theta \quad (2.21)$$

respectively, where the flux density coefficient is

$$K_{B2} = \frac{B_{\text{rem}}}{N} \left\{ \left[\left(1 - \frac{R_4}{R_5}\right)^2 \right] - \frac{1}{\mu_{r5}} \left[1 + \left(\frac{R_4}{R_5}\right)^2 \right] \right\} \left(\frac{R_1}{R_2}\right)^2. \quad (2.22)$$

In the stator core ($R_4 < r < R_5$), the components of the magnetic flux density are

$$B_r = K_{B3} \left[-1 + \left(\frac{R_5}{r}\right)^2 \right] \cos\theta;$$

$$B_\theta = -K_{B3} \left[1 + \left(\frac{R_5}{r} \right)^2 \right] \sin\theta \quad (2.23)$$

respectively, where the flux density coefficient is

$$K_{B3} = \frac{2B_{\text{rem}}}{N} \left(\frac{R_1}{R_5} \right)^2. \quad (2.24)$$

Evaluation

The analytical model (2.18)-(2.24) is based on solving only the magnetic field produced by the permanent magnet in a coordinate system fixed to the rotor. The magnetic field contribution caused by the stator current can be added to the model in a fashion similar to [43]. Furthermore, the variation of this field contribution induces eddy currents in the conducting rotor sleeve, which can also be included in the model [44], [45]. However, the magnetic field of a permanent-magnet machine with an air-gap winding is mainly produced by the permanent magnet, and the influence of the stator winding is very small [36]. Hence the efficiency optimization can be carried out without modeling the magnetic field contribution caused by the stator current.

Figure 2.6 shows a comparison between the flux densities obtained using the analytical model (2.18)-(2.24) and a FE method, respectively. The results agree well with each other. It is typical of ultra-high-speed PM machines with a slotless design that the magnetic flux density does not reach values causing magnetic saturation in the iron core. If magnetic saturation occurs, FE analysis can be used in the optimization.

Torque Calculation

The density of the azimuthal force component caused by the spatial fundamental wave J_1 of the current density in the stator winding is $J_1 B_r$. The electromagnetic torque is obtained as the integral

$$T_e = L \int_{-\pi}^{\pi} \int_{R_3}^{R_4} r^2 J_1 B_r dr d\theta. \quad (2.25)$$

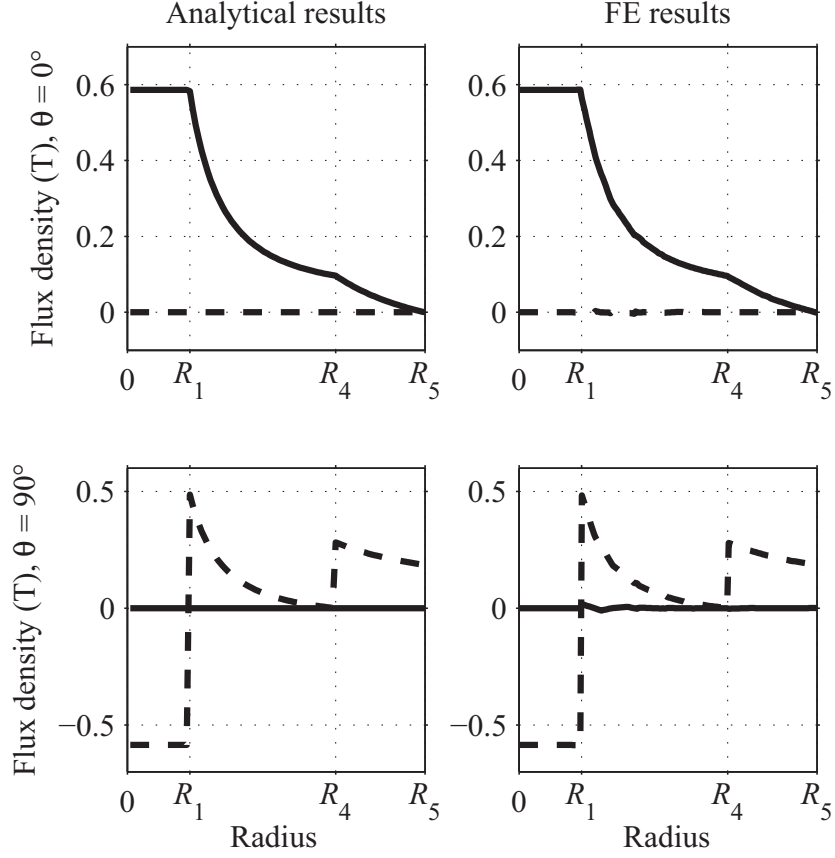


Figure 2.6: Comparison between analytical and FE solutions. Radial flux density components are plotted as solid lines, azimuthal components as dashed lines. $B_{rem} = 1.1$ T, $\mu_{r1} = 1.05$, $\mu_{r5} = 1000$, $R_5 = 8$ mm, $R_4 = 5.6$ mm, and $R_1 = 1.68$ mm.

The stator current component in the direction of the permanent-magnet flux is controlled to zero. Using (2.21), the integration in (2.25) results in

$$T_e = \sqrt{2}\pi k_w k_{Cu} J K_{B2} L R_4^3 \left(\frac{4}{3} - \frac{R_3}{R_4} - \frac{1}{3} \frac{R_3^3}{R_4^3} \right) \quad (2.26)$$

where k_w is the fundamental-wave winding factor, k_{Cu} is the winding fill factor and J the rms current density in the conductors. The current density J can be solved from (2.26) if the electromagnetic torque is known for an operating point. According to [33] the winding factor for the distributed three-phase air-gap winding shown in Figure 2.1 is

$$k_w = \frac{6}{\pi} \sin \frac{\pi}{6}. \quad (2.27)$$

2.3.3 Loss Models

In designing an ultra-high-speed machine, it is important to optimize the efficiency - i.e. minimize the losses. In traditional machine designs, only resistive losses in the stator winding and iron losses in the stator core [46] and, in addition, eddy current losses in the rotor [32] have been considered. However, air friction losses are an important part of the total losses in an ultra-high-speed machine [47]. Furthermore, in this machine type with a slotless design of the stator, the air-gap flux penetrates the winding and causes considerable eddy-current losses. Therefore, these losses should also be taken into account in the design procedure. In the following, models for the loss components are presented.

Copper Losses

The frequency of the fundamental waveform of the stator current is high (e.g. 8.3 kHz in the 500 000 rpm machine). Therefore, eddy currents increase the copper losses of the stator winding. In addition to the stator current, the air-gap flux causes considerable eddy-current losses in the winding due to the slotless design of the stator. In order to reduce the losses, the winding is made of litz wire. The copper losses consist of the current dependent resistive losses $P_{Cu,s}$ in the stator winding, which include the influence of the skin effect, and of the proximity effect losses $P_{Cu,p}$, which are mainly due to the eddy currents induced by the magnetic field of the permanent magnet. The copper losses are

$$P_{Cu} = P_{Cu,s} + P_{Cu,p} = I^2 F + G \frac{\hat{H}^2}{\sigma_{Cu}} \quad (2.28)$$

where I is the rms stator current, \hat{H} is the peak magnetic field strength in the winding, and σ_{Cu} is the conductivity of the conductors. The coefficients F and G include the effects of the eddy currents, and are calculated based on the frequency, the conductivity, and the geometry of the winding arrangement. There are various commonly used methods for

calculating the coefficients in (2.28). The Ferreira method [44] was chosen for the analysis. At significantly higher frequencies or larger strand diameters, i.e. when the field of neighboring strands becomes significant, the accuracy could be increased by using a method based on function fitting for the calculation of the proximity effect losses [45]. However, for this case where proximity losses are dominated by the permanent-magnet field, all methods converge to the same value for the coefficient G .

Iron Losses

There are several methods to calculate the iron losses of magnetic materials. In machines they are usually based on the hysteresis model and/or the eddy-current model, e.g. [48]. However, for the stator core of the machine under investigation both silicon iron laminations, usually used in lower-speed machines, and high-frequency magnetic materials, usually used for inductors and transformers, are considered. Especially for the high-frequency materials, such as ferrites, soft-magnetic powders and amorphous or nanocrystalline iron-based alloys, the Steinmetz equation [49] is the most commonly used method. Furthermore, the iron flux distribution and waveform is sinusoidal, such that the original Steinmetz equation can be used without correction factors. With the flux density in (2.23), the iron losses are calculated as an integral over the iron volume with

$$P_{Fe} = \int_{V_{Fe}} C_m f^\alpha \hat{B}^\beta dV \quad (2.29)$$

where f is the frequency and \hat{B} the peak magnetic flux density. The coefficients C_m , α and β can be directly extracted or obtained by curve fitting from manufacturer's data. The parameters for the materials used in this Thesis are provided in Table 2.3.

Air Friction Losses

For simple geometries, such as cylinders and disks, air friction losses can be calculated analytically with friction coefficients based on empirical data [50]. In the following, only the air gap is taken into account in the calculation of the air friction losses, and the losses at the end caps are omitted. According to [50], the air friction losses of a long rotating

cylinder encased in a stationary hollow cylinder are

$$P_{f,air} = c_f \pi \rho_{air} \omega^3 R_2^4 L \quad (2.30)$$

where ρ_{air} is the density of the air, ω the angular speed, R_2 the radius of the cylinder, and L the length of the cylinder. The friction coefficient depends on the radius of the cylinder, the air gap δ , and the Reynolds number and the Taylor number, which are defined as

$$Re = \frac{R_2^2 \omega}{\nu_{air}}; Ta = \frac{R_2^2 \omega \delta}{\nu_{air}} \sqrt{\frac{\delta}{R_2}} \quad (2.31)$$

where ν_{air} is the kinematic viscosity of air. The flow stability depends on the Taylor number; the flow can be divided into laminar Couette flow ($Ta < 41.3$), laminar flow with Taylor vortices ($41.3 < Ta < 400$), and turbulent flow ($Ta > 400$). For laminar Couette flow, the friction coefficient can be determined analytically, but measurements show discrepancies with the theoretical values. Therefore, empirical data is usually used, and correction factors are applied to adapt for different geometries [50]. For the air gap of the machines under investigation, the friction coefficient

$$c_f = \frac{1.8}{Re} \left(\frac{\delta}{R_2} \right)^{-0.25} \frac{R_3^2}{R_3^2 - R_2^2} \quad (2.32)$$

can be used. Beyond the transition point from laminar flow to flow with Taylor vortices, measurements show a friction coefficient

$$c_f \propto Ta^{-0.2}. \quad (2.33)$$

This model for air friction losses was experimentally validated in [50]. As an example, the calculated air friction losses for the 500 krpm system (see section 5.1.2) are presented. The parameters of the machine are summarized in Table 5.1 and the parameters for air are given in Table 2.3. Figure 2.7 shows the values of the friction coefficients versus Reynolds number used for estimating the friction losses with 2.30. Figure 2.8 shows the calculated air friction losses versus speed. It can be seen that above a speed of 88 000 rpm the air flow in the air gap is fully turbulent. At the rated speed of 500 000 rpm the air friction losses reach 7.8 W and are therefore a main contributor to the total losses at high speeds.

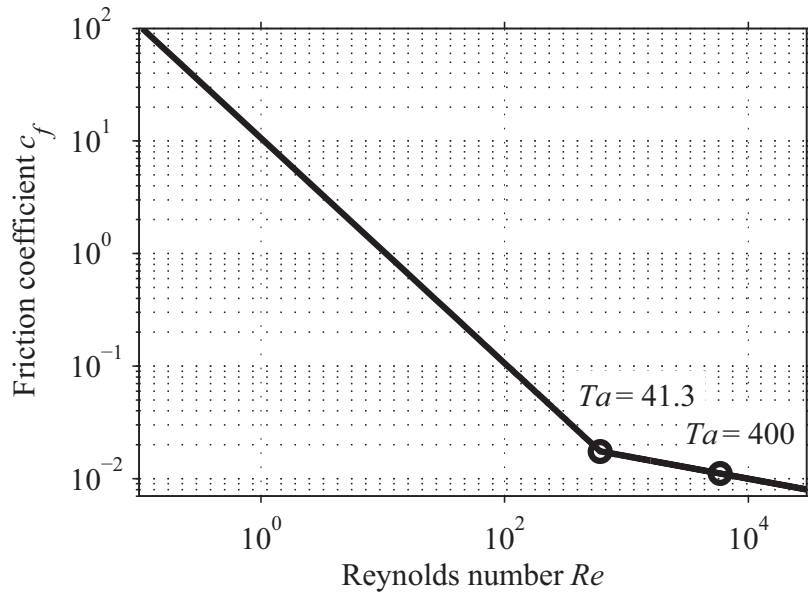


Figure 2.7: Friction coefficient versus Reynolds number for the 500 krpm machine. The transition points from laminar to turbulent flow are indicated with circles.

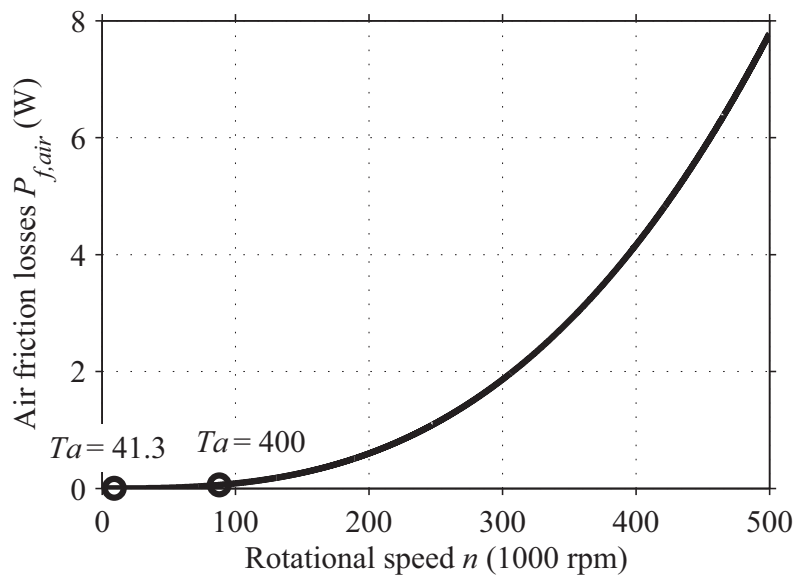


Figure 2.8: Air friction losses versus rotational speed of the 500 krpm machine. The transition points from laminar to turbulent flow are indicated with circles.

Other Losses

The eddy-current losses in the rotor of a slotless PM machine are generally very low as shown in [32]. Therefore, the rotor losses are ignored in

the design and the optimization.

Furthermore, it is to be noted that the bearing losses are not considered in the efficiency optimization of the machine since they are usually more dependent on the application than on the inner dimensions of the motor. A comparison of different bearing concepts is given in Section 4.1.

Shaft Torque

The torque available for an application is not the electromagnetic torque in (2.26), but the mechanical shaft torque T_m . For motor operation, a given mechanical torque required by the application, and when proximity effect losses, iron losses, and air friction losses are taken into account, the electromagnetic torque can be calculated by

$$T_e = T_m + \frac{P_{Cu,p} + P_{Fe} + P_{f,air}}{\omega}. \quad (2.34)$$

2.4 Optimization

Based on the analytical field model, the loss models and different constraints, such as from the mechanical rotor construction, given dimensions, rotor dynamics, etc., an optimization of the machine can be undertaken. Objective functions of such an optimization can be volume, weight, losses, etc.

2.4.1 Loss Minimization

As shown in section 2.2, the volume of an machine decreases with increasing speed for a given power rating, i.e. for a constant efficiency the losses per area increase for increasing rotational speeds. Therefore, for ultra-high-speed machines, it is important to optimize the efficiency - i.e. minimize the losses - when the outer dimensions of the machine are design constraints. In this case, the total losses can be obtained from (2.28)-(2.30), i.e. the objective function is

$$P_d = P_{Cu} + P_{Fe} + P_{f,air}. \quad (2.35)$$

The losses are minimized for a given rotational speed n and shaft torque T_m . The outer radius R_5 and length L of the stator core are kept constant (or changed in an outer iteration), and the independent variables are the magnet radius R_1 , the air gap δ , and the inner radius of the stator core R_4 .

The loss minimization is constrained in order to obtain a geometrically, mechanically, and magnetically feasible design. The sleeve thickness $R_2 - R_1$ is kept at the minimum value given by the mechanical analysis. The minimum value for the air gap δ is 0.2 mm, and the minimum value for the thickness of the stator core ($R_5 - R_4$) is 1 mm, both due to manufacturing and tolerance constraints. In addition, the flux density in the iron core is limited to a maximum value (1.3 T for a silicon iron stack and 1.1 T for an amorphous iron stack), which is a small safety margin to the respective magnetic saturation. A constant temperature of 120°C is assumed for the stator winding, and a constant temperature of 25°C is assumed for the air gap.

Many different methods can be used for solving the minimization problem. A straightforward choice is the Nelder-Mead simplex method included in the MATLAB software as the function `fminsearch`. The constraints can be included in this derivative-free minimization method by giving the objective function a high value if the design is not feasible.

2.4.2 Litz Wire Optimization

The strand diameter of the litz wire only influences the copper losses. During the loss minimization, the strand diameter giving the lowest copper losses is selected for every feasible design. Making the strands thinner decreases the eddy currents, but increases the resistive losses if the winding fill factor decreases. The winding fill factor is given by

$$k_{Cu} = k_{Cu,t}k_{Cu,s}. \quad (2.36)$$

Here, the turn fill factor $k_{Cu,t}$ is defined as the ratio of the area occupied by the litz wires to the total cross-sectional area of the winding. The strand packing factor $k_{Cu,s}$ is the ratio of the copper area of the strands in the wire to the area of the wire. The turn fill factor is assumed to be constant, whereas the strand packing factor is a function of the strand diameter. Figure 2.9 shows the strand packing factors $k_{Cu,s}$ for

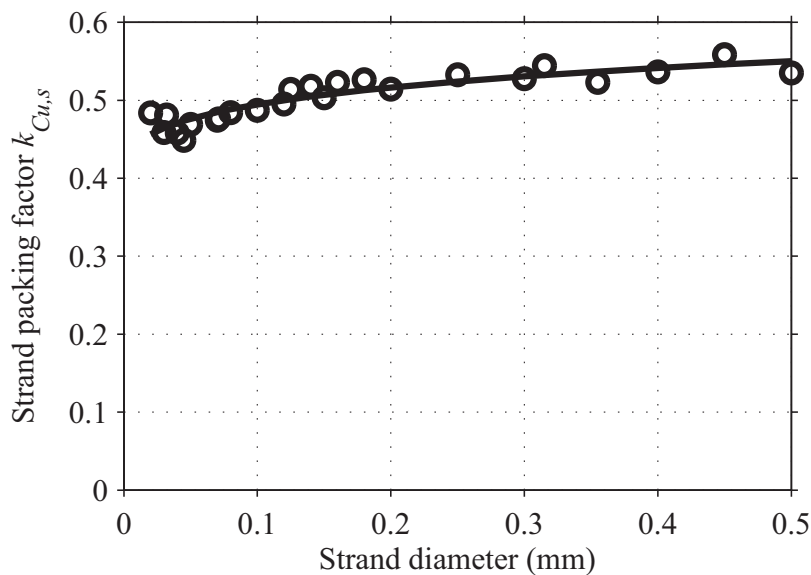


Figure 2.9: Strand packing factor $k_{Cu,s}$ as function of strand diameter: manufacturer’s data (markers) and fitted curve (line).

various strand diameters obtained from manufacturer’s data [51].

2.4.3 Results

Fixed Outer Dimensions

The parameters used in the efficiency optimization are given in Table 2.3. Figure 2.10 and Figure 2.11 illustrate the dependence of the losses on the internal radial dimensions of the machine. The outer dimensions were fixed ($R_5 = 8$ mm and $L = 15$ mm), and the stator core material was laminated silicon iron. The sleeve thickness was fixed to 0.5 mm, and so was the air gap (0.5 mm) and the strand diameter of the litz wire (0.071 mm). In Figure 2.10, the total losses are plotted as a function of the magnet radius R_1 for various values of the inner radius R_4 of the stator core. The individual loss components are shown in Figure 2.11 for the original value $R_4 = 5.5$ mm. It can be seen that the total losses depend strongly on the radius of the permanent magnet, whereas the sensitivity to the inner diameter of the core is low if the radius of the permanent magnet is appropriately chosen.

The minimum of the losses is about 9 W, and it is obtained at $R_4 =$

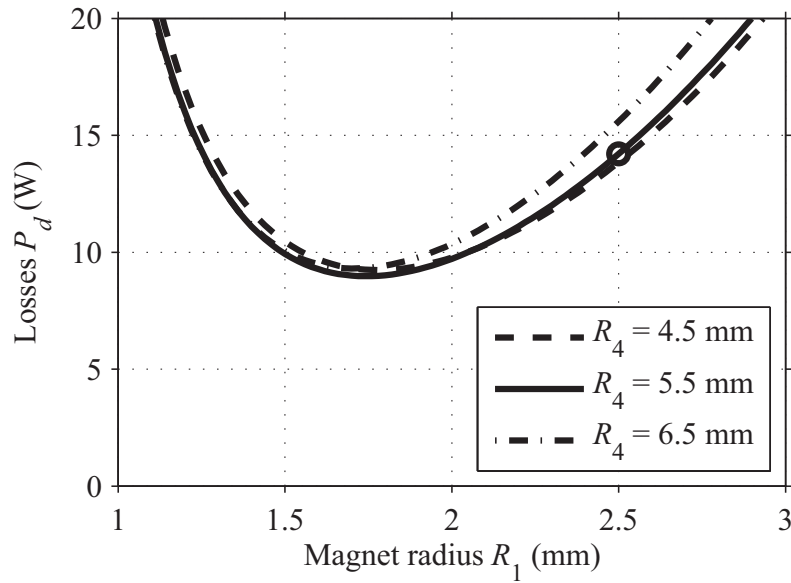


Figure 2.10: Losses of the machine with fixed outer dimensions of the stator core ($R_5 = 8$ mm, $L = 15$ mm) and a shaft power of 100 W at a rotational speed of 500 000 rpm for variable magnet radius R_1 and various values of the inner radius R_4 of the stator core. The circle shows the value for the traditional machine with $R_4 = 5.5$ mm and $R_1 = 2.5$ mm.

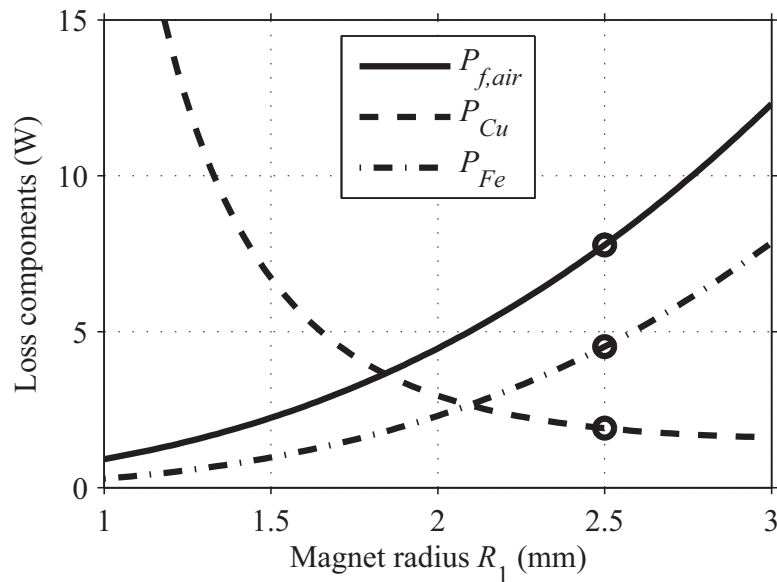


Figure 2.11: Loss components of the machine as described in Figure 2.10 but constant inner radius of the stator core, $R_4 = 5.5$ mm.

Symbol	Quantity	Value
Permanent magnet		
B_{rem}	Remanence flux density	1.1 T
μ_{r1}	Relative recoil permeability	1.05
Silicon-iron laminations		
μ_{r5}	Relative permeability	1860
C_m	Steinmetz coefficient	21.8 W/m ³
α	Steinmetz coefficient	1.42
β	Steinmetz coefficient	1.50
Amorphous iron (Metglas 2605SA1)		
μ_{r5}	Relative permeability	35100
C_m	Steinmetz coefficient	0.94 W/m ³
α	Steinmetz coefficient	1.53
β	Steinmetz coefficient	1.72
Air		
ρ_{air}	Density	1.29 kg/m ³
ν_{air}	Kinematic viscosity	0.000014 m ² /s
Temperatures		
T_{Cu}	Copper temperature	120°C
T_{air}	Air gap temperature	25°C

Table 2.3: Parameters for the optimization.

5.3 mm and $R_1 = 1.7$ mm. A traditional machine design based on copper losses and iron losses only results in the values $R_4 = 5.5$ mm and $R_1 = 2.5$ mm, and it has 14.2 W of losses. Thus a reduction of losses by 5.2 W can be obtained by an optimization including air friction losses and only changing the internal radial dimensions of the machine. It can be seen that the copper losses of the optimized machine are higher than those of the traditional machine, but the air friction and iron losses are reduced. A smaller magnet radius leads to a lower air-gap flux density and thus increases the copper losses. However, a larger amount of air friction and iron losses can be avoided by decreasing the magnet radius. The losses of the traditional machine are shown by circular markers in Figure 2.10 and Figure 2.11.

Variable Outer Dimensions and Strand Diameter

For an improved loss minimization, the sleeve thickness was reduced to the minimum value given by the mechanical analysis ($R_2 - R_1 = 0.25$ mm), and the optimization was based on the three independent variables (R_1 , δ , and R_4). In addition, the strand diameter giving lowest copper losses was determined for the litz wire. In all the following examples, the loss minimization resulted in an air gap value of $\delta = 0.2$ mm, i.e. the minimum value. The optimum strand diameter of the litz wire varied between 0.03 and 0.05 mm, but the influence of small changes in the strand diameter is insignificant since the proximity effect losses are much lower than the other loss components. Figure 2.12 shows the magnet radius R_1 and inner radius R_4 of the stator core for the laminated silicon iron core material. The results are shown for variable outer radius R_5 of the stator core and various values of the core length L . The corresponding total losses are shown in Figure 2.13. For the original outer dimensions ($R_5 = 8$ mm and $L = 15$ mm), the losses can be reduced to about 7 W by choosing $R_4 = 5.1$ mm and $R_1 = 1.8$ mm. Thus the reduction of the air gap and rotor sleeve thickness allows a loss reduction by 2 W from the result shown in Figure 2.10. The losses can be further reduced by increasing the outer dimensions of the machine.

Influence of Stator Core Material

Figure 2.14 and Figure 2.15 show the loss minimization results when the stator core material was laminated amorphous iron (Metglas magnetic alloy 2605SA1). In this case, the iron losses are lower than 10% of the total losses. If the original outer dimensions of the machine are used, a loss reduction to about 5.2 W is possible by choosing $R_4 = 4.5$ mm and $R_1 = 1.9$ mm. The losses of the traditional machine (14.2 W) can thus be reduced by 63% without changing the outer dimensions. It is obvious that for constant L , the results in Figure 2.14 and Figure 2.15 do not depend much on the outer radius R_5 if $R_5 \approx 6$ mm or larger. Thus the outer diameter of the stator can be reduced from the original value with almost no influence on the losses. The losses are higher at the lowest values of R_5 . The loss increase is caused by two constraints used in the optimization: the minimum thickness of the stator core (1 mm) and the maximum flux density allowed in the stator core (1.1 T).

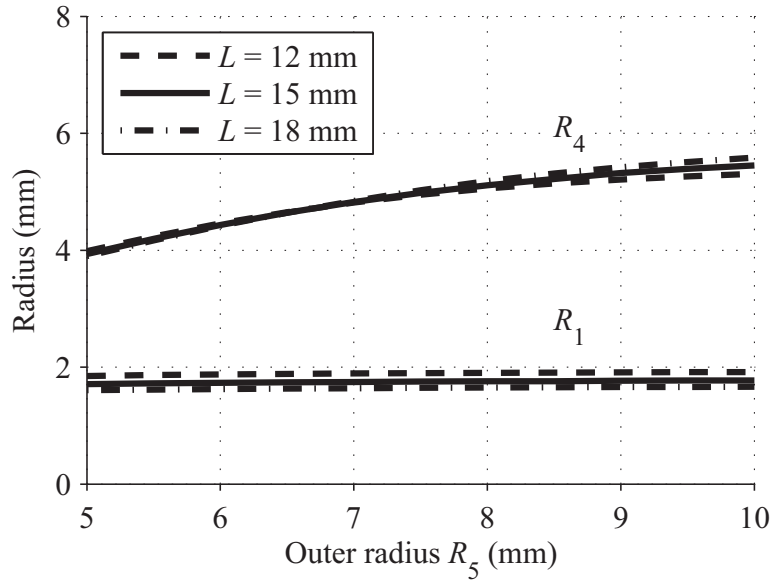


Figure 2.12: Optimization results for the silicon-iron core: magnet radius R_1 and inner radius R_4 of the stator core for variable outer radius R_5 of the stator core and various values of the core length L . The shaft power is 100 W and the rotational speed 500 000 rpm.

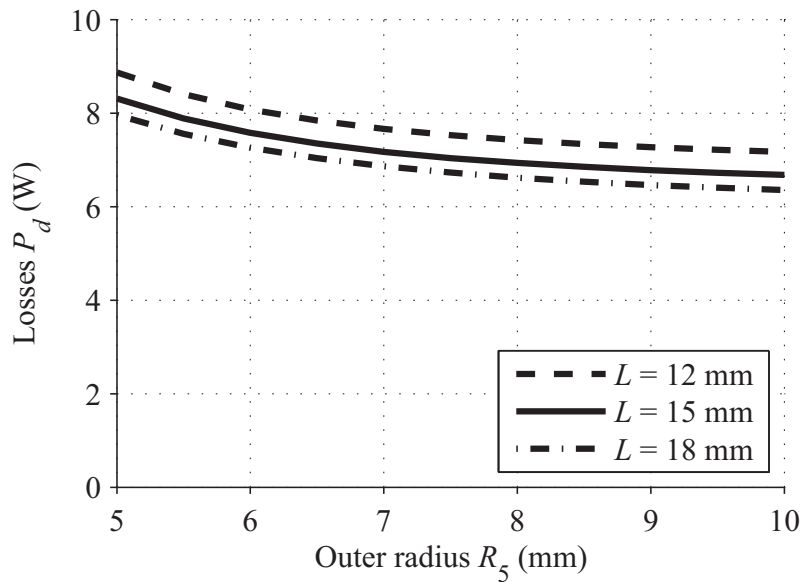


Figure 2.13: Optimization results for the silicon iron core: total losses P_d for variable outer radius R_5 of the stator core and various values of the core length L . The shaft power is 100 W and the rotational speed 500 000 rpm.

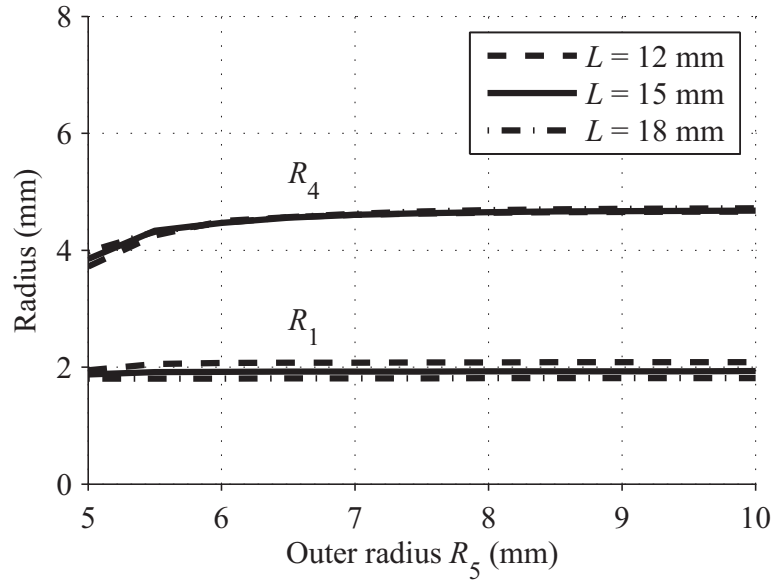


Figure 2.14: Optimization results for the amorphous iron core: magnet radius R_1 and inner radius R_4 of the stator core for variable outer radius R_5 of the stator core and various values of the core length L . The shaft power is 100 W and the rotational speed 500 000 rpm.

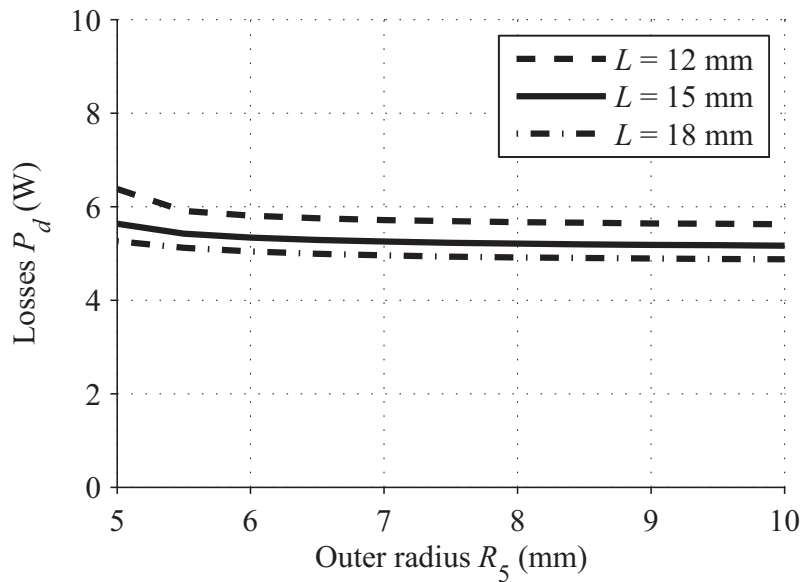


Figure 2.15: Optimization results for the amorphous iron core: total losses P_d for variable outer radius R_5 of the stator core and various values of the core length L . The shaft power is 100 W and the rotational speed 500 000 rpm.

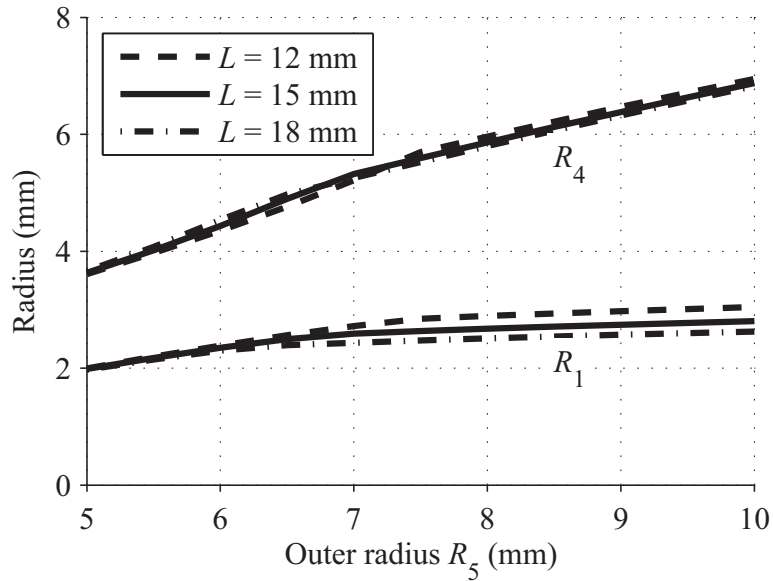


Figure 2.16: Optimization results when air friction losses are omitted. Explanations of curves are as in Figure 2.14.

Influence of Air Friction Losses

The air friction losses (2.30) are approximately proportional to R_5^4 . At high speeds, the inclusion of this loss component in the loss minimization leads to a smaller rotor radius than the one obtained without this loss component. This fact is illustrated in Figure 2.16 and Figure 2.17 showing the loss minimization results when the air friction losses are omitted.

Influence of Speed

In order to investigate the influence of the rotational speed on the results, the losses of 100 W motors were minimized in the speed range between 100 000 and 1 000 000 rpm. The core length was fixed to $L = 15$ mm, and the outer radius R_5 of the core was adjusted in such a way that the flux density was 1.1 T (if possible without contradicting the minimum core thickness constraint). The results are shown in Figure 2.18, Figure 2.19 and Figure 2.20. It is obvious that the inclusion of the air friction losses in the loss minimization leads to very small rotor diameters at the highest speeds. For the power rating considered, the analysis of rotor dynamics would have to be included in the optimization for speeds higher than

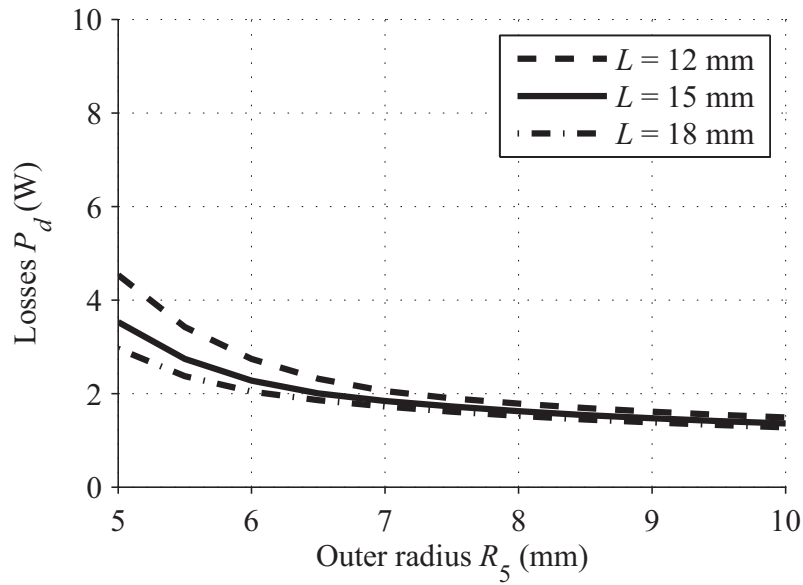


Figure 2.17: Optimization results when air friction losses are omitted. Explanations of curves are as in Figure 2.15.

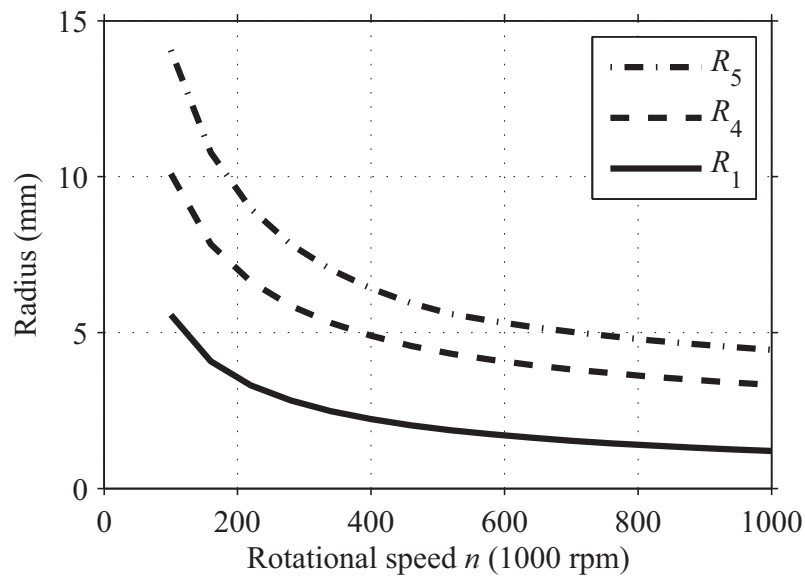


Figure 2.18: Magnet radius R_1 , and inner radius R_4 and outer radius R_5 of the stator core as functions of the rotational speed n used in the optimization. The shaft power is 100 W and the core length $L = 15$ mm.

500 000 rpm, which finally restricts the reduction of the rotor radius with increasing speed.

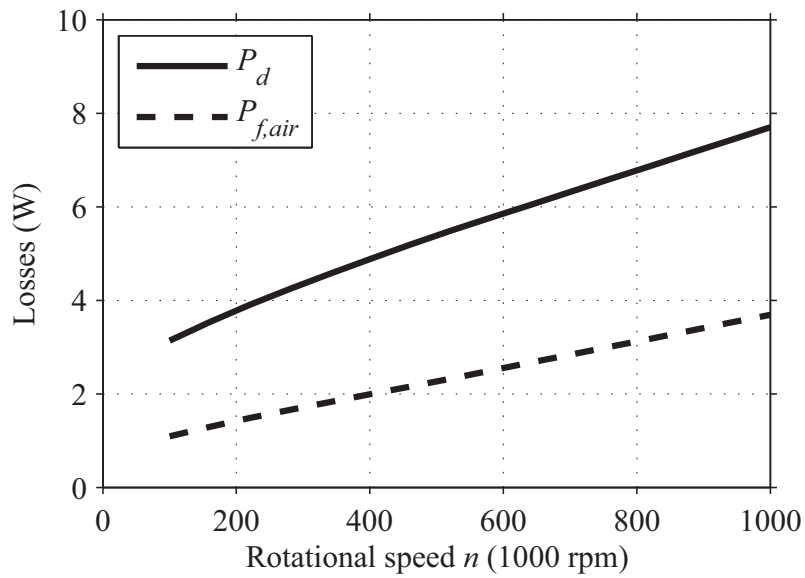


Figure 2.19: Total losses P_d and air friction losses $P_{f,air}$ as functions of the rotational speed n used in the optimization. The shaft power is 100 W and the core length $L = 15$ mm.

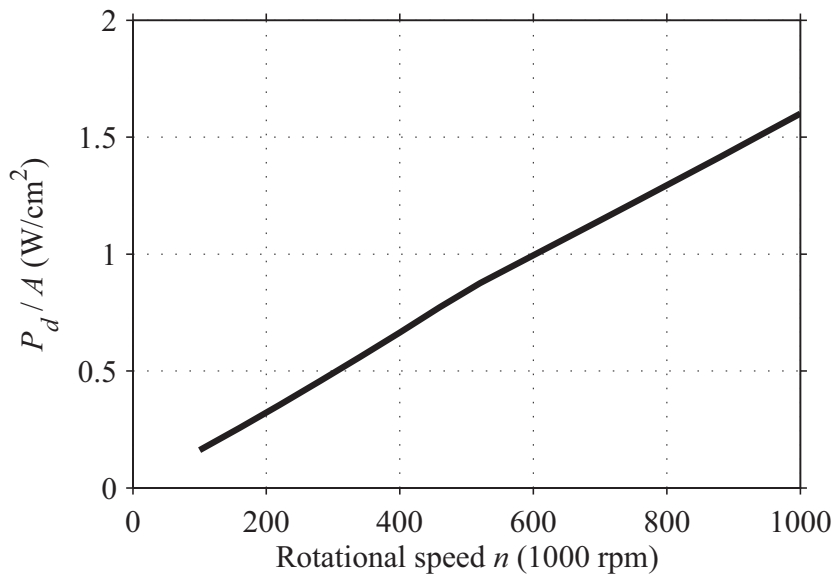


Figure 2.20: Total losses over surface area P_d/A as a function of the rotational speed n used in the optimization. The shaft power is 100 W and the core length $L = 15$ mm.

2.5 Machine Model

Resulting from the torque calculation in (2.26), the current density is translated into litz strand currents by the results from the litz wire optimization. The litz strands can be in connected in parallel or series depending on the current and voltage demand or rating of the power electronics or the application. This winding design leads to a stator phase resistance R_s , a stator phase inductance L_s , and, together with the magnet properties, to the permanent-magnet flux linkage ψ_{PM} used in the following model. These quantities can be determined analytically or by means of FE simulations. For the stator phase resistance, due to the litz wire winding, the skin effect is negligible and only the dc stator resistance has to be determined. This can easily be calculated with the litz strand diameter, the number of parallel strands and the winding length. In contrary to the resistance, the inductance and permanent-magnet flux linkage are determined by means of FE-Simulation. For the machine topology presented in this Thesis, the stator inductance is very low due to the large magnetic air gap. Furthermore, magnetically, the machine has a symmetrical construction (Figure 2.1), the small difference in permeability in the magnet in the magnetization axis and orthogonal thereto is negligible. This results in stator phase inductances independent from the rotor angle. As can be seen in section 2.3.2, the field components in the winding generated by the permanent magnet are sinusoidally distributed along the circumference. This, together with a constant rotational speed ω , results in sinusoidally induced phase voltages (also called back EMF), and such machines are called permanent-magnet synchronous machines (PMSM).

Such a PMSM can be modeled in a stator oriented frame with the three phase quantities for the terminal phase voltages $u_{t,a}$, $u_{t,b}$, $u_{t,c}$ and the phase currents $i_{ph,a}$, $i_{ph,b}$, $i_{ph,c}$. Usually, these three phase quantities are condensed in a space vector for the phase currents \underline{i}_s and a space vector for the terminal voltages \underline{u}_s , where

$$\underline{i}_s = \frac{2}{3} \left(i_{ph,a} + i_{ph,b}e^{2\pi/3} + i_{ph,c}e^{-2\pi/3} \right) \quad (2.37)$$

and

$$\underline{u}_s = \frac{2}{3} \left(u_{t,a} + u_{t,b} e^{2\pi/3} + u_{t,c} e^{-2\pi/3} \right) \quad (2.38)$$

respectively. With the factor $2/3$ it can be achieved that the absolute value of the space vector quantities equals the amplitude of the phase quantities in the symmetric case. With this and the space vector for the permanent-magnet flux linkage

$$\underline{\psi}_{pm} = \psi_{pm} e^{(j\omega t)} \quad (2.39)$$

the electromagnetic part of the machine can be fully described with

$$\underline{u}_s = \underline{i}_s R_s + L_s \frac{\partial \underline{i}_s}{\partial t} + j\omega \underline{\psi}_{pm}. \quad (2.40)$$

The virtual back EMF in phase a can be determined with $\Re(j\omega \underline{\psi}_{PM})$. This three-phase, stator oriented model closely represents the mechanical stator construction with the three-phase winding. These space vectors are in a stator fixed coordinate system, however, for control purposes the quantities are preferably represented in a coordinate system fixed to the rotor. This can be achieved with rotating the stator fixed space vectors with

$$\underline{i}_s = \underline{i}_s e^{j\omega t} \quad (2.41)$$

$$\underline{u}_s = \underline{u}_s e^{j\omega t} \quad (2.42)$$

which leads to the space vectors for stator voltage \underline{u}_s and stator current \underline{i}_s fixed to the rotor axis. For stationary operation, these space vector quantities can then be represented in phasor diagrams, e.g. Figure 3.8, with real axis (d-axis) in direction of the rotor flux linkage and a imaginary axis (q-axis) orthogonal to the direction of the rotor flux linkage. The d-axis has an angle $\epsilon = \omega t$ to the axis of phase a in the stator coordinate system. This leads to the well-known PMSM model in the reference frame fixed to the rotor, with currents and voltages split up into d - and q -components. For this machine with $L_d = L_q$ the PMSM can be represented with (2.43) - (2.46).

$$u_d = R_s i_d + L_s \frac{\partial i_d}{\partial t} - \omega L_s i_q \quad (2.43)$$

$$u_q = R_s i_q + L_s \frac{\partial i_q}{\partial t} + \omega L_s i_d + \omega \psi_{pm} \quad (2.44)$$

$$T_e = \frac{3}{2} i_q \psi_{pm} \quad (2.45)$$

$$J \frac{\partial \omega}{\partial t} = T_e - T_b \quad (2.46)$$

The translation of stator three phase-components to the rotor reference frame is done with the Park-transformation

$$\begin{pmatrix} x_d \\ x_q \end{pmatrix} = \begin{pmatrix} \cos \epsilon & \cos(\epsilon - 2\pi/3) & \cos(\epsilon + 2\pi/3) \\ -\sin \epsilon & -\sin(\epsilon - 2\pi/3) & -\sin(\epsilon + 2\pi/3) \end{pmatrix} \begin{pmatrix} x_a \\ x_b \\ x_c \end{pmatrix}. \quad (2.47)$$

2.5.1 Machine Data and Specifications

The usual machine data provided for this type of machine includes the stator inductance L_s , the stator resistance R_s , and the permanent-magnet flux linkage ψ_{pm} . Furthermore, mechanical data such as dimensions and inertia J might be provided. Specifications can include rated and maximum voltages, currents, speeds and power levels. For the two machines presented in this Thesis the data is compiled in Table 5.1.

Chapter 3

Power and Control Electronics

3.1 Topology Selection

3.1.1 Requirements

The basic task for the power electronics and the control system is to drive the machine described in chapter 2 with the desired speed. The requirements can be divided into the following items:

- Supply the motor phases with currents with fundamental frequencies beyond 16.7 kHz (which equals a rotational speed of 1 million rpm for a two-pole machine).
- For most of the applications in the low power range, a low voltage dc supply is existing or a dc output is required. Therefore, the power electronics should interface to a constant dc voltage supply. For some applications (e.g. a gas turbine starter/generator) bidirectional operation is required.
- Depending on the application (e.g. for a portable gas turbine system), the power and control electronics have to be very compact.

In contrast to electrical machines, the size of the power electronics mainly scales with power rating and is minimized by choosing the correct topology through efficiency improvements and the use of high switching frequencies. For systems with high power ratings, the size of the control electronics is negligible compared to the power electronics. However, for ultra-high-speed machines with low power ratings (e.g. 100 W), the control electronics size becomes significant. Generally, the size of the control electronics scales with the complexity of the control method selected and the complexity depends on the topology and the modulation schemes used.

- Guarantee a sufficiently low current ripple. Due to the litz wire winding with thin strands optimized for proximity effect losses, the copper losses due to current harmonics are negligible. However, the current harmonics also influence the magnetic field in the machine, called armature reaction, and especially high frequency harmonics can lead to additional eddy current losses in stator core and rotor sleeve. Achieving low high-frequency current harmonics is not trivial as the phase inductance of the machine is very low due to the large air gap. For a standard voltage source inverter (VSI) this then results in a trade-off between higher switching frequency (losses, current control bandwidth) and a bigger filter (volume, weight).
- The rotor position has to be determined without additional sensors up to and beyond 1 million rpm. This not only requires a special sensorless rotor position detection, but it also influences the power electronics topology selection as well as the commutation strategy.
- The control system has to include cascaded current (torque) and speed control loops. Furthermore, the control system also has to provide communication with an external interface setting the speed reference, for example a PC.

3.1.2 Topology Candidates

Typically, only standard VSIs are used for low power, low voltage PM machines. Traditionally, for a PMSM (sinusoidal back EMF), as the one presented in section 2, the stator currents are controlled to follow a sinusoidal waveform. However, also these machines can be fed with square-wave currents, usually used for brushless dc (BLDC) machines with trapezoidal

waveform. Due to the high fundamental frequency and the low inductance of the machine, the standard VSI (PMSM or BLDC operation) is not an automatic choice, because either a very high switching frequency, in the order of a factor of twenty compared to the fundamental frequency, is required, and/or a filter between the inverter and the machine has to be employed [52]. A typical VSI configuration with an LCL-filter is shown in Figure 3.1 a). The most simple filter would be only one inductance per phase, i.e. $C_x = 0$ and $L_{x2} = 0$. Higher switching frequency (for a rotational speed of 1 million rpm and a factor of 20 between fundamental and switching frequency the switching frequency is 335 kHz) leads to proportionally higher switching losses and therefore increased cooling requirements. Furthermore, the current control bandwidth has to be very high, which pushes the limits of current measurement, analog signal electronics, controller and gate driver design, and switching time. Because of these disadvantages, also other topologies are considered, with the focus on topologies that allow to switch the inverter stage with the fundamental frequency of the stator currents, and therefore avoid the problems mentioned above.

The traditional VSI can be extended with a DC/DC converter stage which can control the dc link voltage, and therefore the inverter stage only has to task to commutate this voltage or current to the machine with the fundamental frequency. Therefore, this topology is referenced to as the pulse amplitude modulation (PAM) inverter [53], or the variable dc link inverter [54]. Due to the fact that in the inverter stage the half-bridges switch in 120 electrical degree blocks, a further denomination is VSI with block commutation [55]. The DC/DC converter can be realized for uni- or bidirectional power flow depending on the requirements. The topology is shown in Figure 3.1 b) and will further on be referred to as PAM inverter. In the PAM inverter, when carefully selecting the dc link capacitance C_{dc1} , the machine torque can be controlled with controlling the dc current, because in average, the dc current is proportional to the phase currents. This leads to only one current control loop instead of three as for the standard VSI, and the required bandwidth of this control loop is whether dependent on the inverter switching frequency nor on the fundamental frequency of the stator currents, but on the desired torque control bandwidth. Furthermore, the passives (dc link inductance L_{dc} and C_{dc1}) can be dimensioned in accordance with the desired current and voltage ripples and the DC/DC converter switching frequency.

The same commutation strategy with 120 electrical degree blocks in the inverter stage can be used in a current source inverter (CSI). Also here, the dc current is controlled with an additional DC/DC converter. However, for bi-directional power flow, the DC/DC converter has to invert the voltage instead of the current as in the PAM inverter, which requires a full bridge. Furthermore, the switches in the inverter stage have to be reverse blocking, which can be achieved with a diode in series with the MOSFET. The dc link current is decoupled from the phase currents with a three-phase output filter consisting of three capacitors. The topology is shown in Figure 3.1 c). Also here, as for the PAM inverter, the torque control bandwidth can be set independently and the dc inductor L_{dc} can be dimensioned in accordance with the desired current ripple and the DC/DC converter switching frequency. Only the three topologies VSI, PAM inverter, and CSI are considered further. However, for the sake of completeness two more possibilities for driving ultra-high-speed permanent-magnet machines, the inherently bi-directional current source AC/DC converter [56] and the Z-source converter [57] are presented in Figure 3.2 a) and Figure 3.2 b) respectively. With the bi-directional current source AC/DC converter, no additional dc-dc converter is needed, but there is additional complexity and switches required for each phase leg of the inverter. Furthermore, this converter needs minimal ac voltages and therefore a minimal speed of the machine, therefore it is no option for variable speed machines and motor start-up. The Z-source converter can also offer bidirectional power flow when adding a switch at the input, is capable of boosting the dc input voltage and has inherent protection from a bridge-leg short-through condition. However, also this converter has additional control complexity and higher losses. All the topologies have been compared in [58].

Figure 3.3-Figure 3.6 depict simulation results of the phase current waveforms and the corresponding phase leg switching signals for the three topologies considered. For the VSI, both sinusoidal and square-wave current control is presented. The shape in the current waveform of the PAM inverter is the result of the applied voltage over the machine phase inductances. When neglecting the commutation intervals from one phase to another, the voltage over the inductors is the constant dc-link voltage minus the rectified three-phase, sinusoidal back EMF voltages. The three topologies are further compared in Table 3.1 concerning complexity, number of semiconductors and volume of passive components. For

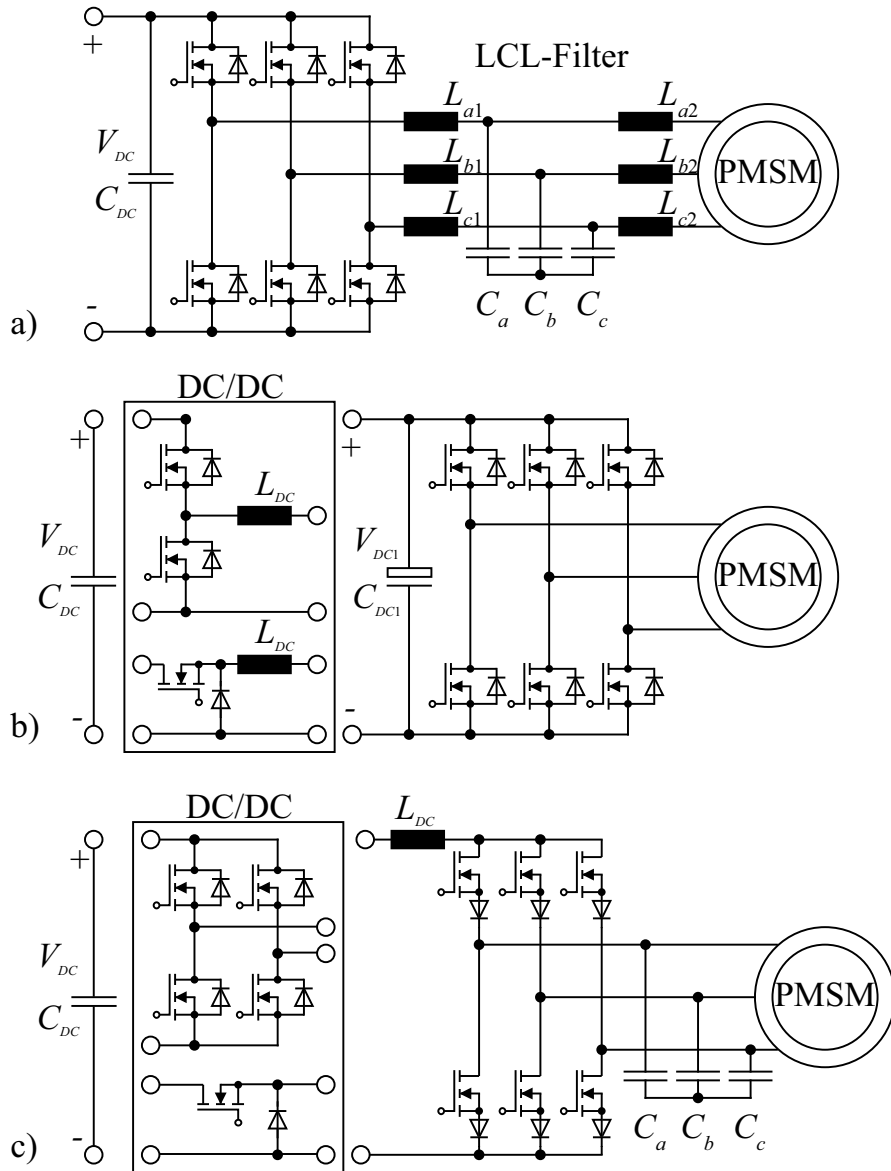


Figure 3.1: Possible power electronic topologies for driving an ultra-high-speed permanent-magnet machine: Traditional VSI with additional output LCL-filter (a), PAM VSI with additional DC/DC converter for uni- or bidirectional power flow (b), and CSI with output capacitors and additional DC/DC converter for uni- or bidirectional power flow (c). The inverter stage of the CSI and PAM VSI switch with the fundamental frequency.

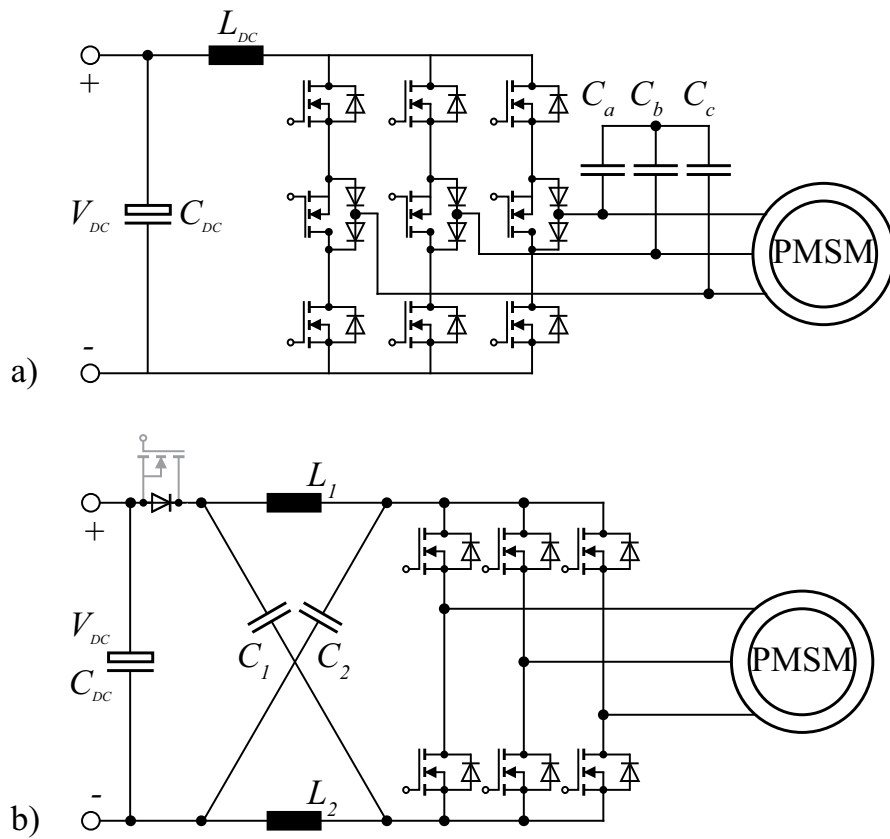


Figure 3.2: Not further considered, alternative topologies for driving an ultra-high-speed permanent-magnet machine: bi-directional current source AC/DC converter (a) and Z-source converter (b).

	VSI	PAM inverter	CSI
Switching frequency	–	+	+
Current control bandwidth	–	+	+
Number of MOSFETs	6	8	10
Number of diodes	0	0	6
Conduction losses	+	0	–
Switching losses	–	+	+
Volume of passive components	+/–	0	–
Control complexity	–	+	+

Table 3.1: Comparison of converter topologies.

the PAM inverter and the CSI the bidirectional topology is chosen. The VSI has the advantage of the lowest number of semiconductor elements and therefore potentially lower conduction losses. This is why the VSI is the preferred choice for most BLDC and PMSM drive systems. The main disadvantage for this application is the high current control-loop bandwidth and the high switching frequency needed, and this for all the three half bridges. This increases the control complexity and leads to high switching losses and therefore a lower efficiency. The problems of high switching frequency and current control bandwidth can be overcome when the inverter is switched at the fundamental frequency of the machine as in the PAM inverter and the CSI. The switching losses and the control complexity for the three phase bridge legs are significantly reduced. However, the disadvantage is that an additional DC/DC converter is required to control the dc current. The current control bandwidth and switching frequency of the DC/DC converter can be selected to reduce switching losses since the dynamic behavior of the drive system is not critical. The main disadvantage is the increased volume caused mainly by the dc inductor. For the PAM inverter, this inductor can be made smaller as for the CSI since additional smoothing is provided with an output capacitor.

3.1.3 PAM Inverter

The standard VSI has the advantage of the lowest number of semiconductors needed. The ac filter is no drawback, as the passives on the dc

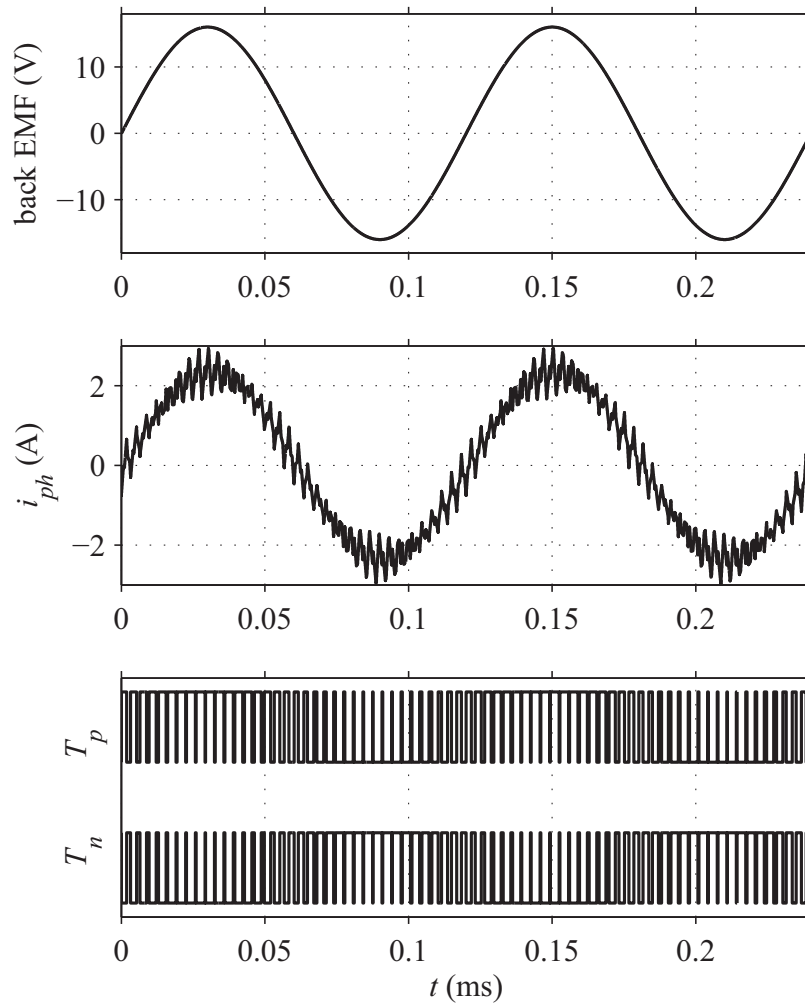


Figure 3.3: Simulation results (machine back EMF, phase current and switching signals for the phase leg) of a PMSM driven with the standard VSI (Figure 3.1 a)) with pulse width modulation (PWM) and sinusoidal current control. In the d-q reference frame fixed to the rotor the d-axis current is controlled to zero and the q-axis current to 2.3 A. The two-pole PMSM has a flux linkage of 0.306 mVs, a stator inductance of $3 \mu\text{H}$, a stator resistance of 0.2Ω and rotates at 500 000 rpm. The inverter has an input voltage of $V_{dc} = 40 \text{ V}$ and a switching frequency of 300 kHz. The filter components are $L_{x1} = 10 \mu\text{H}$, $C_x = 0$ and $L_{x2} = 0$.

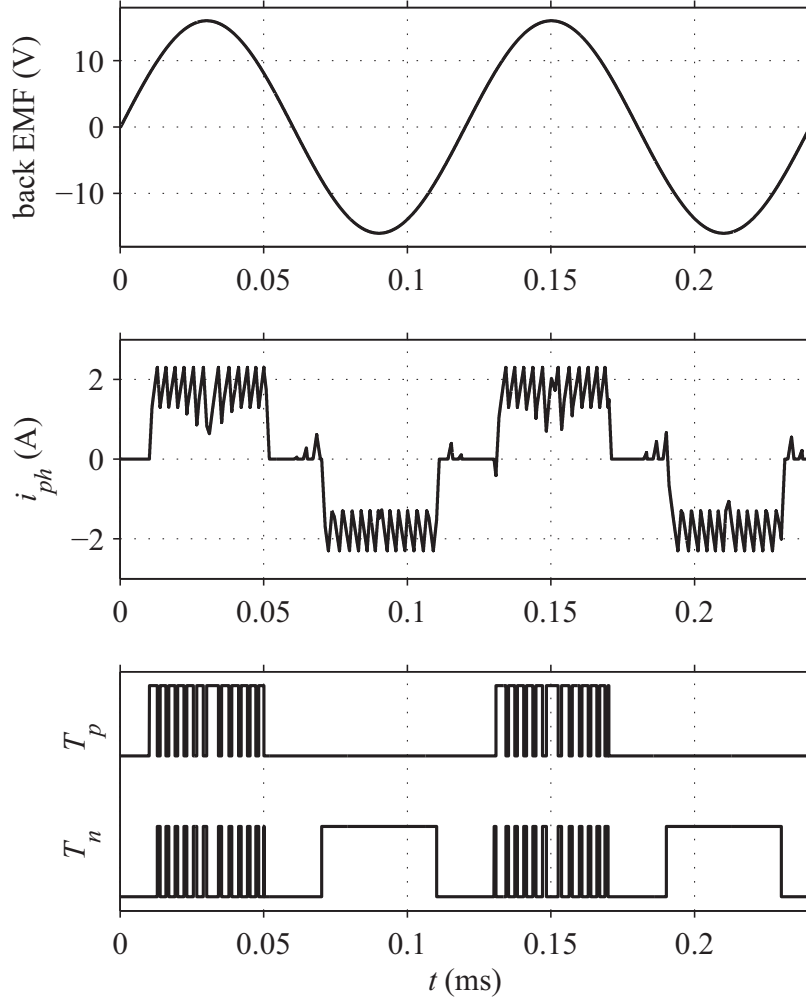


Figure 3.4: Simulation results (machine back EMF, phase current and switching signals for the phase leg) of a PMSM driven with the standard VSI (Figure 3.1 a)) with hysteresis BLDC current control. The currents are controlled to 1.8 A with an allowed ripple current of 1 A during the on interval of one phase. The two-pole PMSM has a flux linkage of 0.306 mVs, a stator inductance of $3 \mu\text{H}$, a stator resistance of 0.2Ω and rotates at 500 000 rpm. The inverter has an input voltage of $V_{dc} = 40 \text{ V}$, and the filter components are $L_{x1} = 10 \mu\text{H}$, $C_x = 0$ and $L_{x2} = 0$. This results in an average switching frequency of 250 kHz.

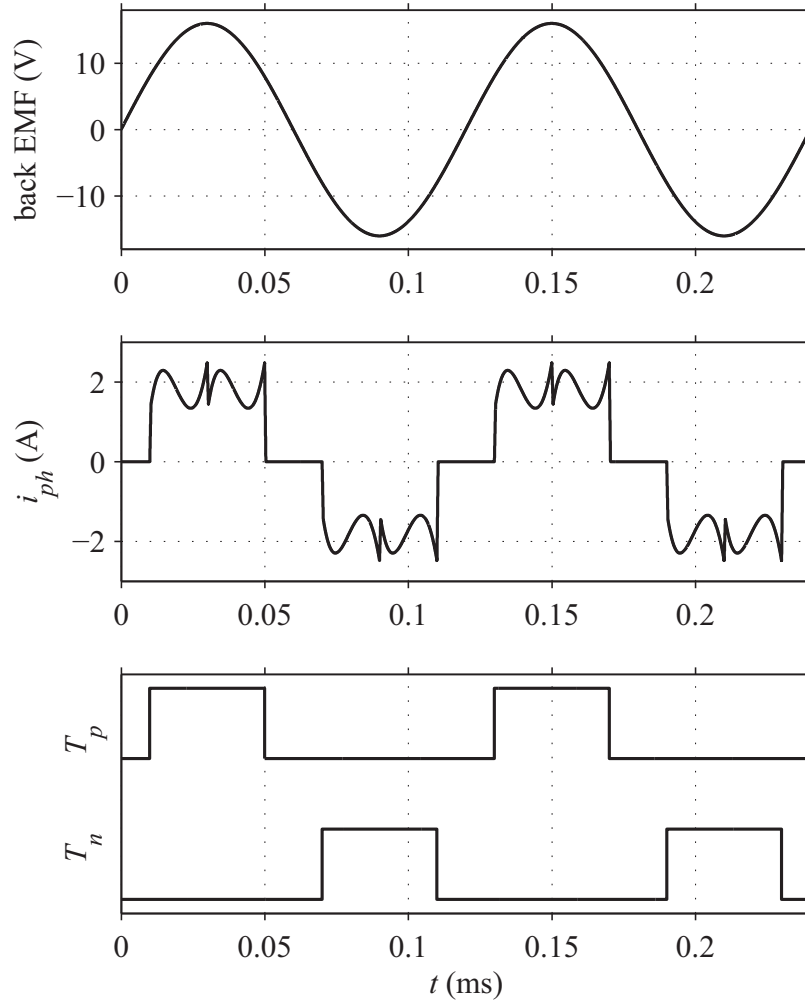


Figure 3.5: Simulation results (machine back EMF, phase current and switching signals for the phase leg) of a PMSM driven with the PAM inverter (Figure 3.1 b)). The dc link current is controlled to 1.8 A. The two-pole PMSM has a flux linkage of 0.306 mVs, a stator inductance of $3 \mu\text{H}$, a stator resistance of 0.2Ω and rotates at 500 000 rpm. The inverter has an input voltage of $V_{dc} = 40 \text{ V}$, the dc link inductance is $L_{DC} = 50 \mu\text{H}$, the dc link capacitance is $C_{DC1} = 40 \mu\text{F}$ and the DC/DC switching frequency is 100 kHz.

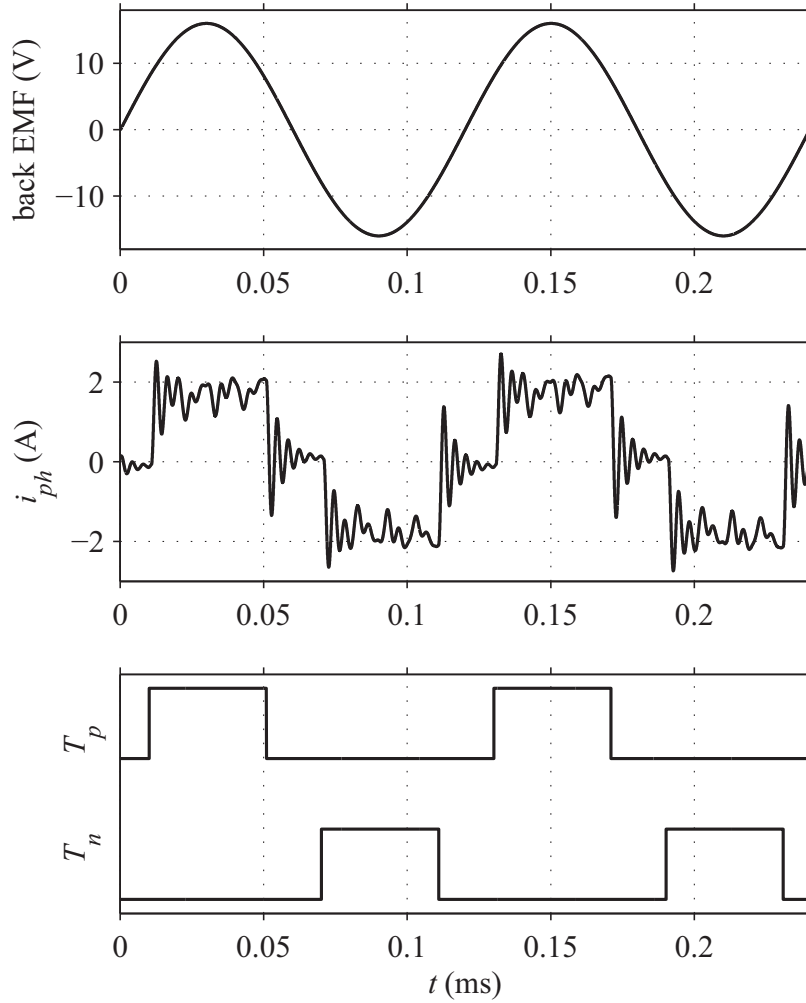


Figure 3.6: Simulation results (machine back EMF, phase current and switching signals for the phase leg) of a PMSM driven with the CSI (Figure 3.1 c)). The dc link current is controlled to 1.8 A. The two-pole PMSM has a flux linkage of 0.306 mVs, a stator inductance of $3 \mu\text{H}$, a stator resistance of 0.2Ω and rotates at 500 000 rpm. The inverter has an input voltage of $V_{dc} = 40 \text{ V}$, the dc link inductance is $L_{DC} = 100 \mu\text{H}$, the output capacitors are $C_x = 147 \text{ nF}$ and the DC/DC switching frequency is 100 kHz.

	switching losses ¹ (W)	conduction losses ² (W)
$T_{DC,p}$	1.15	0.15
$T_{DC,n}$	0.05	0.07
T_{inv}	0.10	0.07
L_{DC}		0.68
Total		3.12

¹switching loss measurements at 25°C, ²calculations at 25°C

Table 3.2: Loss balance for a PAM inverter driving the 500 krpm machine with a speed of 500 000 rpm at a power of 100 W.

link for the other two topologies result in a similar volume. However, due to the drawback of the very high switching frequency and the high bandwidth needed for the current control loop, the VSI is not the optimal choice, as this results in a lower efficiency due to switching losses and an increased effort and volume in the measurement and control system, which, for low power inverters, can be a major part of the total volume.

Compared to the PAM inverter, the CSI has only the advantage of a more direct phase current control, but several drawbacks: A high number of semiconductors needed and therefore higher conduction losses, a higher value and therefore volume of the dc inductor due to the absence of a dc link capacitor, and an increased effort for bidirectional power flow.

Due to the low switching losses, the low complexity control, the bidirectional power flow capability and a relatively low volume of the passives, the PAM inverter is the preferred choice for driving an ultra-high speed, low inductive, PMSM.

In Table 3.2 the loss balance of a PAM inverter for driving the two machines presented in section 5.1 is given. A standard low voltage MOSFET (IRFR3710ZPbF) is chosen and the switching losses have been determined with measurements, the conduction losses have been calculated. The dc link inductance is realized with a iron-powder core and a lizt wire, the losses have been calculated. As in Figure 3.5 the dc link inductance has a value of 50 μ H and the DC/DC switching frequency is 100 kHz. For driving the 500 krpm machine (Table 5.1) with a rotational speed of 500 000 rpm and a power of 100 W the power electronics have total losses of 3.12 W which results in an efficiency of 97.0% for the PAM inverter.

3.2 Sensorless Rotor Position Detection

A sensorless technique is used to control the stator currents, in order to overcome the disadvantages of rotor position sensors, such as an increased failure probability and an axial extension of the machine. Especially in ultra-high-speed machines, a longer rotor is unwanted because the critical speeds are lowered. Traditional sensorless control methods use model based estimation of the back EMF to calculate the rotor angle at any instant. The disadvantages are a large computational effort and the requirement of phase current measurements. For the PAM inverter with 120 electrical degrees current blocks, also known as six-step operation, the back EMF can be directly measured during the off intervals in each phase. The detected zero-crossings can be phase-shifted by 30 electrical degrees and used for switching operations, as described in [59] and shown in Figure 3.7. With this information on the rotor position, the stator current is then usually controlled approximately perpendicular to the permanent-magnet flux, corresponding to maximum torque-per-current operation. Only digital signals are processed, and the computation effort is limited. Nevertheless, unwanted zero-crossings have to be digitally masked, and the 30-degree phase shift has to be implemented. The lower limited speed range due to the speed dependence of the back EMF amplitude and noise sensitivity are further drawbacks. A major drawback is the upper speed limit as described in [59]. It is due to the diode conduction, when the current in one phase decreases to zero, which should be significantly lower than 30 electrical degrees in order to guarantee a zero crossing detection. The diode conduction angle is depending on the machine design and the actual current loading.

Due to these drawbacks, an improved method is suggested which is partly based on sensorless techniques described in [6], where a PMSM is fed by a PWM inverter or a linear amplifier, and in [60], where a BLDC motor is controlled by a VSI.

For the following considerations, only the fundamental waveforms for currents and voltages are considered. Looking at the back EMF and the terminal voltage in Figure 3.7 this is an acceptable approximation. However, considering the phase current waveform, the approximation is only valid if the signals used in the sensorless control are filtered, which is the case as we will see later on. Also the current commutation in between the phases, i.e. the diode conduction angle, is neglected. This is valid for

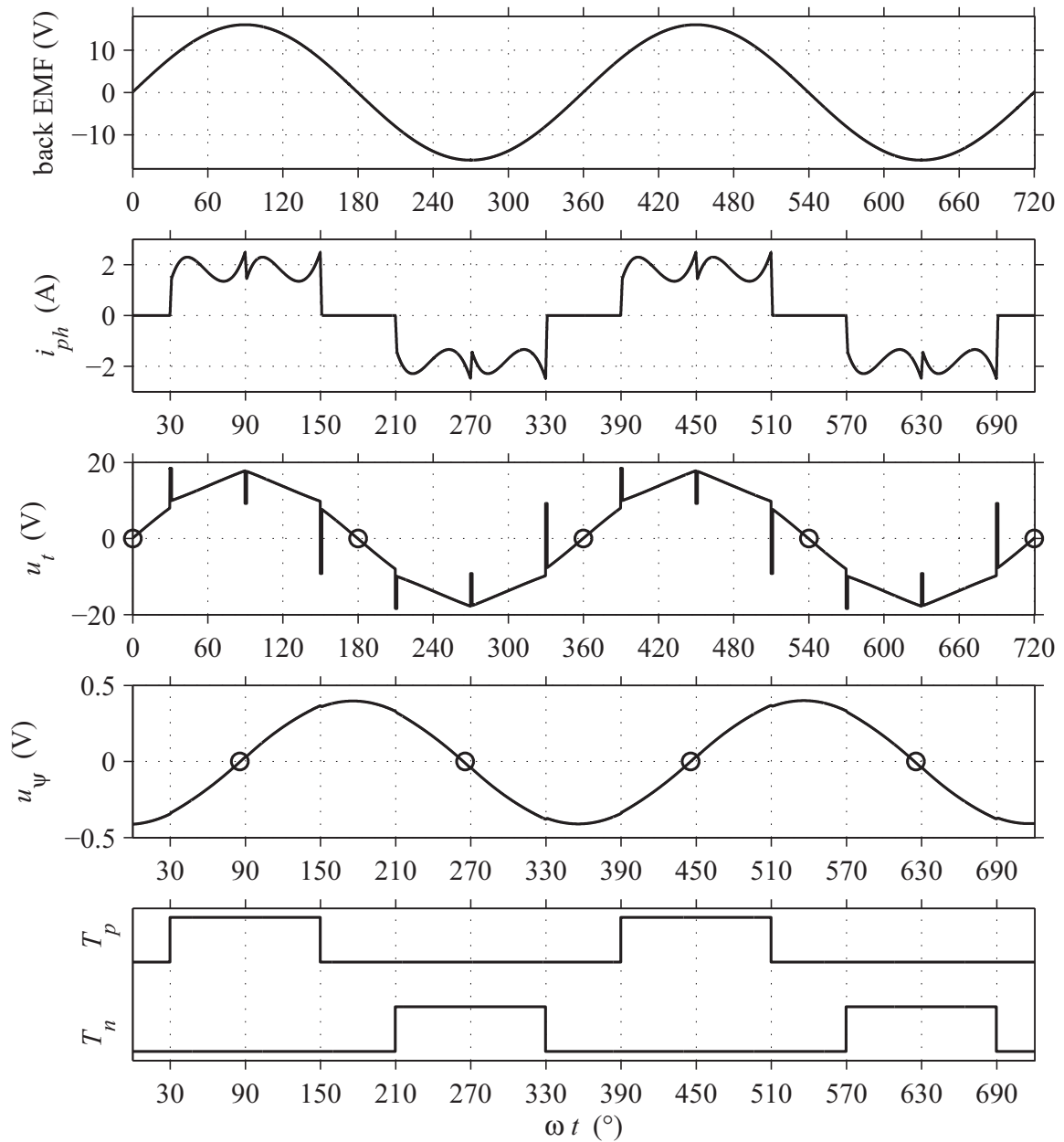


Figure 3.7: Simulation results (machine back EMF, phase current, machine terminal voltages to star point u_t , voltage in phase with the stator flux u_ψ and switching signals for the phase leg) of a PMSM driven with the PAM inverter as described in Figure 3.5. The zero-crossings of the back EMF can be detected in u_t , as indicated with circles, and are phase-shifted by 30 electrical degrees compared to the switching instants. The steady-state difference of the zero-crossings of u_ψ , indicated with circles, to the switching instants is very small, also see (3.1).

low inductive machines with small diode conduction angles.

The voltages presented in simulations and equations are phase quantities. In the practical realization, they are measured in reference to a star point which can be provided with an additional connection to the machine star point or generated externally on the electronics, usually with three equal resistors in star connection.

In the improved sensorless rotor position detection, the fundamental stator current waveform is controlled perpendicular to the stator flux linkage ψ_s instead of the permanent-magnet flux linkage ψ_{pm} as illustrated in Figure 3.8 for steady-state operation. The stator flux position is estimated by integrating the terminal voltages $u_{t,a,b,c}$, leading to signals $u_{\psi,a,b,c}$ in phase with the stator flux (Figure 3.9). The zero-crossings of these signals $s_{a,b,c}$, indicated with circles on u_{ψ} in Figure 3.7, have a steady-state angle difference to the ideal switching instants, indicated with circles on u_t in Figure 3.7. This is due to the voltage drop over the stator inductance and resistance. However, the difference is very small due to the small inductance and therefore the zero-crossings can directly be used for switching the inverter. Then, since the stator currents are now in phase with the stator voltages (and not the back EMF as for maximum torque per current operation), the resistive voltage drop only influences the magnitudes of the signals $u_{\psi,a,b,c}$ but not their phases. A comparison to the maximum torque per current operation can be made by considering the steady-state stator current displacement

$$\delta = \arcsin \left(\frac{L_s \hat{i}_{ph}}{\psi_{pm}} \right) \quad (3.1)$$

of the fundamental waveform with respect to the back EMF induced by the permanent-magnet flux. As an example, for the machine of the simulations with a flux linkage of 0.306 mVs, a stator inductance of 3 μ H and a peak phase current of 4 A this results in a current displacement δ of 2.2 electrical degrees, and this represents a torque decrease of only 0.08% compared to maximum torque per current operation.

The main advantages of this sensorless control are

- The terminal voltages are filtered and noise is reduced due to the integration.
- The signals are phase shifted by -90 electrical degrees and the zero-

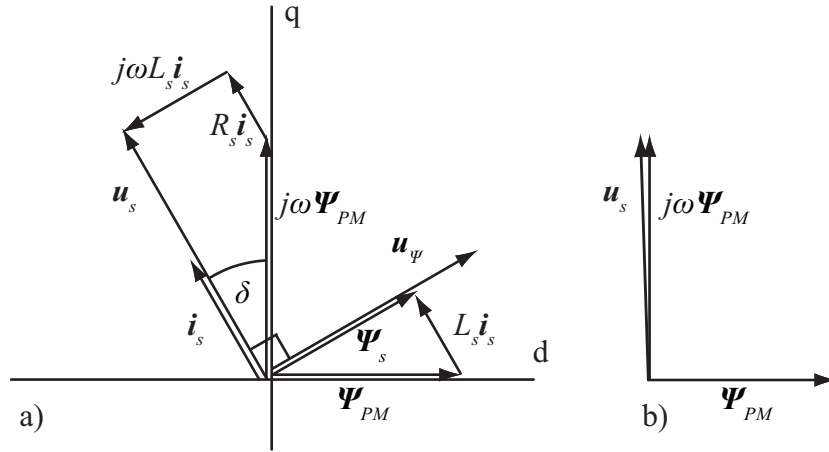


Figure 3.8: Phasor diagram for the applied sensorless control, not drawn to scale (a) and drawn to scale for a machine with a flux linkage of 0.306 mVs, a stator inductance of 3 μ H and a peak phase current of 4 A (b). The stator current is controlled perpendicular to the stator flux.

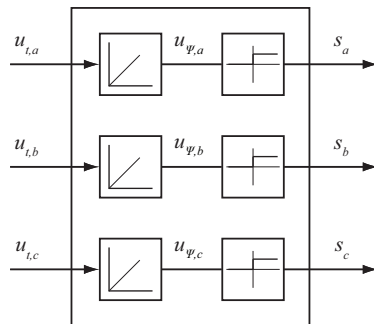


Figure 3.9: Zero stator flux detection with integrators and comparators. In practice, the integrators can be realized as first-order low-pass filters.

crossing of the signals therefore happens at a commutation instant of the inverter. Therefore, no phase-shift has to be implemented as for the zero-crossing detection of the back EMF.

- The integration of the terminal voltages, whose amplitude and frequency is proportional to the rotational speed of the machine, leads to signals $u_{\psi,a,b,c}$ with almost constant amplitude.

In practice, the integrator can be realized as a first-order low-pass RC filter with a very low cross-over frequency. A low cross-over frequency is necessary to get a phase shift of -90 degrees at as low speeds as possible. The design of such a low-pass filter is a trade-off between having a phase shift of -90 degrees at low speeds and having a signal with a larger amplitude. The zero-crossing detection of the signals $u_{\psi,a,b,c}$ can be done with comparators and leads to digital signals $s_{a,b,c}$, which can be connected to digital inputs of a DSP.

In contrary to the standard VSI, where a low inductive machine results in a high current ripple or a large output filter, for a PAM inverter with flux-zero crossing sensorless control, the low phase inductance of the PMSM is an advantage due to the negligible steady-state current displacement of the sensorless control. This means that the machine topology selected in section 2, the inverter selected in section 3.1 and the sensorless rotor position detection described here are a very good match and the ideal combination for ultra-high-speed operation.

3.3 Control

For most of the applications, the main task of the control system is the speed or torque control of the machine. This includes the commutation of the inverter switches depending on the rotor position, and the cascaded current and speed control loops. The control system also provides communication with an external interface setting the speed reference, for example a PC.

The stator-flux zero-crossing detection can be realized with a discrete low-pass filter and comparator circuit, as described in the previous section, whereas the rotor position and speed calculation can be implemented on microcontroller or a DSP. Out of the sensorless signals $s_{a,b,c}$ the inverter switching and speed calculation can be realized in software

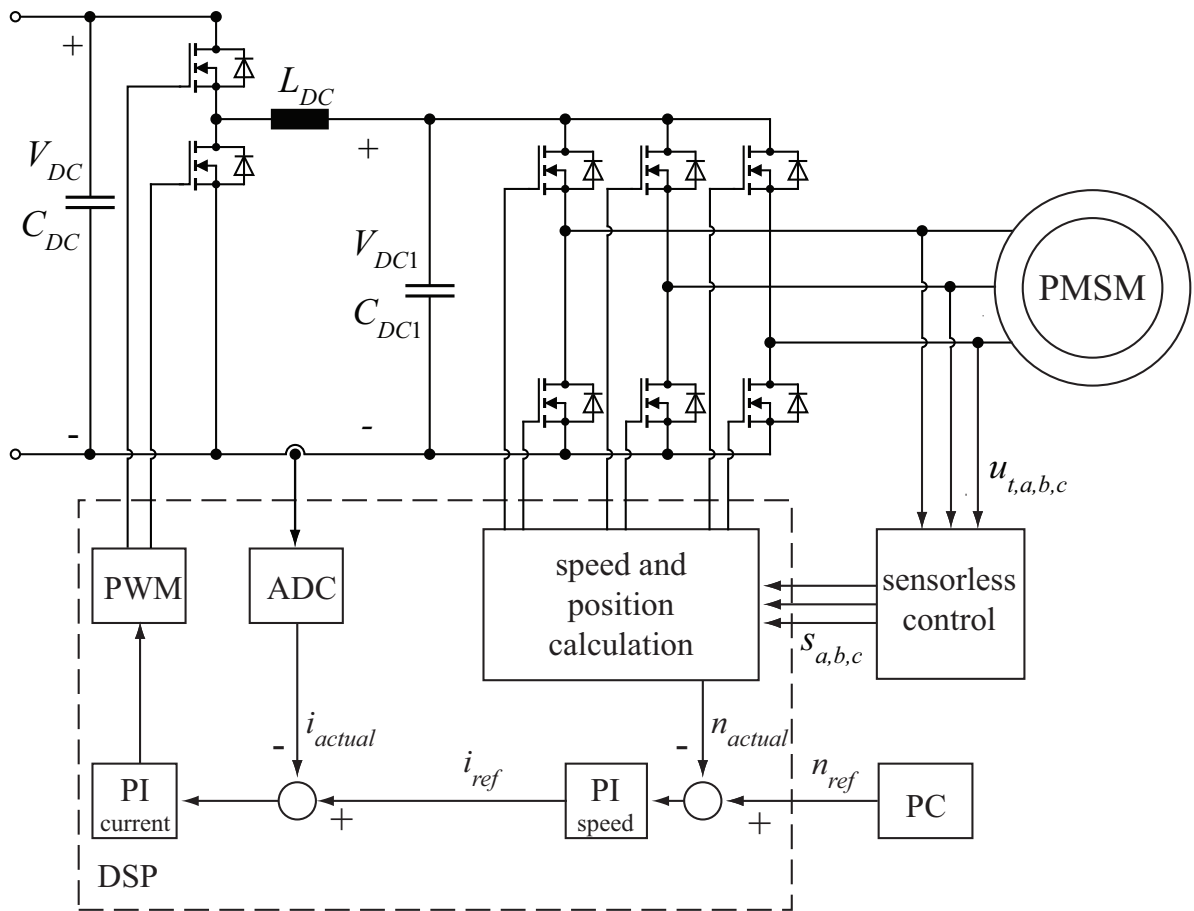


Figure 3.10: Overview about the control system of the PAM inverter. Part of the sensorless control is realized as discrete electronics, part is realized in software on a DSP. The current (or torque respectively) and speed control loop are cascaded, and the speed reference is set from an external source. The current controller controls the dc link current via the DC/DC converter.

with a short computation time. The signals directly set the state of the inverter, whereas the speed information is passed on to a speed controller. Since all considered applications need only low dynamics of the speed or torque control, simple torque control via the dc current is sufficient, which allows for a single current measurement. The current reference is set by the speed controller. The entire control structure is presented in Figure 3.10.

This low complexity control structure leads to a simple and compact control system. Further control requirements such as current limitation for electronics and machine protection, speed ramp limitations for protecting the application and the bearing system, additional control, e.g.

outer loops for pressure or mass flow control in a compressor, can be implemented in software.

3.3.1 Torque Generation

As previously shown, the phase currents in the chosen inverter-motor combination are not sinusoidal, and the instantaneous torque generated in a machine is therefore not constant. The current waveforms depend on the machine inductance and back EMF waveform.

The instantaneous torque can be calculated with (2.45) and (2.47) from the phase currents. A simulation result is shown in Figure 3.11. It can be seen that the non-sinusoidal phase currents produce a torque ripple. However, for most of the applications, this torque ripple is negligible due to the high inertia compared to the torque ripple variation, which only leads to a very small speed ripple when the inertia J is sufficiently high, according to (2.46). The usual problem of noise and vibration due to a high torque ripple is outweighed by the noise and vibration of the application, for example in drilling spindles and turbocompressors.

Hence, only the mean torque is considered. For steady-state operation and neglecting the diode conduction angle, and during the conduction, i.e. on-state, of the upper MOSFET in a phase leg, the mean value of the phase current equals the dc current. Due to the sinusoidal back EMF, only the fundamental current waveform contributes to the average torque generation. Assuming block currents in the phases, the fundamental component (peak) of the phase current, and therefore the q -current can be calculated with

$$\hat{i}_{ph,1} = i_q = i_{dc} \frac{2\sqrt{3}}{\pi} \quad (3.2)$$

and therefore the average electromagnetic torque can be written as a function of the dc current i_{dc} with

$$T_e = \frac{3\sqrt{3}}{\pi} \psi_{pm} i_{dc} . \quad (3.3)$$

The instantaneous and the fundamental current waveforms in one phase, the dc current, the instantaneous and the average electromagnetic torque are depicted in Figure 3.11.

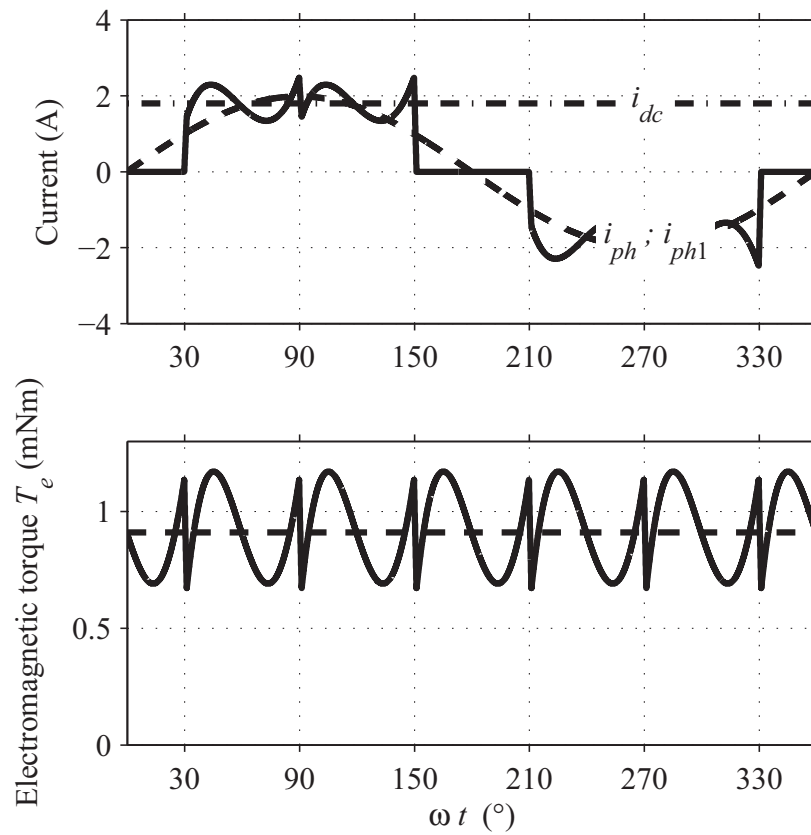


Figure 3.11: Instantaneous (solid) and fundamental (dashed) current waveforms in one phase of the machine, and the dc current, instantaneous (solid) and average (dashed) electromagnetic torque.

Chapter 4

System Integration

4.1 Bearing Technology

4.1.1 Requirements

For machine speeds in the range of 500 000 to 1 000 000 rpm the selection of a suitable bearing is a main issue. In this Thesis, the focus is on the electrical drive system and not on the bearing, and no bearing system is designed. However, in order to build experimental setups and running systems, a suitable bearing has to be evaluated. Therefore, in the following, a short overview about different bearing technologies is given, different high-speed bearings from literature are reported, and advantages and disadvantages of the bearings are compared.

The requirements, besides the feasibility for highest speed operation, can be very different depending on the application. The mechanical load is high in a machining spindle, but low in a rotating optical mirror. The running hours between service intervals is short in a medical drill compared to a heat pump compressor that might run nonstop for years. The bearing losses in a flywheel application are critical, whereas high losses and a low efficiency is no problem in a turboexpander in a cryogenic plant, where energy is wasted as heat anyway. The bearing close to the turbine side in a gas turbine has to suffer high temperatures, whereas in a compressor sucking in ambient air the cooling is almost perfect. A

turbocompressor delivering air to a fuel cell has to be oil-free, whereas the gearboxes in a dental handpiece have to be lubricated daily with an oil-spray. Therefore, no single choice for a bearing can be made for ultra-high-speed electrical machines, it very much depends on the application. After the comparison of the different bearings, three application examples of bearing choice are given.

4.1.2 Bearing Types

Ball Bearings

Standard ball bearings are not feasible for highest speeds. Hence, manufactures usually give limit speeds in the dimensionless " $n \times d$ ", which means rotational speed in rpm times shaft diameter of the bearing in mm. For standard bearings, the limits are in the range of a few 100 000 up to about 2 million for special miniature high-speed bearings. Such specialized bearings are commonly used in the dental industry, and bearings are available for speeds up to 400 000 rpm, with an according diameter in the range of 3-6 mm.

The main advantages of ball bearings are the robustness, stiffness and small size. Disadvantages are the limited operating temperature depending on materials and lubrication and relatively high losses at high speed, see section 5.3.4. However, the main disadvantage is the limited lifetime dependent on lubrication, load and especially speed.

Air Bearings

Static air bearings, dynamic air bearings and foil bearings levitate the rotor with air pressure, either generated with an external supply (static) or by spinning the rotor (dynamic and foil). They all show low friction losses and a long lifetime. Furthermore, depending on the air bearing type and materials used, high temperature operation is possible. The drawback is a speed limit due to instabilities, especially with heavy rotors such as in permanent-magnet machines. No satisfactory designs or experimental results have been presented for speeds above 500 000 rpm, and no air bearings are commercially available in this area.

Static air bearings are widely used in machining spindles i.e. in PCB drilling [5], [24], where external pressure supply is easily available. In in-

dustry, the highest speeds achieved today are in the area of 200 000 rpm. A hydrostatic thrust bearing design resulting from a MEMS gas turbine research project was running at a maximum speed of 1.4 million rpm [25], [61]. For applications where an external power supply is not available, dynamic or foil air bearings are reported. MiTi verified a foil bearing at speeds up to 700 000 rpm and temperatures up to 650°C [27] and for a miniature gas turbine, bearings are tested in [26] up to 770 000 rpm. Further theoretical analysis and experimental verification of high-speed gas bearings is presented in [62] and [63].

Magnetic Bearings

Magnetic bearings levitate the rotor using magnetic forces and have similar advantages as air bearings, because they also work without mechanical contact. In contrary to air bearings, they are limited in temperature due to the usual permanent magnets and copper windings used.

Active magnetic bearings require sensors, actuators and control, which results in high complexity and increased bearing volume. Furthermore, the high dynamic rotor position control requires a high bandwidth in current and position measurement and controllers. Furthermore, due to its complexity, and therefore probability of failure, usually an emergency bearing is needed. The challenges and possible solutions are described in [64], [65] and [66].

In [67], a passive magnetic bearing concept for supporting high-speed rotors has been presented and experimentally verified up to 90 000 rpm. It is a homopolar electrodynamic bearing with ring magnets that induce stabilizing eddy currents without the need for any control electronics. Beside the advantage of no extra controller and position measurement needed, it also has a small size. However, it is no option due to increasing instabilities with increasing speed and low stiffness.

Hybrid Bearings

Hybrid bearings can incorporate the advantages and eliminate the drawbacks of different bearing types. For example, a combined aerodynamic and magnetic bearing can eliminate the wear of the air bearing at start and stop and provide a control and stabilization possibility, whereas the

air bearing can take the main load [68]. Another example is the commonly used emergency ball bearings in magnetic bearings preventing a crash of the rotor if the magnetic bearings fails.

4.1.3 Application Examples

The different requirements of the applications and the difference in advantageous and disadvantageous of the bearing types lead to individual choices. Three examples of high-speed applications are presented here. In a dental drill the mechanical load is high in axial and radial direction, and the bearings can be changed regularly. Therefore the ball bearing is the preferred option. In a flywheel storage, the losses of a bearing are critical and the bearing has to usually work in vacuum, therefore, the magnetic bearing is the optimal choice. In a miniature gas turbine, the temperatures are elevated and therefore the air bearing is the only option.

All the measurements for this Thesis have been made with test benches and demonstrators running on ball bearings. This is due to the simplicity, robustness against mechanical impacts, small size, avoidance of auxiliary equipment and availability of miniature high-speed ball bearings.

4.2 Thermal Design

A thermal design of power electronics, an electrical machine, and an application always has the goal of keeping the temperature within the operating limits of the parts and materials used. In an ultra-high-speed electrical drive system an its integrated application there are two very distinct thermal considerations different from other systems.

Whereas for the power electronics a standard thermal design can be made, this is different for the machine. As seen in Figure 2.19 the losses for a machine with constant power rating increase with increasing speed, even if the machine is optimized for lowest losses. This is mainly due to higher air friction losses. To make it worse, as can be seen in Figure 2.18, the outer radius of the machine decreases with increasing speed, this is due to the lower torque demand. This combination leads to an increased losses per surface area for increasing speed, as can be seen in Figure 2.20. As a result, the higher the rotational speed, the more losses have to be

cooled with a smaller surface in order to fulfill the operating limits of the materials. This requires an increased effort in the thermal design.

A second consideration is, as for the bearings, again very dependent on the application. For example, in a gas turbine application, there is excessive heat from the combustion and the turbine side, which heats the rotor of the machine and also, depending on the thermal insulation, the electrical generator. In contrary, in a compressor application for an air pressurization of an airplane, e.g. the Solar Impulse system, the intake air temperature is below zero degrees Celsius, and therefore a very good cooling of the machine is present, and the air might has to be heated intentionally.

Thermal calculations can be made analytically or with finite element simulations, depending on the complexity of the system. As an example, the thermal design for two very different systems, the two-stage Solar Impulse cabin air pressurization compressor and the 1 million rpm demonstrator, is presented. The 1 million rpm demonstrator has a very simple geometry, and can therefore be modeled analytically. It consists of a machine as shown in Figure 2.1 with two ball bearings on each end of the rotor, and the back side of the machine is attached to a test bench, which also provides cooling. The main goal in the thermal design is to avoid temperatures above 200 °C in the bearings. They are most critical due to the high bearing losses and the poor thermal connection of the bearings to the machine stator. The thermal model of this demonstrator can be seen in Figure 4.1 and the loss components and the resulting temperatures of the knots of the thermal model can be found in Figure 4.2.

In the Solar Impulse air pressurization compressor, the intake air temperature is -56 °C, and therefore one goal of the thermal design is to keep the temperature in the ball bearings above 0 °C. A second goal is to cool the motor. Both goals have been achieved by guiding the intake air around the motor. The Solar Impulse compressor has a more complex geometry than the 1 million rpm demonstrator, and therefore the thermal design is done with finite element simulations. The results can be found in Figure 4.3. It can be seen that the temperatures in the bearings can be kept above zero with an according flow director 1 and guiding the air around the generator.

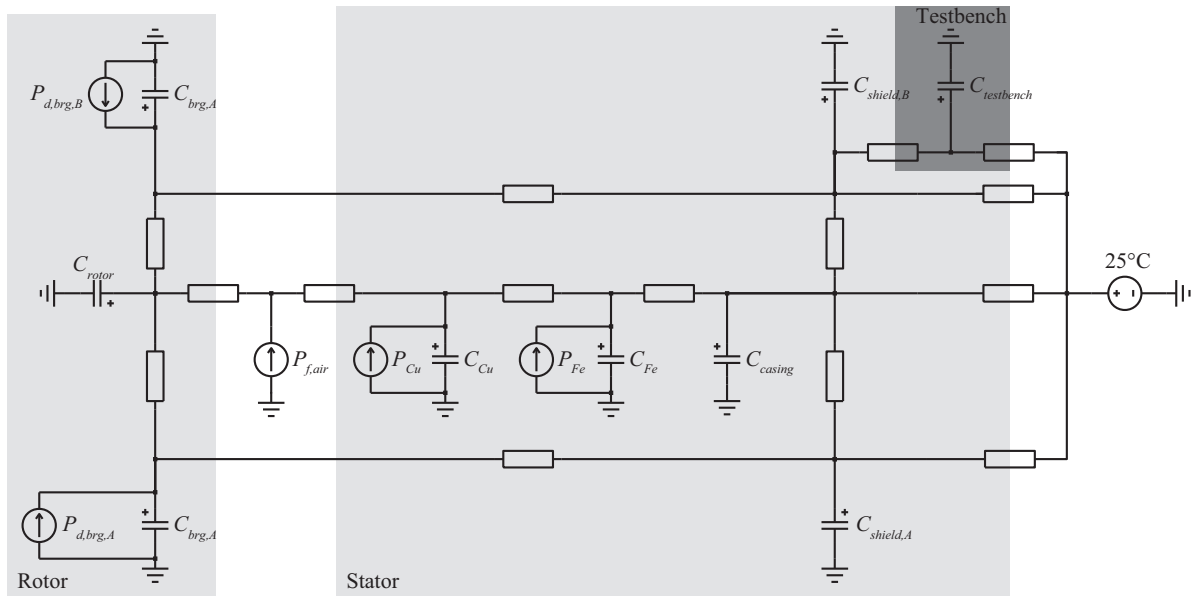


Figure 4.1: Thermal model of the 1 million rpm demonstrator system.

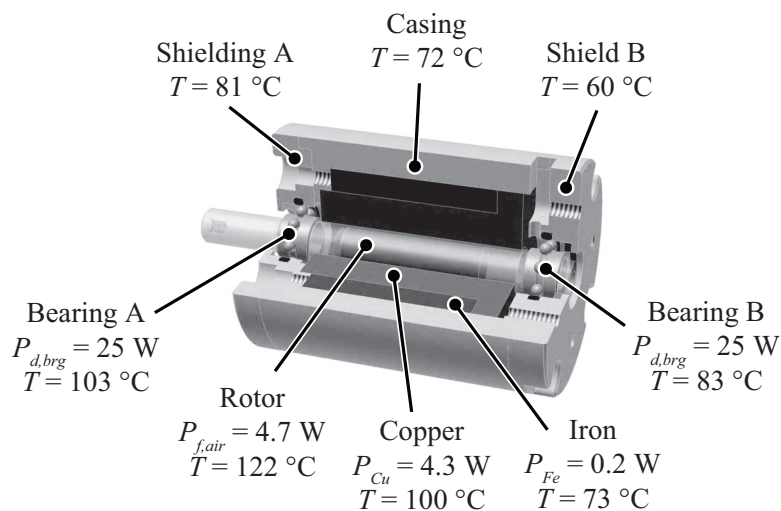


Figure 4.2: Power losses and resulting temperatures in the 1 million rpm demonstrator calculated with the thermal model presented in Figure 4.1.

4.3 Rotordynamics

4.3.1 Motivation

Ideally, a rotor is perfectly balanced, i.e. that means the geometrical centerline equals the centerline of mass. However, in reality, every rotor has unbalance, which excites vibrations. As the speed of rotation increases

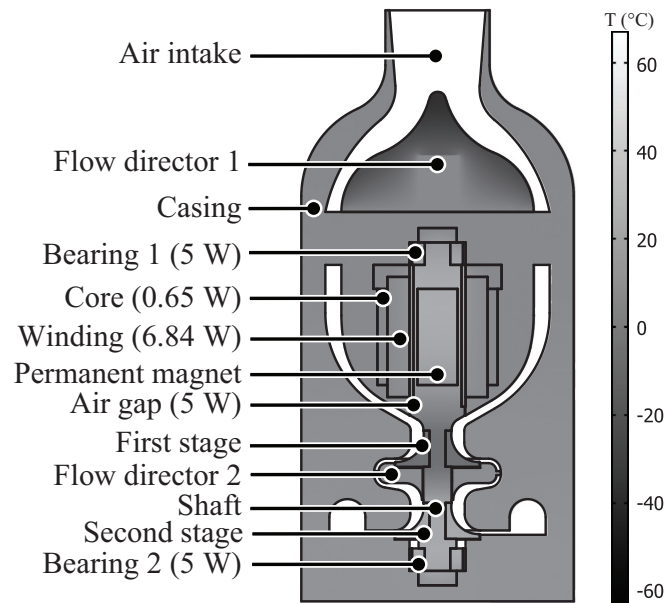


Figure 4.3: Power losses and resulting temperatures in the Solar Impulse two-stage turbocompressor system calculated with an FE simulation.

the amplitude of this vibration often passes through a maximum that is called a critical speed. If the amplitude of vibration at these critical speeds is excessive, catastrophic failure occurs; either the bearing fails or even the rotor structure disintegrates. Therefore, the main goal of the rotordynamic analysis is to determine those critical speeds and avoid a constant operation at these speeds. This can be done with adapting the operational speed, or changing the bearings or the rotor geometry and material and therefore shifting the critical speeds. Furthermore, the critical speeds should be passed quick enough to protect the rotor construction and bearings.

There are several commercial tools available for determining critical speeds, usually based on 1D or 3D Finite Element rotor models. However, they have the drawback that they are usually computational intense and do not have an interface for access by external programs, for example the optimization routine presented in section 2.4. Furthermore, for the simple rotor geometries used in the motor concepts presented in this Thesis, a simple algorithm for calculating the critical speeds is sufficient. Therefore, a simple, calculation efficient code is presented.

When the rotor dynamic analysis is used in the optimization routine, it checks the optimized machines concerning critical speeds and even-

tually constrains the geometry of the rotor such that the third critical speed (the first bending mode of the rotor without bearings) is above 120% of the rated speed.

4.3.2 Modeling

Euler-Bernoulli Beam Equation

The rotordynamic analysis is based on the one-dimensional Euler-Bernoulli beam equation (Figure 4.4, [69])

$$\frac{\partial^2}{\partial z^2} \left(EI_{xy} \frac{\partial^2 \psi_x}{\partial z^2} \right) + q = 0 \quad (4.1)$$

where the ψ_x is the the deflection of the beam in the direction of x at the position z , q is the distributed load (force per unit length). E is the elastic modulus and I_{xy} is the area moment of inertia.

For dynamic calculations, the equation is extended with the distributed mass moment of inertia depending on the cross section area A and the density ρ . Furthermore, the bearings are modeled as deflection-depending force $c_b \psi$. This leads to

$$\rho A \frac{\partial^2 \psi_x}{\partial t^2} + \frac{\partial^2}{\partial z^2} \left(EI_{xy} \frac{\partial^2 \psi_x}{\partial z^2} \right) + c_b \psi + q = 0. \quad (4.2)$$

On a body with a rotational speed ω around the z -axis with the inertia J_z the gyroscopic effect describes the torque generated in direction of the y -axis at a rotation around the x -axis with the angular speed $\dot{\varphi}_x$ and vice versa. Therefore, two differential equations for the deflection in x -axis direction ψ_x and in y -axis direction ψ_y are coupled and extended with the gyroscopic terms leading to

$$\rho A \frac{\partial^2 \psi_x}{\partial t^2} + \frac{\partial^2}{\partial z^2} \left(EI_{xy} \frac{\partial^2 \psi_x}{\partial z^2} \right) - 2\omega I_{xy} \rho \frac{\partial^3 \psi_y}{\partial t \partial z^2} + c_b \psi_x + q_x = 0 \quad (4.3)$$

$$\rho A \frac{\partial^2 \psi_y}{\partial t^2} + \frac{\partial^2}{\partial z^2} \left(EI_{xy} \frac{\partial^2 \psi_y}{\partial z^2} \right) + 2\omega I_{xy} \rho \frac{\partial^3 \psi_x}{\partial t \partial z^2} + c_b \psi_y + q_y = 0 \quad (4.4)$$

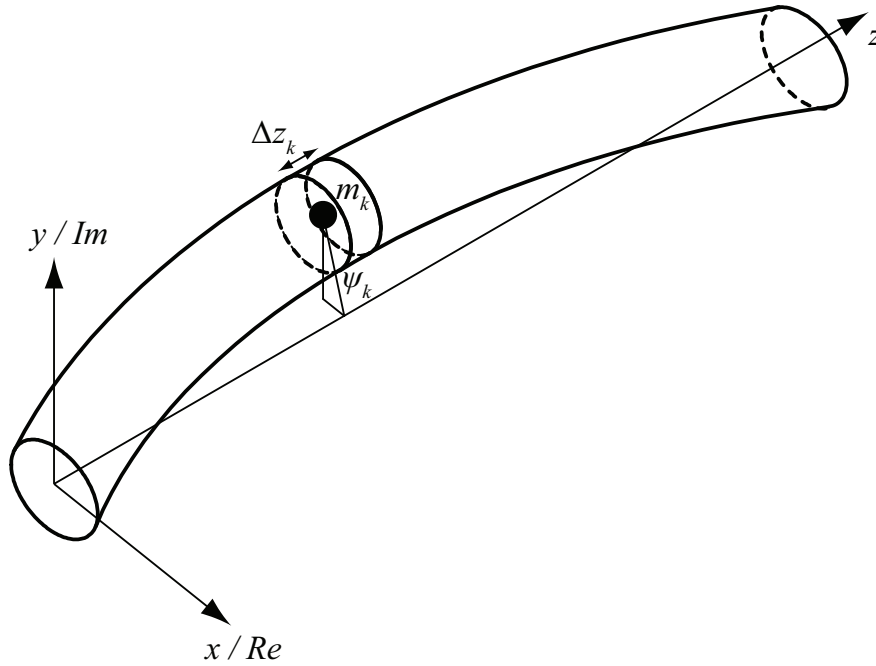


Figure 4.4: Finite element modeling of a rotor.

or with the complex deflection ψ

$$\rho A \frac{\partial^2 \psi}{\partial t^2} + \frac{\partial^2}{\partial z^2} \left(EI_{xy} \frac{\partial^2 \psi}{\partial z^2} \right) + 2j\omega I_{xy} \rho \frac{\partial^3 \psi}{\partial t \partial z^2} + c_b \psi + q = 0 \quad (4.5)$$

where

$$\psi_x = \Re(\psi) \quad (4.6)$$

$$\psi_y = \Im(\psi). \quad (4.7)$$

Numerical Solution

For the rotordynamic analysis the distributed load q is set to zero, it could be used e.g. for unbalance calculations or influence of magnetic forces. Furthermore, in order to be able to solve any rotor geometry, the rotor is discretized into n_q pieces along the z -axis as shown in Figure 4.4 and therefore (4.5) is written in matrix representation as

$$M\ddot{\psi} + j\omega G\dot{\psi} + S\psi = 0 \quad (4.8)$$

where M is the mass matrix, G the gyroscopic matrix and S the stiffness matrix. Inserting

$$\psi(t) = \hat{\psi}e^{j\omega_{res}t} \quad (4.9)$$

in (4.8) leads to

$$\omega_{res}^2 \hat{\psi} + \omega_{res}\omega M^{-1}G\hat{\psi} - M^{-1}S\hat{\psi} = 0. \quad (4.10)$$

which results in a quadratic eigenvalue problem with the eigenvalues ω_{res} and the eigenvectors $\hat{\psi}$.

System Matrices

The mass matrix contains the masses of the discrete elements as shown in (4.11).

$$M = \begin{pmatrix} m_1 & & & 0 \\ & m_2 & & \\ & & \ddots & \\ 0 & & & m_{n_q} \end{pmatrix} \quad (4.11)$$

The gyroscopic matrix G is derived from $2\rho I_{xy} \frac{\partial^3 \psi}{\partial t \partial z^2}$ out of (4.5). With the relationship of inertia and area moment if inertia $J_{z,k} = 2\Delta z \rho I_{xy}$ and the derivation matrix V_{II} (see (4.21)) it can be written as

$$G = J_z V_{II,b}. \quad (4.12)$$

The stiffness matrix contains the matrix defining the elasticity of the rotor EI_{xy} (4.23), the bearing stiffness C_b (4.25), the lengths of the discrete elements Δz (4.25) and the two derivation matrices (4.16) and (4.21). The matrix S is defined as

$$S = \Delta z V_{II,a} EI_{xy} V_{II,b} + C_b \quad (4.13)$$

Auxiliary Matrices

There are two boundary conditions that result in two derivation matrices. There is no material at the ends of the beam to transfer a force to and from, i.e.

$$EI_{xy,0} = 0 \quad (4.14)$$

$$EI_{xy,q_n+1} = 0 \quad (4.15)$$

and therefore the derivation matrix $V_{II,a}$ is

$$V_{II,a} = \begin{pmatrix} c_1 & & & 0 \\ & c_2 & & \\ & & \ddots & \\ & & & c_{n_q-1} \\ 0 & & & & c_{n_q} \end{pmatrix} \begin{pmatrix} -\frac{\Delta z_1}{2+\delta_2} & \frac{\Delta z_1}{2} & & 0 \\ \delta_3 & -(\delta_2 + \delta_3) & \delta_2 & \\ & \ddots & \ddots & \ddots \\ & \delta_{n_q} & -(\delta_{n_q-1} + \delta_{n_q}) & \delta_{n_q-1} \\ 0 & & \frac{\Delta z_{n_q}}{2} & -\frac{\delta_{n_q} + \Delta z_{n_q}}{2} \end{pmatrix} \quad (4.16)$$

where

$$c_k = \begin{cases} \frac{1}{\Delta z_1/2\delta_2(\Delta z_1/2 + \delta_2)} & k = 1 \\ \frac{1}{\delta_k\delta_{k+1}(\delta_k + \delta_{k+1})} & 2 \leq k \leq n-1 \\ \frac{1}{\delta_{q_n}\Delta z_{n_q}/2(\delta_{q_n} + \Delta z_{n_q}/2)} & k = n \end{cases} \quad (4.17)$$

and

$$\delta_k = z_k - z_{k-1} = (\Delta z_k + \Delta z_{k-1})/2. \quad (4.18)$$

Furthermore, the ends of the beams are free, i.e.

$$\psi_1'' = 0 \quad (4.19)$$

$$\psi_{n_q}'' = 0 \quad (4.20)$$

which leads to the derivation matrix $V_{II,b}$ as

$$V_{II,b} = \begin{pmatrix} 0 & & 0 \\ & 1 & \\ & & \ddots \\ & & & 1 \\ 0 & & & & 0 \end{pmatrix} V_{II,a}. \quad (4.21)$$

The inertia matrix can be written as

$$J_z = \begin{pmatrix} J_{z,1} & & 0 \\ & J_{z,2} & \\ & & \ddots \\ 0 & & & J_{z,n_q} \end{pmatrix}. \quad (4.22)$$

The matrix EI_{xy} is defined as

$$EI_{xy} = \begin{pmatrix} EI_{xy,1} & & 0 \\ & EI_{xy,2} & \\ & & \ddots \\ 0 & & & EI_{xy,n_q} \end{pmatrix} \quad (4.23)$$

where the single components can be calculated with

$$EI_{xy,k} = \frac{\pi}{4} r^4 E_k \quad (4.24)$$

where r is the cylinder radius and E_k the Young's modulus of the specific element.

The bearing matrix can be written

$$C_b = \begin{pmatrix} c_{b,1} & & & 0 \\ & c_{b,2} & & \\ & & \ddots & \\ 0 & & & c_{b,n_q} \end{pmatrix} \quad (4.25)$$

where the bearing stiffnesses $c_{b,k}$ of the single elements are zero beside at one point for each bearing. The matrix Δz is defined as

$$\Delta z = \begin{pmatrix} \Delta z_1 & & & 0 \\ & \Delta z_2 & & \\ & & \ddots & \\ 0 & & & \Delta z_{n_q} \end{pmatrix} \quad (4.26)$$

4.3.3 Results

Campbell Diagram and Critical Speeds

Due to the gyroscopic effect the eigenvalues are speed dependent. An interesting phenomena is that depending on the rotational direction of the eigenfrequency, the resulting gyroscopic torque is either accelerating or breaking, which leads to the so called backward or forward whirl. These eigenvalues are usually plotted in the Campbell diagram as function of the rotational speed. The intersection of the speed dependent eigenvalues with the identity leads to the critical speeds.

As an example, the rotor of a turbocompressor for a rated speed of 500 000 rpm is analyzed. It consists of a permanent magnet for the electrical machine encased in a titanium sleeve, onto which the impeller wheel, made out of aluminum, is attached. The rotor is supported by two high-speed ball bearings, one in between the impeller and the motor, and one at the back end of the rotor. A CAD cut away view can be found in Figure 5.3. In order to avoid dangerous excitations, the rotor construction has been adjusted such that the rated speed falls in between the second and third critical speed. In Figure 4.5 the deflection of the rotor in the resulting eigenfrequencies at standstill are shown. Figure 4.6 depicts the Campbell diagram for this rotor, where it can be seen that the backward and forward whirl are very close to each other. Furthermore, it can be seen that the first two critical speeds are dominated by the

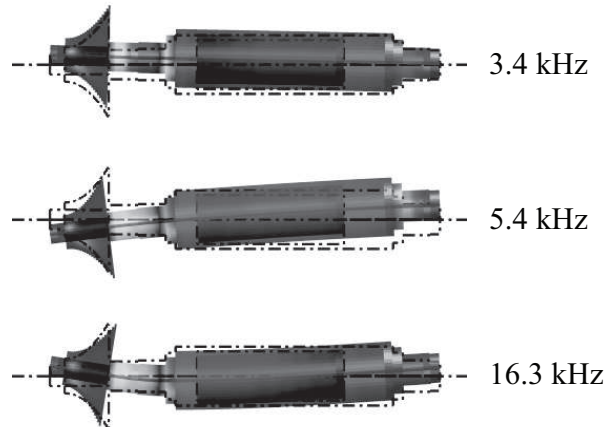


Figure 4.5: Deflection of the turbocompressor rotor at the resulting eigenfrequencies at standstill. The color indicates the value of deflection and therefore the location of highest stresses.

bearing stiffness and the main deflection occurs at the bearing positions. Therefore, these two critical speeds can be damped efficiently with an according bearing setup. However, the third critical speed is mainly due to the rotor stiffness and can therefore not be damped by the bearings. Therefore, passing through the third critical speed is most critical and if possible has to be avoided.

Comparison with Commercial Tools

There is various commercial tools for the analysis of rotordynamics, usually also based on 1-D models or on 3-D finite element solvers. As mentioned in the beginning, those are not suitable for a integrated design and optimization process. However, for comparison of the results they are feasible. With a standard, multiphysics, 3-D finite element solver, the eigenfrequencies of the same rotor of the turbocompressor have been calculated. The finite element simulations do not include the gyroscopic effect, but the results match the analytical model as can be seen in Figure 4.7, therefore either rotordynamic analysis is suited for the rotors under investigation. However, integrating the rotordynamic analysis into an optimization routing, the solution presented in section 4.3.2 is preferred.

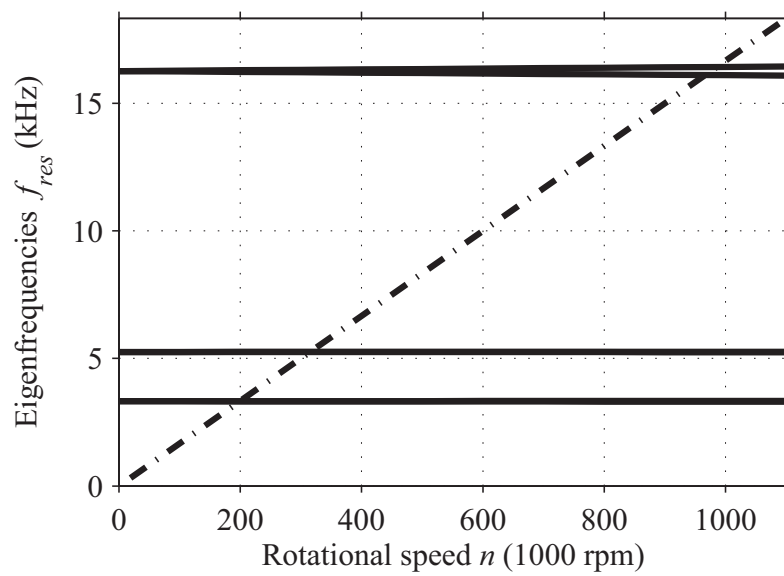


Figure 4.6: Campbell diagram for the 500 000 rpm turbocompressor rotor. The critical speeds are at the intersection of the rotational speed dependent eigenfrequencies f_{res} with the identity. The backward and forward whirl is only visible for the third critical speed.



Figure 4.7: Deflection of the turbocompressor rotor at the resulting eigenfrequencies at standstill, calculated with a commercial finite element solver. The color indicates the value of displacement from the original position.

Chapter 5

Experimental Results

In this chapter, the hardware and experimental results of two systems are presented. Existing systems running at rated speed are especially important for this research, because other systems reported in literature from research and industry have not achieved speeds above 450 000 rpm, [20]. Therefore, the feasibility of the design routines presented in this Thesis is proved with hardware demonstrators and measurements for speeds up to 1 million rpm.

5.1 Hardware

5.1.1 1 Million rpm System

In order to prove the feasibility of the electrical drive systems for speeds up to 1 million rpm a demonstrator has been designed and realized. It consists of a motor as presented in section 2 optimized for highest efficiency at a rated speed of 1 million rpm and a rated power of 100 W. The power and control electronics are built for a maximum power of 200 W, a dc link voltage of 60 V, and with a sensorless control as presented in section 3. The technical details are given in Table 5.1 and a photo of the demonstrator can be seen in Figure 5.1.

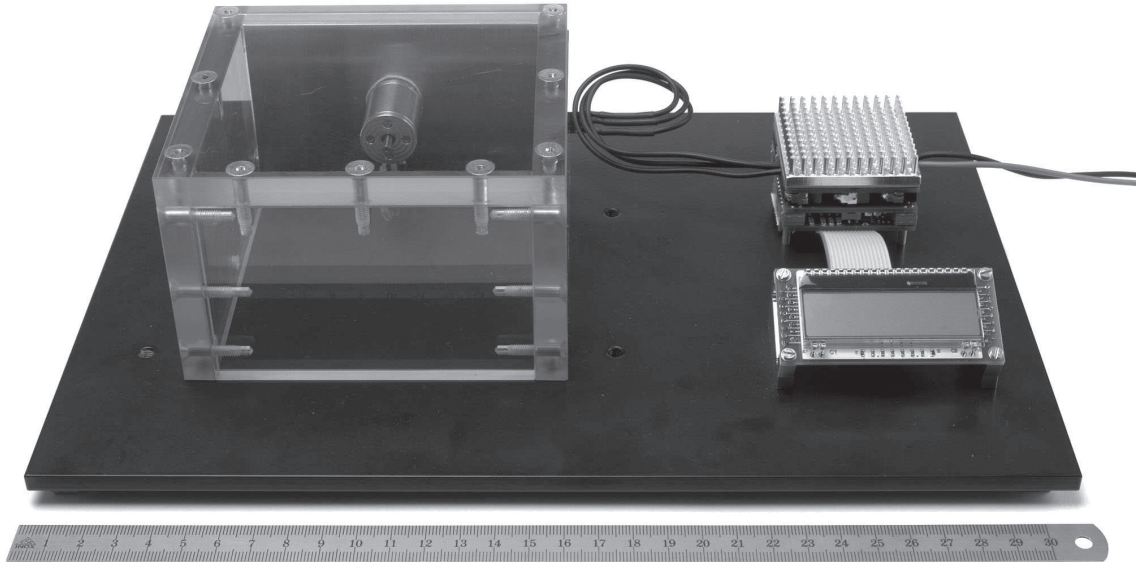


Figure 5.1: Photo of the 1 million rpm demonstrator. The machine is covered with a see-through security box, and a display is connected to the electronics in order to show the current speed.

5.1.2 500 krpm System

For a portable gas turbine project [70] and the Solar Impulse cabin air pressurization system based on a miniature turbocompressor [71], a drive system with a rated speed of 500 000 rpm and a rated power of 100 W has been developed. The machine winding is optimized for low eddy current losses, however the total machine is not optimized according to section 2.4, but designed with a traditional method only considering copper and iron losses. This allows for a comparison with an optimized design. Furthermore, there is two versions of the machine, one with a stator core of silicon-iron laminations, a second one with amorphous iron laminations, resulting in either 4.5 W or 0.5 W of iron losses at rated speed. The power and control electronics are built for a maximum power of 150 W, a dc link voltage of 30 V, and with a sensorless control as presented in section 3.

In one case this drive system is operating as a starter/generator for a

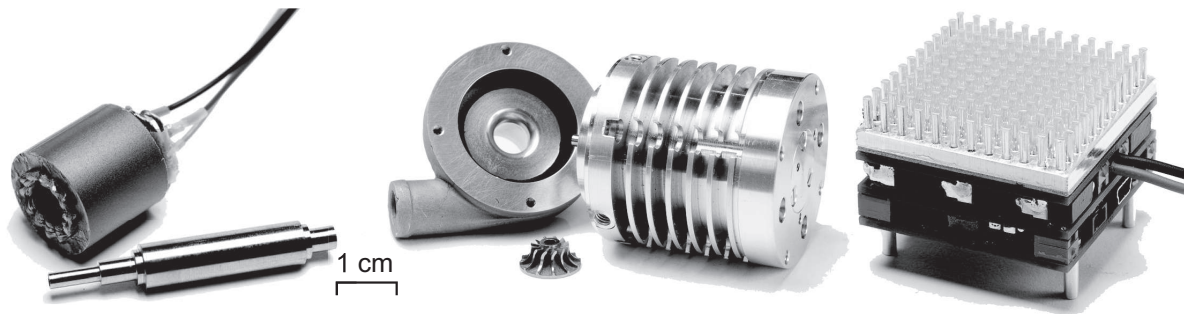


Figure 5.2: Photo of the 500 krpm system with stator and rotor parts (left), its integration into the miniature turbocompressor (middle) and the power and control electronics (right).

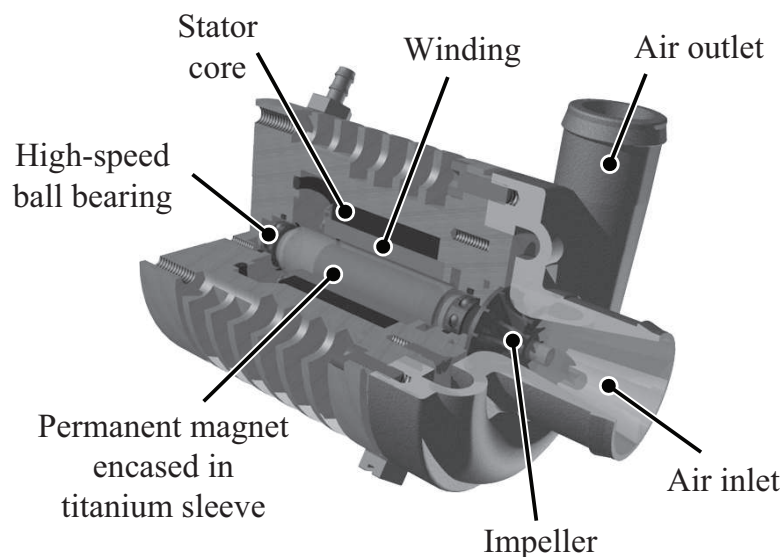


Figure 5.3: Cut away view of the miniature turbocompressor showing the inner construction.

gas turbine, in the other case it is purely run in motor operation in order to drive a radial turbocompressor, which supplies the Solar Impulse airplane cabin with air at 12 000 m altitude in order for one pilot to be able to breath. A photo of the single parts and the integrated turbocompressor system can be found in Figure 5.2, a CAD cut away view is presented in Figure 5.3 and the technical data is collected in Table 5.1.

		500 krpm	1 Mrpm
Rated speed	n_r (krpm)	500	1 000
Rated power	P_r (W)	100	100
Rotor radius	R_2 (mm)	3	1.75
Stator radius	R_5 (mm)	8	7
Active length	L (mm)	15	11.5
First critical speed	(kHz/krpm)	2.9/176	3.4/206
Second critical speed	(kHz/krpm)	4.6/276	4.9/293
Third critical speed	(kHz/krpm)	14.3/858	18.0/1080
Copper losses	P_{Cu} (W)	5.5	4.3
Iron losses	P_{Fe} (W)	$4.5^1/0.5^2$	0.2
Air friction losses	$P_{f,air}$ (W)	6.5	4.7
Stator resistance	R_s (Ω)	0.13	0.36
Stator inductance	L_s (μ H)	2.25	11.5
PM flux linkage	ψ_{pm} (mVs)	0.306	0.243
DC link voltage	V_{DC} (V)	30	60
DC/DC switching frequency	f_s (kHz)	200	200
DC link inductance	L_{DC} (μ H)	30	60

¹ silicon-iron, ² amorphous iron

Table 5.1: Data for the two experimental systems.

5.2 Power and Control Electronics Measurements

The correct functionality of the power and control electronics is verified with the 1 million rpm demonstrator. In Figure 5.4 the waveforms of the drive system running at 1 000 000 rpm are shown.

5.3 Machine Measurement Methods and Results

Measurements are undertaken to verify the theoretical machine design and the determination of losses not considered in the design, mainly the bearing losses. Previously reported high-speed test benches are realized

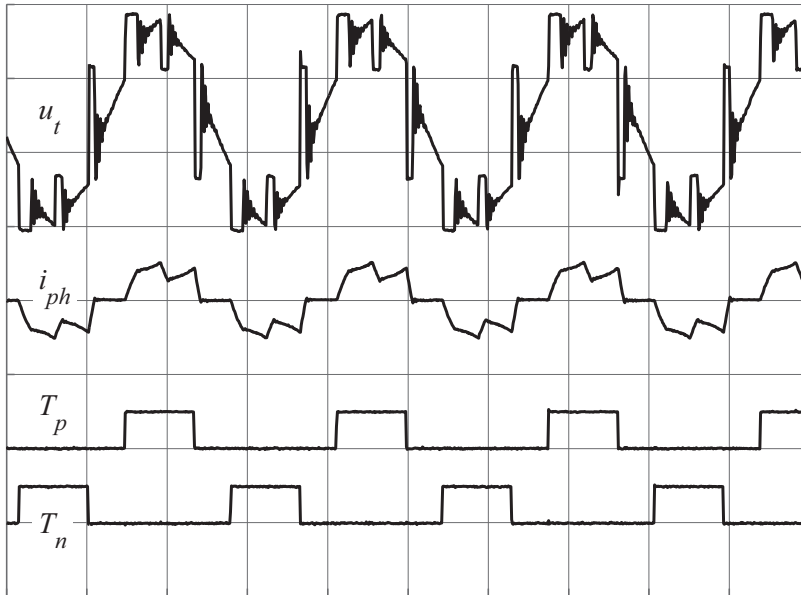


Figure 5.4: Waveforms of the demonstrator at 1.1 million rpm: terminal voltage (u_t , 50 V/div), phase current (i_{ph} , 5A/div), and positive (T_p) and negative (T_n) switching signal of the corresponding half bridge. The time scale is 20 μ s/div.

using available hardware, such as mechanical couplings, ball bearings, torque transducers and temperature sensors, since the speed is limited to a few tens of thousand rpm, and the power is in the range of kW with a torque of several Nm (e.g. [72]). In contrast, significant challenges exist to measure on machines with operating speeds exceeding 500 000 rpm and measuring very low torque values of mNm at high speeds.

5.3.1 Machine Resistance and Inductance Measurements

The machine inductance and resistance is measured using standard 4 line measurement methods on the machine stator, usually when the rotor is removed. The inductance for all machines is within a few percent of the calculated value. With the measured resistance, which also is within a few percent of the estimated value, the dc copper losses in the machine can be calculated according to

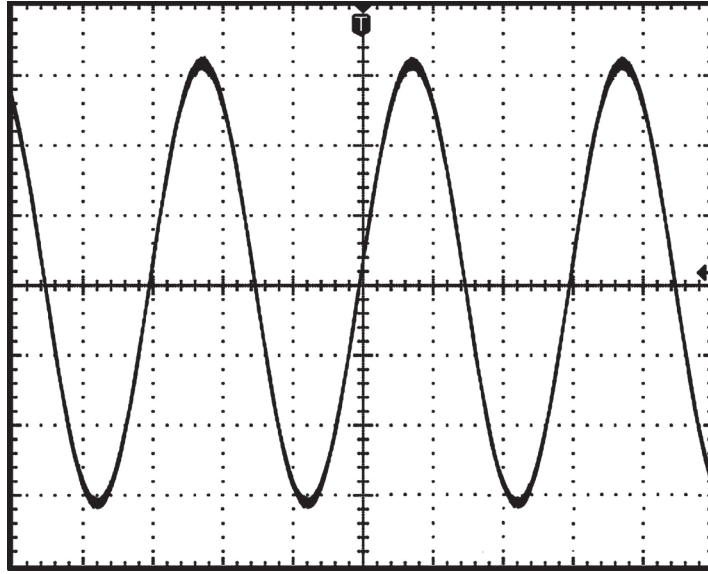


Figure 5.5: Waveforms of the 500 krpm machine at 500 000 rpm. The voltage scale is 5 V/div and the time scale is 40 μ s/div.

$$P_{Cu,dc} = I^2 R_{dc}. \quad (5.1)$$

Since all the machines constructed are optimized for highest efficiency, the resulting strand diameters are in the area of tens of micrometers in order to limit the proximity effect losses. Therefore, compared to dc and proximity effect losses, the skin effect losses are very small and are therefore omitted.

5.3.2 Back EMF Measurement

Beside the phase inductance and resistance, the permanent-magnet flux linkage has to be determined in order to fully describe the machine model presented in section 2.5. This can be done by measuring the back EMF from the open-loop phase voltage. To achieve open-loop operation, meaning zero phase currents, either the machine is driven as generator, or the speed of the machine is increased in motor mode and then the inverter is switched off. The permanent-magnet flux linkage can then be calculated using (2.40) and setting $\dot{i}_s = 0$. For the 500 krpm machine, the 16 V peak measured at 500 000 rpm, as shown in Figure 5.5, exactly matches the value given by the design calculations.

5.3.3 Reaction Torque Measurement

With the knowledge of the permanent-magnet flux linkage the torque per current can be calculated according to (2.42). Nevertheless it can also be measured directly for verification by driving the machine as a generator with an external motor and connecting a variable resistive load to the machine under investigation. Since the inductive voltage drop $j\omega L_s$ is very small compared to the back EMF especially at low speed, the phase shift between current and back EMF can be neglected and i_q of (2.42) equals the peak values of the phase currents. The stator is held with low static friction ball bearings and the reaction torque on the stator is measured with a load cell. The copper dc losses and the ball bearing losses are not measured with this setup, but the air friction losses and eddy current losses in copper and iron are included in the measured torque. However, the reaction torque measurement has been undertaken at low speed where these losses can be neglected.

With this measurements, the machine design can be verified. However, the accuracy of this method is not good enough to measure small differences in e.g. iron losses which only lead to torque differences in the sub-mNm area. Achieving a good accuracy when measuring low torques in the area of mNm is a difficult task and an area of research itself [73], [74].

For the 500 krpm machine the predicted and measured torque is shown in Figure 5.6, and it can be seen that they match very well.

5.3.4 Deceleration Test

In order to fully verify the machine characteristics from the design stage, the calculated losses from section 2.3.3 and the bearing losses are measured. The dc copper losses can be determined with (5.1), and all other losses can be measured with the deceleration test. For these measurements the machine under investigation is spun up to approximately 110% of the rated speed and then the drive system is switched off such that only the losses decelerate the rotor. The angular speed ω is measured over time from the back EMF, and with knowing the speed gradient $\partial\omega/\partial t$ the braking torque $T_{d,dec}$ and power losses $P_{d,dec}$ are calculated according to

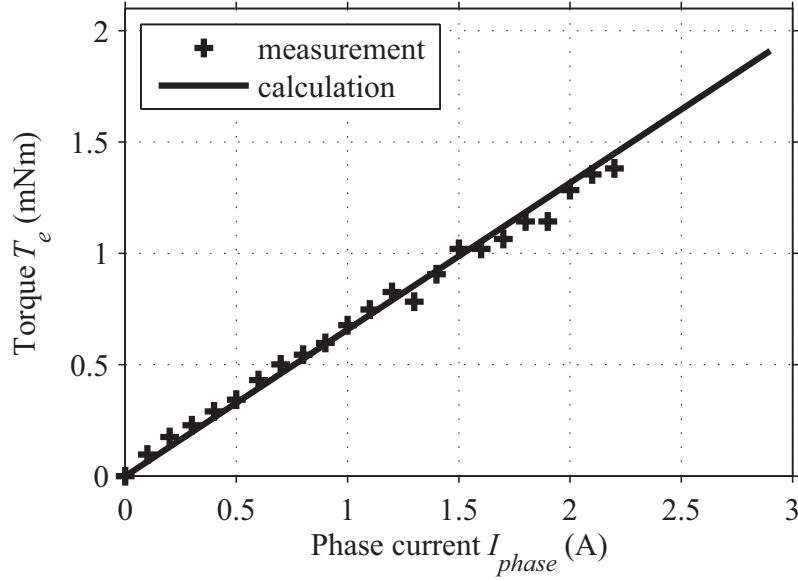


Figure 5.6: Results of the 500 krpm demonstrator: Comparison of predicted and measured torque over phase current.

$$J \frac{\partial \omega}{\partial t} = -T_{d,dec} = -\frac{P_{d,dec}}{\omega} \quad (5.2)$$

where rotor inertia J can be calculated exactly due to the simple rotor geometry. With the deceleration test the total losses in open-loop operation $P_{d,dec}$ are determined, which include copper proximity $P_{Cu,p}$, iron P_{Fe} , air friction $P_{f,air}$ and bearing losses $P_{d,brg}$ according to

$$P_{d,dec} = P_{Cu,p} + P_{Fe} + P_{d,brg} + P_{f,air}. \quad (5.3)$$

$P_{d,dec}$ does not include the dc current losses $P_{Cu,dc}$. The bearing friction losses are included in these measurements, but not included in the total losses P_d that are calculated in the optimization procedure in section 2.4. Estimating the friction losses of ball bearings is difficult because these losses depend on the age of the bearings, the axial preload, the temperature, and the unbalance of the rotor.

In order to verify the analytical model for the air friction losses, the deceleration test on a test bench with two of the 500 krpm machines mounted on one shaft has been undertaken under ambient conditions and in a vacuum chamber. Comparing this two measurements leads to

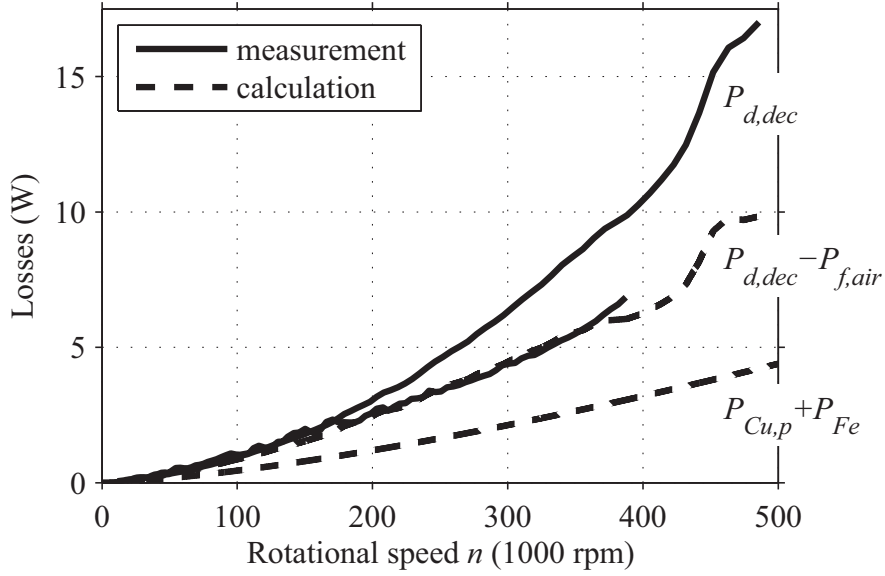


Figure 5.7: Results of a test bench setup with the 500 krpm demonstrator machine with silicon-iron stator core: losses $P_{d,dec}$ and $P_{d,dec} - P_{f,air}$ measured by means of the deceleration test (solid) and the calculated losses $P_{d,dec} - P_{f,air}$ and $P_{Cu,p} + P_{Fe}$ (dashed). The total measured losses can be subdivided into the proximity effect losses plus the iron losses, the bearing friction losses and the air friction losses. The current dependent resistive losses are excluded in both measurements and calculations. The measured total losses minus the calculated air friction losses, match the experiments excluding air friction losses (vacuum deceleration tests) well.

the air friction losses, as in vacuum they should be negligible. Only measurements from 400 000 rpm are presented because above that speed the bearings fail due to the absence of air and therefore appropriate cooling. Nevertheless the measurements show a difference, and the air friction losses can be experimentally determined. The experimental results from a 500 krpm machine with silicon-iron core match the calculations very well as can be seen in Figure 5.7.

Having measured the total losses including bearing losses $P_{d,brg}$ experimentally, and having validated the models for air friction losses $P_{f,air}$, copper losses $P_{Cu,s} + P_{Cu,p}$ and trusting the iron loss calculation the bearing losses $P_{d,brg}$ can be determined according to

$$P_{d,brg} = P_{d,dec} - P_{f,air} - P_{Cu,p} - P_{Fe}. \quad (5.4)$$

For one individual 500 krpm machine, the measured losses $P_{d,dec}$ and calculated losses $P_d - P_{Cu,dc}$ of the 500 krpm machine are shown in Figure 5.8 and the corresponding losses of the 1 million rpm machine are shown in Figure 5.9. The results of the 500 krpm machine deceleration test in Figure 5.7 slightly differ from the the results in Figure 5.8 since for the first a test bench setup has been used, whereas for the latter the machine unit of the miniature turbocompressor is used, the two are slightly different in housing geometry. It is to be noted that the calculated losses do not include the bearing friction losses. The manufacturer's estimate is 5 W for the two bearings at 500 000 rpm, which corresponds well to the results shown in Figure 5.7 to Figure 5.9. It can be seen that the losses can be drastically reduced by optimizing the inner dimensions of the machine, namely decreasing the rotor radius R_2 . This reduction is mainly due to decreased air friction losses, which are proportional to R_2^4 as shown in (2.30). It is also clear from these measurements that going to higher speeds, especially towards 1 million rpm, the effort for a further efficiency optimization should be on the bearing system and not on the machine side anymore. A better performance concerning losses might be achieved with a magnetic or air bearing.

5.3.5 Machine Efficiency

Theoretically, when operating as a generator, the efficiency of the machine incorporating copper, iron and air friction losses can be measured by comparing the mechanical power measured with the reaction torque on the stator according to section 5.3.3 and the angular speed and the electrical output power measured with a three phase power analyzer. However, measuring efficiency differences in the percent range would require a torque measurement in the area of 10 μ Nm, which is very hard to achieve. The torque measurement is disturbed by the friction of the bearings holding the stator, the cable connections from the stator, and any vibration on the test bench itself. Therefore, the determination of the losses via the deceleration test and the resistance measurement is more exact.

It is to be noted that the efficiency of the machine is very much dependent on the allocation of the losses to either the electrical drive system or the application. With defining all the friction losses (air friction and bearing) as part of the application (common in a gas turbine or an air

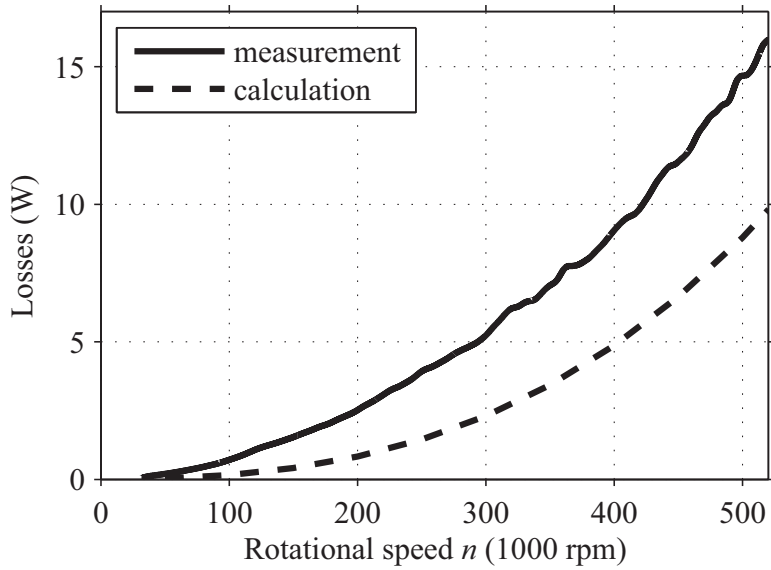


Figure 5.8: Results of the 500 krpm demonstrator with amorphous stator core: losses measured by means of the deceleration test (solid) and calculated losses (dashed). The measured losses include the proximity effect losses, the iron losses, the air friction losses, and the bearing friction losses. The calculated losses include the proximity effect losses, the iron losses, and the air friction losses. The current dependent resistive losses are excluded in both cases.

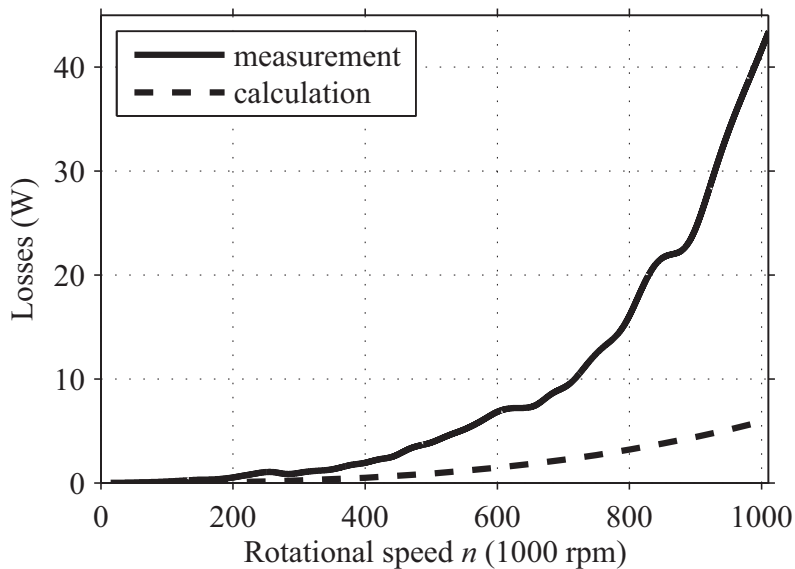


Figure 5.9: Results of the 1 million rpm demonstrator: losses measured by means of the deceleration test (solid) and calculated losses (dashed). Explanations of the loss components are as in Fig. 18.

	500 krpm	1 Mrpm
$P_d = P_{Cu} + P_{Fe} + P_{f,air} + P_{d,brg}$	84.4%	67.9%
$P_d = P_{Cu} + P_{Fe} + P_{f,air}$	88.9%	91.6%
$P_d = P_{Cu} + P_{Fe}$	94.3%	95.7%

Table 5.2: Machine efficiencies of the two machines under investigation, including and excluding bearing and air friction losses.

bearing drilling spindle) the efficiency of the 500 krpm machine is 94.3%. However, allocating the losses to the drive system (for example for a turbocompressor system) the efficiency drops down to 84.4%. Therefore, in Table 5.2 the efficiencies of the machines for rated speed and power are presented including as well as excluding ball bearing and air friction losses. It is the author's opinion that the air friction losses belong to the electrical machine, whereas for the bearing losses it is depending on the application. From Table 5.2 it is also clear that a further optimization concerning efficiency has to be on the bearing side rather than on the machine or power electronics design, especially for highest speeds.

Chapter 6

Conclusion

6.1 Summary

To the author's knowledge, 1 million rpm is the highest speed ever achieved with an electrical drive system. Furthermore, no electrically driven compressor has been reported achieving speeds in the area of 500 000 rpm. These results have been achieved with individual research results summarized in the following.

The machine selection has resulted in a permanent-magnet machine with an air gap winding and a ironless rotor as the ideal choice. This selection has not only considered the machine design and optimization, but was also undertaken with respect to the power and control electronics design. There, for the usual VSI the low inductance due to the slotless winding and ironless rotor is a drawback, whereas for the chosen PAM inverter topology and commutation strategy, and stator flux based sensorless control, the low inductance becomes an advantage.

Increasing the rotational speed of a machine results in additional high-frequency losses in the rotor, the winding, the iron, and especially in air friction. The first three losses are due to increased eddy-current effects and are reduced with an according machine topology with low armature reaction and no slotting effects (rotor losses), a litz wire winding (copper losses) and a high-frequency stator core material (iron losses). The air friction losses however can only be reduced by decreasing the rotor ra-

dus (and length), which influences the other loss components. Therefore, in this Thesis an optimization method was developed in order to minimize the total losses. The constraints are set by the outer dimensions, mechanical stress limitations in the rotor, and the rotordynamic design.

Compared to a traditional design not considering air friction losses and using a standard high-frequency stator core material, with the optimization method presented in this Thesis the losses could be reduced from 14.2 Watts to 5.2 Watts, which is a reduction of 62%. This reduction is mainly due to the consideration of the air friction losses and therefore a smaller rotor radius, and the implementation of amorphous iron for the stator core. Although a further reduction could be achieved with higher energy density permanent-magnets, nanocrystalline iron stator cores, and additional efforts on the winding configuration, the improvements would be marginal. If anything, the effort for an optimization concerning efficiency should be on the bearing system, as this has a much higher influence on the total system efficiency. As an example, the ball bearings used for the experiments have losses of approximately 2.5 Watts at 500 000 rpm, but at 1 000 000 rpm they increase to approximately 18 Watts.

For the power electronics needed to drive the machine at highest speeds, the traditional VSI is not the automatic choice. It was shown that it would result in a very high switching frequency and a high current control bandwidth needed. The PAM topology and commutation strategy is chosen due to an inverter switching frequency that equals the fundamental frequency, only a single, low dynamic current control needed on the dc side, and the possibility for a simple, back EMF based sensorless control. The usual drawbacks of higher harmonic content in the phase currents and lower dynamic current and speed control are no problem; due to the litz wire winding and the low armature reaction in the machine the additional losses due to current harmonics can be neglected, and the control dynamics needed are low in all presented applications at high speed.

A sensorless control method for highest speeds, partly presented in earlier literature, was developed. It is based on the stator flux zero crossings detection. Due to the low inductance of the machine, the angle deviation of the stator flux compared to the permanent-magnet flux is very small and does not have to be corrected.

With these technologies, two prototypes were realized; a 500 000 rpm

turbocompressor system and a 1 million rpm demonstrator drive system. Both of them include the machine design presented in this Thesis, and are driven by a low voltage, MOSFET based PAM inverter including the presented sensorless control. With these two systems, the theoretical considerations were experimentally verified.

Beside these specific results, the author dares to add some general remarks and lessons learned during the Thesis. Firstly, manufacturing a drive system, realizing it in hardware, is a main issue as it influences the design considerations and calculations. Furthermore, the manufacturing usually has the biggest time constant in a project. Secondly, for designing an electrical drive systems for highest speeds, a very interdisciplinary field of technologies has to be taken into account: the bearing system, rotordynamics, mechanical stress analysis, materials, thermal design, electromagnetics, power electronics and control systems. An integrated drive system design is needed considering all these different aspects. And last but not least, designing an ultra-high-speed electrical drive system always has to include the application the machine is connected to. In contrary to low speed applications, this connection can not be made with a coupling and the application can therefore not be designed separately. This includes especially the mechanical rotor design and the rotor dynamic analysis. Due to the resulting close proximity of machine and application, they are also thermally connected. In some applications, also the electronics might be in close proximity or even integrated into the application, for example in a portable gas turbine system.

6.2 Outlook

Besides the results achieved in this Thesis there are some future challenges determined. As mentioned before, the most effective efficiency improvement in the drive system can be achieved with new bearing technologies. This could also solve some of the other drawbacks of the ball bearings used for the experimental setups in this Thesis, most of all the limited lifetime, but also the temperature limits towards lower and higher temperatures. Possible options are air bearings and magnetic bearings, both an area of research itself.

As mentioned before, designing an ultra-high-speed electrical drive system always has to include the application the machine is connected to.

CONCLUSION

Due to the therefore required integrated design including electrical drive system and application, the research can be extended toward different applications. Especially turbomachinery, compressors and turbines, have requirements very well suiting the specifications of the drive system and can therefore be an application area for future research.

Further research vectors could include high-temperature machines and electronics, MEMS-based machines and applications for even smaller power demands, and zero and low-speed sensorless control.

Finally, also the manufacturing, especially of machine parts (e.g. rotor bandages out of different materials such as ceramics or carbon fiber), can be an area of research itself. There still are many problems to be solved and many processes to be optimized.

Bibliography

- [1] A. Binder and T. Schneider, “High-speed inverter-fed AC drives,” in *Proceedings of International Aegean Conference on Electrical Machines and Power Electronics (ACEMP '07)*, 2007, pp. 9–16.
- [2] M. A. Rahman, A. Chiba, and T. Fukao, “Super high speed electrical machines - summary,” in *Proceedings of IEEE Power Engineering Society General Meeting*, vol. 2, 2004, pp. 1272–1275.
- [3] I. Takahashi, T. Koganezawa, G. Su, and K. Ohyama, “A super high speed PM motor drive system by a quasi-current source inverter,” *IEEE Transactions on Industry Applications*, vol. 30, no. 3, pp. 683–690, May–Jun. 1994.
- [4] Wafer grinding products. Westwind Air Bearings. <http://www.westwind-airbearings.com/>.
- [5] PCB drilling products. Westwind Air Bearings. <http://www.westwind-airbearings.com/>.
- [6] J. Thur, “Antriebssystem für höchste Geschwindigkeiten zur feldorientierten Regelung von permanenterregten Hochfrequenzspindeln ohne Drehgeber und ohne Signalrechner,” Ph.D. dissertation, Bergische Universität, Wuppertal, Germany, 2006.
- [7] Automotive fuel cell air compressor/expander system. Mohawk Innovative Technology. <http://www.miti.cc/>.
- [8] J. R. Bumby, E. S. Spooner, J. Carter, H. Tennant, G. G. Mego, G. Dellora, W. Gstrein, H. Sutter, and J. Wagner, “Electrical machines for use in electrically assisted turbochargers,” in *Proceedings*

- of IEE Second International Conference on Power Electronics, Machines and Drives (PEMD '04)*, vol. 1, 2004, pp. 344–349.
- [9] F. Westin, “Simulation of turbocharged SI-engines - with focus on the turbine,” Ph.D. dissertation, Royal Institute of Technology, Stockholm, Sweden, 2005.
- [10] S. Kang, S. J. J. Lee, and F. B. Prinz, “Size does matter: The pros and cons of miniaturization,” *ABB Review*, vol. 2, no. 1, pp. 54–62, Jan.–Feb. 2002.
- [11] A. H. Epstein, “Millimeter-scale, micro-electro-mechanical systems gas turbine engines,” *Journal of Engineering for Gas Turbines and Power*, vol. 126, no. 2, pp. 205–226, Apr. 2004.
- [12] S. A. Jacobson and E. H. Epstein, “An informal survey of power MEMS,” in *Proceedings of International Symposium on Micro-Mechanical Engineering*, 2003, pp. 513–520.
- [13] S. Kang, “Fabrication of functional mesoscopic ceramic parts for micro gas turbine engines,” Ph.D. dissertation, Stanford University, Stanford, USA, 2001.
- [14] P. Tsao, M. Senesky, and S. R. Sanders, “An integrated flywheel energy storage system with homopolar inductor motor/generator and high-frequency drive,” *IEEE Transactions on Industry Applications*, vol. 39, no. 6, pp. 1710–1725, Nov.–Dec. 2003.
- [15] W. Wang, “Design of high speed flywheel motor/generator for aerospace applications,” Ph.D. dissertation, Pennsylvania State University, State College, USA, 2004.
- [16] J. Szydlo, “High speed depth optical scanner,” Ph.D. dissertation, Ecole Polytechnique Federale De Lausanne, Lausanne, Switzerland, 2000.
- [17] Rotating mirror concept. Cordin. <http://www.cordin.com/>.
- [18] T. Mashimo, S. Okazaki, and S. Shibasaki, “Ultracentrifuge apparatus to generate a strong acceleration field of over 1 000 000 g at a high temperature in condensed matter,” *Review of Scientific Instruments*, vol. 67, no. 9, pp. 3170–3174, 1996.

- [19] J. Oyama, T. Higuchi, T. Abe, K. Shigematsu, and R. Moriguchi, “The development of small size ultra-high speed drive system,” in *Proceedings of Power Conversion Conference (PCC '07)*, 2007, pp. 1571–1576.
- [20] High speed PM brushless dc motor/generator. Calnetix. <http://www.calnetix.com/>.
- [21] S. Das, D. P. Arnold, I. Zana, J. W. Park, M. G. Allen, and J. H. L. Lang, “Microfabricated high-speed axial-flux multiwatt permanent-magnet generators—Part I: Modeling,” *IEEE/ASME Journal of Microelectromechanical Systems*, vol. 15, no. 5, pp. 1330–1350, Oct. 2006.
- [22] D. P. Arnold, S. Das, J. W. Park, I. Zana, J. H. Lang, and M. G. Allen, “Microfabricated high-speed axial-flux multiwatt permanent-magnet generators—Part II: Design, fabrication, and testing,” *IEEE/ASME Journal of Microelectromechanical Systems*, vol. 15, no. 5, pp. 1351–1363, Oct. 2006.
- [23] D. E. Hesmondhalgh and D. Tipping, “Design of a high-speed permanent magnet motor,” in *Proceedings of IEE Colloquium on Permanent Magnet Machines*, 1988, pp. 6/1–6/2.
- [24] PCB drilling product information. Fischer-Precise Group. <http://www.precise.de/>.
- [25] L. G. Frechette, S. A. Jacobson, K. S. Breuer, F. F. Ehrich, R. Ghodssi, R. Khanna, C. W. Wong, X. Zhang, M. A. Schmidt, and A. H. Epstein, “High-speed microfabricated silicon turbomachinery and fluid film bearings,” *IEEE/ASME Journal of Microelectromechanical Systems*, vol. 14, no. 1, pp. 141–152, Feb. 2005.
- [26] K. Isomura, S. Togo, K. Hikichi, S. Goto, and S. Tanaka, “Analytical and experimental study of hydroinertia gas bearings for micro-machine gas turbines,” in *Proceedings of ASME Turbo Expo 2005: Power for Land, Sea and Air*, 2005, pp. 747–755.
- [27] M. Salehi, H. Heshmat, J. F. Walton, and M. Tomaszewski, “Operation of a mesoscopic gas turbine simulator at speeds in excess of 700,000 rpm on foil bearings,” in *Proceedings of ASME Turbo Expo 2004: Power for Land, Sea and Air*, 2004, pp. 87–94.

- [28] J. W. Beams, J. L. Young, and J. W. Moore, "The production of high centrifugal fields," *Journal of Applied Physics*, vol. 17, pp. 886–890, Apr. 1946.
- [29] A. R. Boletis, "High speed micromotor on a three axis active magnetic bearing," Ph.D. dissertation, Ecole Polytechnique Federale De Lausanne, Lausanne, Switzerland, 2005.
- [30] P. L. Chapman and P. T. Krein, "Smaller is better? [micromotors and electric drives]," *IEEE Industry Applications Magazine*, vol. 9, no. 1, pp. 62–67, Jan.–Feb. 2003.
- [31] U. Kafader and J. Schulze, "Similarity relations in electromagnetic motors - limitations and consequences for the design of small dc motors," in *Proceedings of 9th International Conference on New Actuators (ACTUATOR '04)*, 2004, pp. 309–312.
- [32] N. Bianchi, S. Bolognani, and F. Luise, "Potentials and limits of high-speed PM motors," *IEEE Transactions on Industry Applications*, vol. 40, no. 6, pp. 1570–1578, Nov.–Dec. 2004.
- [33] Y. Chen, J. Shen, and Z. Fang, "Topology and preliminary design of slotless brushless dc motor," in *Proceedings of IEEE International Electric Machines and Drives Conference*, 1997, pp. WB2/7.1–WB2/7.3.
- [34] P. Ragot, M. Markovic, and Y. Perriard, "Analytical determination of the phase inductances for a brushless dc motor with faulhaber winding," in *Proceedings of 42nd IEEE Industry Applications Society Annual Meeting (IAS '07)*, 2007, pp. 1538–1543.
- [35] S.-M. Jang, S.-S. Jeong, D.-W. Ryu, and S.-K. Choi, "Comparison of three types of PM brushless machines for an electro-mechanical battery," *IEEE Transactions on Magnetics*, vol. 36, no. 5, pp. 3540–3543, 2000.
- [36] C. Zwysig, J. W. Kolar, W. Thaler, and M. Vohrer, "Design of a 100 W, 500000 rpm permanent-magnet generator for mesoscale gas turbines," in *Proceedings of 40th IEEE Industry Applications Society Annual Meeting (IAS '05)*, vol. 1, 2005, pp. 253–260.
- [37] S. Timoshenko and J. Goodier, *Theory of elasticity*. New York, USA: McGraw-Hill, 1970.

- [38] Z. Q. Zhu, D. Howe, E. Bolte, and B. Ackermann, “Instantaneous magnetic field distribution in brushless permanent magnet dc motors. I. Open-circuit field,” *IEEE Transactions on Magnetics*, vol. 29, no. 1, pp. 124–135, Jan 1993.
- [39] U. Kim and D. K. Lieu, “Magnetic field calculation in permanent magnet motors with rotor eccentricity: without slotting effect,” *IEEE Transactions on Magnetics*, vol. 34, no. 4, pp. 2243–2252, July 1998.
- [40] K. F. Rasmussen, J. H. Davies, T. J. E. Miller, M. I. McGelp, and M. Olaru, “Analytical and numerical computation of air-gap magnetic fields in brushless motors with surface permanent magnets,” *IEEE Transactions on Industry Applications*, vol. 36, no. 6, pp. 1547–1554, Nov.–Dec. 2000.
- [41] Z. Q. Zhu, D. Howe, and C. C. Chan, “Improved analytical model for predicting the magnetic field distribution in brushless permanent-magnet machines,” *IEEE Transactions on Magnetics*, vol. 38, no. 1, pp. 229–238, Jan. 2002.
- [42] T. Modeer, “On stator yoke rotational iron losses in permanent magnet machines,” in *Proceedings of International Conference on Electrical Machines (ICEM '06)*, 2006, pp. 5, Paper OTA4–1.
- [43] K. Atallah, Z. Q. Zhu, and D. Howe, “Armature reaction field and winding inductances of slotless permanent-magnet brushless machines,” *IEEE Transactions on Magnetics*, vol. 34, no. 5, pp. 3737–3744, Sept. 1998.
- [44] J. A. Ferreira, *Electromagnetic modeling of power electronic converters*. Norwell, USA: Kluwer Academic Publishers, 1989.
- [45] X. Nan and C. R. Sullivan, “An equivalent complex permeability model for litz-wire windings,” in *Proceedings of 40th IEEE Industry Applications Society Annual Meeting (IAS '05)*, vol. 3, 2005, pp. 2229–2235.
- [46] J. D. Ede, Z. Q. Zhu, and D. Howe, “Optimal split ratio for high-speed permanent magnet brushless dc motors,” in *Proceedings of 5th International Conference on Electrical Machines and Systems (ICEMS '01)*, vol. 2, 2001, pp. 909–912.

- [47] C. Zwyssig, S. D. Round, and J. W. Kolar, “Analytical and experimental investigation of a low torque, ultra-high speed drive system,” in *Proceedings of 41st IEEE Industry Applications Society Annual Meeting (IAS '06)*, vol. 3, 2006, pp. 1507–1513.
- [48] C. Mi, G. R. Slemon, and R. Bonert, “Modeling of iron losses of permanent-magnet synchronous motors,” *IEEE Transactions on Industry Applications*, vol. 39, no. 3, pp. 734–742, May–June 2003.
- [49] C. P. Steinmetz, “On the law of hysteresis,” *Proceedings of the IEEE*, vol. 72, no. 2, pp. 197–221, Feb. 1984.
- [50] M. Mack, “Luftreibungsverluste bei elektrischen Maschinen kleiner Baugröße,” Ph.D. dissertation, Universität Stuttgart, Stuttgart, Germany, 1967.
- [51] Litz wire table. Pack Feindrähte. <http://www.pack-feindraehte.de/>.
- [52] C. Fritsche, “Digital geregelter Frequenzumrichter mit Ausgangsfilter für schnelle Synchronmaschinen,” Ph.D. dissertation, ETH Zürich, Zürich, Switzerland, 2000.
- [53] K. Taniguchi and A. Okumura, “A PAM inverter system for vector control of induction motor,” in *Proceedings of Power Conversion Conference (PCC '93)*, 1993, pp. 478–483.
- [54] K.-H. Kim and M.-J. Youn, “Performance comparison of PWM inverter and variable dc link inverter schemes for high-speed sensorless control of BLDC motor,” *Electronics Letters*, vol. 38, no. 21, pp. 1294–1295, 2002.
- [55] J. Zhang and M. Schroff, “High-performance micromotor control systems,” in *Proceedings of 29th IEEE Industrial Electronics Society Annual Conference (IECON '03)*, vol. 1, 2003, pp. 347–352.
- [56] T. C. Green, M. H. Taha, N. A. Rahim, and B. W. Williams, “Three-phase step-down reversible ac-dc power converter,” *IEEE Transactions on Power Electronics*, vol. 12, no. 2, pp. 319–324, March 1997.
- [57] F. Z. Peng, “Z-source inverter,” *IEEE Transactions on Industry Applications*, vol. 39, no. 2, pp. 504–510, March–April 2003.

- [58] C. Zwyssig, S. D. Round, and J. W. Kolar, “Power electronics interface for a 100 W, 500000 rpm gas turbine portable power unit,” in *Proceedings of 21st Annual IEEE Applied Power Electronics Conference and Exposition (APEC '06)*, 2006, pp. 283–289.
- [59] Z. Q. Zhu, J. D. Ede, and D. Howe, “Design criteria for brushless dc motors for high-speed sensorless operation,” *International Journal of Applied Electromagnetics and Mechanics*, vol. 15, pp. 79–87, 2001/2002.
- [60] K. Iizuka, H. Uzuhashi, M. Kano, T. Endo, and K. Mohri, “Micro-computer control for sensorless brushless motor,” *IEEE Transactions on Industry Applications*, no. 3, pp. 595–601, May 1985.
- [61] C. J. Teo and Z. S. Spakovszky, “Modeling and experimental investigation of micro-hydrostatic gas thrust bearings for micro-turbomachines,” in *Proceedings of ASME Turbo Expo 2005: Power for Land, Sea and Air*, 2005, pp. 689–700.
- [62] J. Schiffmann and D. Favrat, “Multi-objective optimisation of herringbone grooved gas bearings supporting a high speed rotor, taking into account rarefied gas and real gas effects,” in *Proceedings of 8th Biennial ASME Conference on Engineering Systems Design and Analysis*, 2006, pp. 857–865.
- [63] J. Peirs, P. Vleugels, T. Waumans, M. Verlinden, D. Reynaerts, and F. Verplaetsen, “Development of high-speed bearings for micro gas turbines,” in *Proceedings of MicroMechanics Europe Workshop*, 2004, pp. 313–316.
- [64] P. Imoberdorf, C. Zwyssig, S. D. Round, and J. W. Kolar, “Combined radial-axial magnetic bearing for a 1 kW, 500,000 rpm permanent magnet machine,” in *Proceedings of 22nd Annual IEEE Applied Power Electronics Conference (APEC '07)*, 2007, pp. 1434–1440.
- [65] M. H. Kimman, H. H. Langen, J. van Eijk, and R. M. Schmidt, “Design and realization of a miniature spindle test setup with active magnetic bearings,” in *Proceedings of IEEE/ASME International Conference on Advanced Intelligent Mechatronics*, 2007, pp. 1–6.
- [66] R. Larsonneur, “Design and control of active magnetic bearing systems for high speed rotation,” Ph.D. dissertation, ETH Zürich, Zürich, Switzerland, 1990.

- [67] T. Lembke, “Design and analysis of a novel low loss homopolar electrodynamic bearing,” Ph.D. dissertation, Royal Institute of Technology, Stockholm, Sweden, 2005.
- [68] H. Heshmat, H. Ming Chen, and J. F. Walton, “On the performance of hybrid foil-magnetic bearings,” *Journal of Engineering for Gas Turbines and Power*, vol. 122, pp. 73–81, 2000.
- [69] R. Gasch, R. Nordmann, and H. Pfützner, *Rotordynamik*. Berlin, Germany: Springer, 2001.
- [70] B. Schneider, M. Bruderer, D. Dyntar, C. Zwysig, M. Diener, K. Boulouchos, R. S. Abhari, L. Guzzella, and J. W. Kolar, “Ultra-high-energy-density converter for portable power,” in *Proceedings of International Workshop on Micro and Nanotechnology for Power Generation and Energy Conversion Applications*, 2005, pp. 81–84.
- [71] The solar impulse challenge. <http://www.solarimpulse.com/>.
- [72] O. Aglen, “Back-to-back tests of a high-speed generator,” in *Proceedings of IEEE Electric Machines and Drives Conference (IEMDC '03)*, vol. 2, 1–4 June 2003, pp. 1084–1090.
- [73] H. Ota, T. Ohara, Y. Karata, S. Nakasima, and M. Takeda, “Novel micro torque measurement method for microdevices,” in *Journal of Micromechanics and Microengineering*, vol. 11, no. 5, Sept. 2001, pp. 595–602.
- [74] V. Gass, B. H. van der Schoot, S. Jeanneret, and N. F. de Rooij, “Micro-torque sensor based on differential force measurement,” in *Proceedings of IEEE Workshop on Micro Electro Mechanical Systems (MEMS '94)*, 25–28 Jan. 1994, pp. 241–244.

Vita

Name	Christof Zwyssig
Birth	24 th July 1978
Place of birth	Richterswil, ZH (Switzerland)
Citizen of	Switzerland
Education	1985—1991 Primary, Ernetschwil-Gebertingen 1991—1993 Secondary, Gommiswald 1993—1998 Gymnasium, Kantonsschule Wattwil Matura Typus C
University	1998—2004 ETH Zürich M.Sc. in Electrical Engineering 2004 Chalmers University of Technology, Göteborg Master Thesis in Wind Power
Doctorate	2004—2008 Doctorate at the Power Electronics Systems Laboratory (PES), ETH Zürich